Electronic correlations in strongly spin-orbit coupled systems

A Thesis

Submitted to the
Tata Institute of Fundamental Research, Mumbai
for the degree of
Doctor of Philosophy
in
Physics

By

Sarbajaya Kundu
Department of Theoretical Physics
Tata Institute of Fundamental Research
Mumbai

July 2019
Final version submitted in September 2019

To Ma and Baba...

DECLARATION

This thesis is a presentation of my original research work. Wherever contributions of others are involved, every effort is made to indicate this clearly, with due reference to the literature, and acknowledgement of collaborative research and discussions.

The work was done under the guidance of Professor Vikram Tripathi, at the Tata Institute of Fundamental Research, Mumbai.

Sarbajaya Kundu

Sarbajaya Kundu

In my capacity as supervisor of the candidate's thesis, I certify that the above statements are true to the best of my knowledge.

Vikram Tripathi

Vikram Tripathi

Date: 25.9.2019

ACKNOWLEDGEMENTS

I have had a wonderful time doing my PhD in TIFR, and the last few years have been among the best and most productive in my life. For this, I must thank my advisor, Prof. Vikram Tripathi, whose able guidance and support has made my PhD work a lot less stressful and a lot more fun. He is an immensely knowledgeable physicist and an incredibly patient teacher, and I have learnt a lot by interacting regularly with him. I would also like to thank all the members of the Theoretical Condensed Matter group for creating such a lively and interactive working atmosphere, and especially Prof. Kedar Damle and Prof. Rajdeep Sensarma for their highly instructive and enjoyable courses, scientific discussions, their careful assessment of my abilities and valuable advice for improvement.

A big 'Thank You' to all my friends in TIFR for the delightful times that we spent together and the memories that we created. I would especially like to mention here Sounak, Ahana, Anirban, Meenakshi, Dattaraj, Vishal, Abhishek and Lavneet, each of whom has contributed to my PhD life in their own unique way. I have also had a great time interacting with some of my seniors such as Debjyoti, Disha, Ronak, Sarath, Tousik, Yogesh and Ritam.

I would not be where I am today without the constant love and support of my parents. They have been there with me at every step and have always encouraged me to put in my best efforts towards every endeavor. Thank you for always being there for me!

ABSTRACT

In recent times, the effects of spin-orbit coupling (SOC) in strongly correlated electron systems has been one of the most actively studied subjects in Condensed Matter Physics, as correlations and SOC together play a crucial role in understanding many new and exotic quantum states of matter. For strongly spin-orbit coupled materials, the weak-to-intermediate correlation regime corresponds to situations where band theory is applicable, and the lifting of degeneracies leads to a nontrivial band topology, such as in topological insulators and semimetals. On the other hand, in the limit of strong electronic correlations, a Mott-like gap opens in the narrow total angular momentum bands, giving rise to the so-called 'spin-orbit assisted Mott insulators'. Such systems often feature multiple Fermi pockets at non-high symmetry points, which opens up the possibility of realizing, for instance, long-range ordered phases with valley-symmetry breaking. In this thesis, we attempt to understand the behavior of some representative systems, which correspond to the regime of strong spin-orbit coupling, accompanied by both weak and strong electronic correlations. The thesis consists of three parts. In the first part, we study electronic phase competition on the (001) surface of the topological crystalline insulator $Pb_{1-x}Sn_xTe$, in the presence of Fermi surface nesting and two-dimensional Van Hove singularities, and identify chiral $p-$wave superconductivity to be the dominant electronic order. We further study the effect of an external magnetization on the chiral $p-$wave order and find that multiorbital effects play an important role in stabilizing electronic order on the surface. Finally, as a possible way of detecting the chiral $p-$wave order, we study impurity-induced subgap bound states in this system and find that only in certain parameter regimes of doping, the impurity bound states provide an unambiguous signature of this order, and otherwise they are indistinguishable from impurity states in, say, a semiconductor. In the second part of the thesis, we combine large-scale exact diagonalization simulations of the torque response for various effective spin models studied in the literature, with high-field torque magnetometry measurements, for probing the underlying interactions in the Mott-insulating honeycomb iridate Na_2IrO_3, which is a popular Kitaev material. Our results indicate the presence of strong ferromagnetic Kitaev correlations in this material, and the possibility of realizing field-induced spin liquid physics beyond the position of a

characteristic peak-dip feature in the torque response, close to the magnetic ordering scale. In the third part of the thesis, we study competing phases in a system of three coupled spinless Luttinger liquids using a renormalization group (RG) treatment of the bosonized interactions. Such an analysis is applicable for strongly spin-orbit coupled systems with multiple small Fermi pockets, such as bismuth, in the presence of a large applied magnetic field, where the behavior is essentially one-dimensional. We find that even at the one-loop level in perturbative RG, off-diagonal contributions are generated in the phase stiffness matrix, which require large nontrivial rotations of the matrix, along with a rescaling of the fields. As a consequence of the rotations involved in the RG procedure, the nature of the electronic phases and critical behavior of this system are in general sensitive to the relative strengths of the interactions as well as the Luttinger liquid parameters. Our results also indicate that it may be possible to realize chiral phases as well as valley symmetry breaking in certain parameter regimes in such systems.

Publication list

Publications relevant to the thesis

1. Sarbajaya Kundu and Vikram Tripathi. “Role of Hund’s splitting in electronic phase competition in $Pb_{1-x}Sn_xTe$", Physical Review B 96 (2017): 205111

2. Sitikantha D. Das, Sarbajaya Kundu, Zengwei Zhu, Eundeok Mun, Ross D. McDonald, Gang Li, Luis Balicas, Alix McCollam, Gang Cao, Jeffrey G. Rau, Hae-Young Kee, Vikram Tripathi and Suchitra E. Sebastian. “Magnetic anisotropy of the alkali iridate Na_2IrO_3 at high magnetic fields: evidence for strong ferromagnetic Kitaev correlations", Physical Review B 99 (2019): 081101(R)

3. Sarbajaya Kundu and Vikram Tripathi, “Competing effects of Hund’s splitting and symmetry-breaking perturbations on electronic order in $Pb_{1-x}Sn_xTe$", European Physical Journal B (2018) 91: 198

4. Sarbajaya Kundu and Vikram Tripathi, “Chiral $p-$wave superconductivity in $Pb_{1-x}Sn_xTe$: signatures from bound-state spectra and wavefunctions”, Physical Review B 99 (2019): 205105

5. Sarbajaya Kundu and Vikram Tripathi, “Competing phases and critical phenomena in three coupled spinless Luttinger liquids”, arXiv:1906.11053

Table of contents

Chapter 1

Introduction

Understanding, controlling and predicting the emergent behavior of strongly correlated electron systems is one of the most pressing challenges in Condensed Matter Physics today [1, 2]. In such systems, large ensembles of individual constituents give rise to highly complex and fascinating collective phenomena. Owing to the strong correlations between the particles, such collective states cannot be understood in terms of the single-particle approximation, and require the development of more sophisticated approaches. Examples of remarkable phenomena arising from electron-electron interactions include local moment formation and magnetism [3, 4], spin liquid states [5, 6], correlated metals [7, 8], quantum criticality [9, 10], and unconventional superconductivity [11, 12]. Over time, these are expected to give way to possible practical applications, such as in superconducting magnets [13, 14] or quantum computers [15–17].

Another important area of research in the field of quantum materials involves nontrivial physics arising from strong spin-orbit coupling (SOC) [18, 19]. Recently, the consequences of spin-orbit coupling (SOC) for correlated electron systems [20, 21, 18, 22] has been a subject of great interest, as the cooperative effects of electronic correlations and strong spin-orbit coupling have been found to play an important role in understanding many new and exotic quantum states of matter. A schematic phase diagram in Fig.1.1, broadly depicting various possible electronic phases that may be realized in the presence of weak and strong electronic interactions as well as spin-orbit coupling, provides an illustration of this physics. In this diagram, the two axes denote an increasing strength of the Hubbard interaction U and spin-orbit coupling λ relative to the hopping amplitude t respectively, and the different regimes corresponding to weak and strong interactions and SOC are separated into four quadrants. For weakly spin-orbit coupled systems, increasing the strength of electronic correlations leads to the formation of Mott insulators [23]. On the other hand, strong spin–orbit coupling can have marked qualitative effects on the band structure of weakly interacting solids. As the

strength of spin-orbit coupling increases, the total angular momentum basis becomes more suitable for describing the behavior of these systems. The degeneracies due to spin-flip or inversion symmetries are lifted, giving rise to non-trivial band topology in weakly interacting electron systems, manifested in topological insulators (TIs) [24–26] and semimetals [27, 28]. As the electronic correlations become stronger, it is possible to open a Mott-like gap in the new bands in the total angular momentum basis which are narrower, giving rise to spin-orbit entangled local moments in a class of materials known as 'spin-orbit assisted Mott insulators' [18]. From the materials perspective, topological insulators have mostly been identified, by the presence of topologically protected Dirac-like surface states [29–32], in classes of solids with heavy s- and p- elements. 3d transition metal oxides have traditionally been a playground for strong correlation effects, and much theoretical and experimental effort has been brought to bear on material systems such as the cuprates [33], manganites [34], and vanadium oxides [35]. In these compounds the SOC is a smaller energy scale as compared to the atomic interactions, crystal field splitting, and kinetic terms. New materials with significant electronic correlations and strong spin-orbit coupling often comprise 4d and 5d transition metal elements [36], where the d-orbitals become more extended, the electron correlation effects decline, while the SOC increases, and all these energy scales become comparable, revealing a plethora of phases. Further, the presence of strong spin-orbit coupling can also lead to the formation of small Fermi pockets at non-high symmetry points in the Brillouin zone, which are replicated by the underlying symmetries of the crystal. Such systems with multiple Fermi pockets can become effectively one-dimensional in the presence of a large applied magnetic field. The method of bosonization [37] has proven useful for studying of effects of electronic correlations in one-dimensional systems. A particularly interesting situation arises in elemental bismuth, with three Dirac-like electron pockets, where a variety of fascinating and anomalous effects [38–45] have been observed at high fields, in the ultraquantum limit, inviting the question of how the effects of electronic correlations are manifested in these strongly spin-orbit coupled systems.

Admittedly, the scope of topics under this overarching umbrella is large, and the choice of problems in this thesis only covers a relatively small part of the area, and specifically focuses on the regime of strong spin-orbit coupling, in the presence of both weak and strong electronic correlations. Below we describe the research projects which form a part of this thesis.

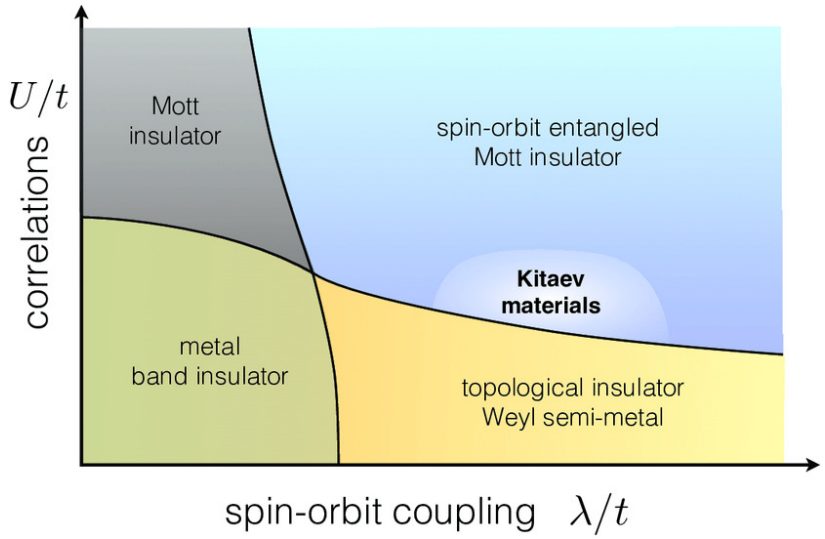

Fig. 1.1 The figure shows different electronic phases that may be realized as a function of the relative strength of the spin-orbit coupling λ/t (along the x-axis) and the Hubbard interaction U/t (along the y-axis), where t denotes the hopping amplitude. The regions of weak and strong interactions, and corresponding regions for the spin-orbit coupling, are separated into four quadrants. In this thesis, we shall discuss situations corresponding to the large spin-orbit coupling regime, for both weak and strong electronic correlations. (Figure has been reproduced from Ref. [46])

1.1 Chiral $p-$wave superconductivity on a topological crystalline insulator surface

Phys. Rev. B 96, 205111 (2017), Eur. Phys. J. B (2018) 91: 198, Phys. Rev. B 99, 205105 (2019)

The topological crystalline insulator (TCI) phase [47] is a new state of matter where the topological character of the electronic bands is protected by crystalline symmetries. The IV-VI semiconductors SnTe and related semiconducting alloys $Pb_{1-x}Sn_x$(Te,Se) were recently predicted to belong to the TCI class [48–51]. These materials feature an even number of Dirac cones on high-symmetry crystal surfaces such as $\{001\}$, $\{110\}$ and $\{111\}$, topologically protected by the reflection symmetry with respect to the $\{110\}$ mirror planes. The band gap minima of IV-VI semiconductors are located at the four L points in the FCC Brillouin zone. For the case of the (001) surface, the L_1 and L_2 points are projected to the $\overline{X}_1$ point on the surface, and the L_3 and L_4 points are projected to the symmetry-related $\overline{X}_2$ point [52]. The resulting surface bandstructure comprises of two disconnected Dirac pockets touching each other at two saddle points, with Type-II Van-Hove singularities [53] in the density of states,

near each of the $\overline{X}$ points [52]. This enhances the possibility of competing electronic orders due to weak repulsive interparticle interactions [54, 55].

We consider interactions between surface electrons corresponding to different valleys and spins, and project these interactions to the positive-energy band lying closest to the Van Hove singularities. The resulting multiplicative form factors $u_{\sigma ai}$ (for a transformation from valley a, spin σ to the ith band) lend a momentum dependence to the effective pairing interactions obtained upon projection. The spin $\uparrow$ and spin $\downarrow$ components have a relative phase of $\exp[i\theta_k]$, due to the Berry phases [56] associated with the surface states, which gives rise to additional phases in the effective interactions in the band picture and distinguishes couplings corresponding to different spin configurations. We have constructed a two-patch renormalization group (RG) [57, 58] for the interaction vertices to study possible electronic instabilities in this system, where the instability is indicated in the form of a pole in the vertex function. The results of the RG analysis are found to be extremely sensitive to the spin configuration being considered. We have investigated the instabilities of the system by evaluating the susceptibilities χ for various types of order, introducing infinitesimal test vertices corresponding to different kinds of pairing into the action. A comparison between the values of exponents corresponding to susceptibilities for different types of order shows that the most divergent susceptibility corresponds to p-wave superconductivity, which is chiral in nature since its symmetry is dictated by the aforementioned $\exp[i\theta_k]$ dependence of the Berry phase factors in the wave functions. We have further examined the robustness of the superconducting order in the presence of an external magnetization, introduced as a Zeeman spin-splitting term in the non-interacting part of the Hamiltonian. We find that in the presence of a finite value of the Hund's splitting Δ, quantified by the difference in the interactions for spin-parallel and spin-antiparallel configurations, chiral p-wave superconductivity [59, 60] continues to be the dominant instability at the one-loop level up to a finite value of the Zeeman splitting M_c (which depends on the value of $\triangle$ chosen). Finally, we have proposed that impurity-induced Shiba-like subgap bound states [61, 62], in certain parameter regimes of doping, can serve as robust and reliable experimental signatures for the chiral $p-$wave order, in contrast to Majorana zero modes [16, 63, 64], which are harder to detect experimentally. In particular, we have distinguished such states from impurity states in semiconductors [65, 66] which are expected to be present even in the absence of the chiral $p-$wave order. We obtain analytical expressions for the bound state spectra and wavefunctions and indicate the properties of such states that can be used to identify the nature of the surface superconducting order.

1.2 High-field torque magnetometry studies in the alkali Iridate Na_2IrO_3

Phys Rev B 99, 081101(R) (2019)

The alkali Iridates A_2IrO_3(A=Na,Li) [67–71] and their celebrated 4d analogue $\alpha-RuCl_3$ [72–76] are popular candidate materials for realizing the physics of the honeycomb Kitaev model [77]. Interactions between the effective $\widetilde{j} = \frac{1}{2}$ pseudospins on every site of the two-dimensional hexagonal lattice in these strongly spin-orbit coupled materials can be described by a dominant anisotropic Kitaev and other subdominant interactions such as Heisenberg and symmetric off-diagonal exchange [78, 79]. Such materials are known to exhibit a magnetically ordered zigzag ground state [71]. Notwithstanding the great progress made, the sign of the dominant Kitaev interaction remains a question of vital importance in ascertaining the underlying physics in this class of materials [67, 70, 76, 78, 80]. There has also been considerable effort towards tuning such materials to a quantum spin liquid state, and, in particular, realizing a field-tuned spin liquid state, especially in $\alpha-RuCl_3$ [74, 73]. In this part of the thesis, we probe the physics of Na_2IrO_3 by using a combination of torque magnetometry studies for magnetic fields up to 60 T, and exact diagonalization calculations. We find a distinctive peak-dip structure in the experimental torque response at high magnetic fields, which we use to constrain the model description of Na_2IrO_3.

The parameter space of couplings for Na_2IrO_3 has thus far been constrained by using both analytical and numerical techniques [67, 70, 81–85, 79, 78], as well as experimental investigation [86]. Based on such phenomenological justification, the simplest model arrived at is a nearest-neighbor model with a dominant antiferromagnetic Kitaev and a smaller ferromagnetic Heisenberg exchange [67]. A different model with a dominant ferromagnetic Kitaev and smaller antiferromagnetic Heisenberg exchange is however suggested by quantum chemistry and other ab initio calculations [87, 70, 82]. In order to stabilize a zigzag phase within such a model, further neighbor couplings [87] or additional anisotropic interactions [78, 79] must be included. Here we distinguish between these categories of models with either a dominant antiferromagnetic Kitaev, or a dominant ferromagnetic Kitaev interaction, by comparing experimental results for the finite magnetic-field response of Na_2IrO_3 with exact diagonalization simulations. For a single crystal of Na_2IrO_3 of dimension $\approx 100\ \mu m$, the torque response (τ) was measured as a function of the magnetic field at various fixed angles θ of the crystalline axis normal to the honeycomb lattice, with respect to the magnetic-field axis. A distinctive nonmonotonous peak-dip feature was observed in the magnetic torque response in the field range of 20-40 T. Our starting point for the theoretical modeling of these features is the usual spin Hamiltonian with nearest-neighbor Kitaev and Heisenberg interactions.

For our calculations, we use a hexagonal 24-site cluster with periodic boundary conditions. The effect of the applied magnetic field is described using a Zeeman term with a constant g-factor, for simplicity. We find that the peak-dip feature in the magnetic torque response is reproduced only by models with a dominant ferromagnetic Kitaev interaction, whereas models with a dominant antiferromagnetic Kitaev interaction display instead a monotonic increase in the magnetic torque with magnetic field, with a single peak close to the Kitaev energy scale. We have computed the spin-spin correlations, as a function of the distance on the hexagonal cluster, for different values of the applied field. We find that the amplitude of oscillation of the correlation functions falls off rapidly with increasing field values, in particular above the zigzag ordering scale, indicating the possibility of realizing field-tuned spin-liquid physics in the regime of field values beyond the position of the peak-dip feature. Such a feature has also been observed recently in another popular Kitaev material $\alpha-RuCl_3$ [88], and our work sheds light on the universality of magnetic field-induced quantum spin liquid physics in these Kitaev systems.

1.3 Phase transitions and critical phenomena in a system of three coupled spinless Luttinger liquids

arXiv:1906.11053

The problem of coupled one-dimensional systems of interacting fermions has received considerable attention in the literature, appearing in diverse contexts. These have been used as building blocks for studying higher-dimensional systems such as cuprate high-temperature superconductors [89], due to the availability of controlled nonperturbative methods and numerical techniques for analyzing them. Such a situation may also arise in many naturally occuring compounds, such as carbon nanotubes [90], low-dimensional organic conductors [91], spin ladders [92, 93], quasi-1D superconductors (such as $K_2Cr_3As_3$ [94]), Mott insulating magnets, as well as artificially manufactured structures (such as self-assembled transition metal nanowires [95]). Bosonization has been the natural tool for studying the low-energy properties of such systems. The majority of these studies involve two-leg ladder systems [89, 95, 91], and the number of comparable studies on systems of three coupled Luttinger liquids have been limited [92, 93, 90]. The common prescription for studying all of these systems involves setting up scaling equations for the stiffness matrix $\widehat{K}$ in the quadratic part of the bosonized Hamiltonian (a sine-Gordon model), and the coupling constants in the sine-Gordon terms. One peculiarity of coupled Luttinger liquid systems that distinguishes them from single-phase Luttinger liquids is the fact that the renormalization

process, even if performed to one-loop order, introduces corrections to all the matrix elements of $\widehat{K}$ in general. These corrections not only change the scaling dimensions of the interactions, but also introduce large rotations of the $\widehat{K}-$matrices, which have, for the most part, been neglected in existing studies of such systems. In our work, we study a system of three coupled spinless Luttinger liquids, set up scaling equations for the $\widehat{K}-$matrix as well as the coupling constants, and solve them numerically. From these solutions, we identify the most singular susceptibilities, corresponding to different order parameters, which in turn determine the phase diagram. Also, from a numerical study of the RG equations, we obtain the critical behavior near the phase transition points. Such an analysis is applicable to multipocket systems with strong spin-orbit coupling, such as bismuth, subject to quantizing magnetic fields.

In our analysis, we have considered density-density type of interactions and situations that physically correspond to partially filled bands. We have bosonized the fermionic model using the standard abelian bosonization prescription. The renormalization group employed by us follows the standard Wilsonian procedure of elimination of fast degrees of freedom, restoration of the cutoff, rescaling of the couplings and the renormalization of the fields. This leads to the generation of off-diagonal components to the $\widehat{K}-$matrices. To keep the Gaussian fixed point unchanged, we rotate the $\widehat{K}-$matrices to diagonalize them and then rescale the fields such that they become proportional to identity matrices, and repeat these steps throughout the RG process. The rotations involved in restoring the above matrices are finite rotations and we always work in the rotating frame, where these large rotations are absent. The coefficients of the cosine terms in the interaction Hamiltonian rotate and stretch during the RG flow procedure, and we write down scaling equations for these coefficients, as well as for the coupling strengths, considering weak repulsive interactions in every channel. The order parameters considered in our analysis are fermionic bilinear operators characterized by chirality and band indices, which may be defined in the particle-particle or particle-hole channels. We analyze the renormalization group flows of the sixteen order parameters generated in the spinless case for opposite chiralities, written in terms of the bosonic fields, to determine the dominant orders in a given parameter regime. To determine the nature of the phase transitions in this system, the scaling of the correlation length ξ at the critical point is determined by identifying the characteristic RG scale y where the couplings $g_\alpha(y)$ cross a designated value $\gtrsim 1$. We obtain continuous phase transitions as a function of the Luttinger liquid parameter $K_\perp^\phi$, which belong to the Berezinskii-Kosterlitz-Thouless (BKT) [96] universality class. We conclude from our analysis of competing phases in this system that it is possible to isolate specific interband or intraband particle-particle and particle-hole orders for extreme values of the parameter $K_\perp^\phi$, whereas for $K_\perp^\phi \sim 1$, various orders compete

with one another, and in this regime, the initial conditions on the interactions play a crucial role in the deciding the dominant electronic order.

The rest of the thesis is divided into three parts. The first part discusses aspects of electronic phase competition in a topological crystalline insulator. This part consists of three chapters. Chapter-2 provides an introduction to topological phases of matter. Chapter-3 is dedicated to studying competing electronic instabilities on a topological crystalline insulator surface, and the effect of an external magnetization on the resulting chiral $p-$wave superconducting state. Chapter-4 discusses the possibility of using impurity-induced Shiba-like subgap bound states in certain parameter regimes of doping as an experimental signature of the chiral $p-$wave order on the TCI surface. The second part of the thesis discusses high-field torque magnetometry measurements in the alkali Iridate Na_2IrO_3 and numerical evidence for strong ferromagnetic Kitaev correlations as well as a possible field-induced spin liquid state in this material. It comprises of two chapters. Chapter-5 provides an introduction to Kitaev materials. Chapter-6 discusses the high-field magnetization response of various effective spin models proposed to describe the Kitaev candidate Na_2IrO_3, using exact diagonalization simulations on a hexagonal 24-site cluster with periodic boundary conditions. The third part of the thesis discusses phase transitions and critical phenomena in a system of three coupled spinless Luttinger liquids. Chapter-7 discusses the physical contexts in which interacting one-dimensional systems appear, and our work on studying interaction effects for three coupled spinless Luttinger liquids, using a renormalization group analysis of the bosonized interactions, that takes into account the effect of off-diagonal corrections generated in the phase stiffness matrices, at the one-loop level. Finally, Chapter-8 provides a summary of the topics covered in this thesis.

ELECTRONIC PHASE COMPETITION ON A TOPOLOGICAL CRYSTALLINE INSULATOR SURFACE

Chapter 2

Topological phases of matter

In the past decade, there has been remarkable progress in our understanding of topological states of matter [97, 98]. These are gapped quantum phases in which the characterization of order goes beyond the conventional paradigm of Landau's symmetry breaking theory. There are three types of topological phases: topologically ordered phases, symmetry protected topological (SPT) phases, and symmetry enriched topological (SET) phases [99, 100], each of which is associated with an unconventional order. For a topologically ordered phase, the ground state can never be deformed into a trivial ordered state by local unitary operations. These are gapped long-range entangled phases and may harbor excitations bearing fractional statistics. In the presence of a global symmetry, the ground state is short-range entangled and equivalent to a trivial ordered state up to unitary transformations which are, however, constrained by the symmetry. Such phases are thus protected by a global symmetry, and are known as symmetry-protected topological (SPT) phases [101–103, 97]. The global symmetry can also intertwine with the non-trivial topological order, leading to symmetry-enriched topological (SET) phases [100, 104]. Materials which realize such topological states in their bulk are known as topological materials.

Below, we shall discuss topological insulators (TIs) and topological crystalline insulators (TCIs), which are specific examples of SPT phases.

2.1 Topological insulators

Topological insulators [105–107, 25] are gapped quantum states of matter, with bulk wavefunctions that possess non-standard topological properties, quantified by various topological invariants, i.e. discrete quantities that remain unchanged upon adiabatic deformations of the system. These feature gapless edge or surface states, a universal and remarkable consequence of a nontrivial bulk topology.

Topological phenomena were first observed in the context of the Integer Quantum Hall Effect (IQHE) [108, 109], where a two-dimensional electron gas at very low temperatures is subjected to a strong perpendicular magnetic field. Here, quantized plateaus appear in the Hall conductivity, that can be attributed to the topological character of the bulk Landau levels, expressed in terms of an integer topological invariant, known as the TKNN invariant [110]. The Quantum Spin Hall (QSH) insulator state was later proposed by Kane and Mele [24], for a model of graphene with strong spin-orbit coupling, which established that the constraints imposed by time-reversal symmetry could lead to a new kind of topological order, characterized by a Z_2 index. Such a phase has been experimentally realized in CdTe/HgTe/CdTe quantum wells [111, 112], and is associated with counter-propagating edge states. This topological classification was soon extended to three dimensions, where the topology is fully characterized by four Z_2 invariants [113]. These have the advantage of being fairly prevalent, and realizable under ambient conditions. Several classes of materials with strong spin-orbit coupling, such as $Bi_{1-x}Sb_x$ alloys [114–117], Bi_2Se_3, Bi_2Te_3 [29, 118–121] and strained HgTe [122] have been established to be three-dimensional topological insulators, with surface states that have a linear dispersion and obey the Dirac equation. These Dirac-like surface states are characterized by spin-momentum locking, and probed experimentally using techniques such as Angle-Resolved Photoemission (ARPES) [29, 123] and Scanning Tunneling Microscopy (STM) [118, 111, 124, 125]. The notion of three-dimensional topological insulators has now been extended to systems that host no gapless surface states but exhibit topologically protected gapless corner states (localized at the corners) [126] or hinge states (that propagate along the edges) [127]. Their topological character is protected by spatiotemporal symmetries. These systems can be subsumed under the notion of higher-order TIs.

We shall now discuss new topological phases that are subsets of SPT phases, relevant to this thesis. These are a) topological crystalline insulators (TCIs) and b) topological superconductors (TSCs).

2.2 Topological crystalline insulators

Topological crystalline insulators (TCIs) [47] are gapped states of matter in which the topological character of the bulk bandstructure arises from crystalline symmetries, i.e. they cannot be adiabatically connected to the atomic limit without breaking symmetries involving spatial transformations, such as mirror reflection or rotational symmetries. As a result, specific crystalline symmetries ensure the topological protection of the metallic surface states occuring in such systems. Theoretically, TCI phases protected by mirror reflection [128],

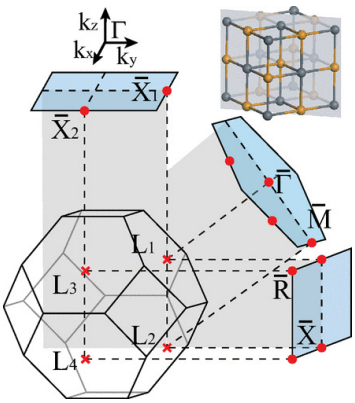

Fig. 2.1 The figure depicts the first Brillouin zone of $Pb_{1-x}Sn_xTe$, which is a truncated octahedron with six square faces and eight hexagonal faces, and represents the projection of the L-points in the bulk Brillouin zone at different points on the surfaces. Two types of surface states are depicted, depending upon whether each L-point projects to a different point on the surface. For the (001) surface, the plane $\Gamma L_1 L_2$ in the bulk Brillouin zone projects onto the symmetry line $\overline{\Gamma X}$ in the surface Brillouin zone, with both L_1 and L_2 projecting onto the $\overline{X}_1-$point. For the (111) surface, the plane $\Gamma L_1 L_2$ projects onto the line $\overline{\Gamma M}$, so there are two Dirac points along each of the three equivalent lines $\overline{\Gamma M}$. The inset shows the fcc unit cell for SnTe, with two interpenetrating lattices. (Figure has been reproduced from Ref. [52] with permission)

glide [129, 130], rotational [131] and inversion [132, 133] symmetries have been proposed, and such phases have been identified using first-principles calculations in material systems such as Ca_2As [134], $\alpha-Bi_4Br_4$ [135], a family of Zintl compounds including $Ba_3Cd_2As_4$, $Ba_3Zn_2As_4$ and $Ba_3Cd_2Sb_4$ [136], and in stacked graphene layers [137].

For the purpose of this thesis, we shall specifically focus on a class of TCIs, that are protected by reflection symmetry with respect to a crystal plane, i.e. mirror reflection symmetry [107, 51, 48, 49, 138, 50, 52]. Here the topological properties are dictated by a new integer topological invariant, known as the mirror Chern number [48, 107], which guarantees the existence of topological surface states on only those surfaces which are invariant under mirror reflection symmetry. Such a TCI state was first theoretically predicted in SnTe [48, 49], for mirror reflection symmetry with respect to the (110) mirror planes. In practice, it is known that SnTe crystals are subject to a rhombohedral distortion [48], which, strictly speaking, breaks the crystal mirror symmetries, and hence excludes a gapless TCI phase. Moreover, these are naturally hole-doped, owing to an exceptionally high concentration of electrically active Sn vacancies, which are heavily p-type, meaning that the TCI states are not occupied and thus difficult to observe in photoemission experiments [51]. Such issues can be avoided by instead considering $Pb_{1-x}Sn_xTe$ and $Pb_{1-x}Sn_xSe$ alloys, where the chemical potential can be tuned more easily. $Pb_{1-x}Sn_xTe$ crystallizes in the rock

salt crystal structure [139–143], where each of two types of atoms (Pb/Sn and Te) form separate face-centred cubic lattices, with the two lattices interpenetrating so as to form a three-dimensional checkerboard pattern. The first Brillouin zone (BZ) of the crystal structure is a truncated octahedron with six square faces and eight hexagonal faces (see Fig. 2.1). The fundamental band gaps are located at the four distinct L-point momenta, which correspond to the centres of the eight hexagonal faces of the BZ. It has long been established that the ordering of the conduction and valence bands at L-points in SnTe is inverted relative to PbTe [144], the latter being smoothly connected to the atomic limit. The topologically nontrivial character of the former has been established from first-principles calculations [48]. In the SnTe class of TCIs, topological surface states have been observed on crystal faces that are symmetric with respect to the (110) mirror planes. Three common surface terminations of IV–VI semiconductors are (001), (111), and (110). Depending on the surface orientation, there are two types of TCI surface states [52, 138], with qualitatively different electronic properties, depending on whether different L-points project to different points on the surface, or pairs of L-points project to the same point on the surface. In particular, for the (001) surface, the plane $\Gamma L_1 L_2$ in the bulk Brillouin zone projects onto the symmetry line $\overline{\Gamma X}$ in the surface Brillouin zone, with both L_1 and L_2 projecting onto the $\overline{X}_1-$point. For the (111) surface, the plane $\Gamma L_1 L_2$ projects onto the line $\overline{\Gamma M}$, so there are two Dirac points along each of the three equivalent lines $\overline{\Gamma M}$ (see Fig. 2.1).

In our analysis, we shall work with the former class of surfaces, which has been shown to harbor a double-Dirac like dispersion for the surface states [52], with two-dimensional Van Hove singularities [53].

2.3 Topological superconductors

In principle, systematic topological classifications on the basis of symmetry properties are possible for various quantum many-body systems with a gapped spectrum, and have been conducted not only for insulators but also superconductors. A fully-gapped topological superconductor (TSC) [107, 145, 105] can be defined as one that cannot be adiabatically connected to a Bose-Einstein condensate (BEC) of Cooper pairs. Conventional $s-$wave spin-singlet superconductors are therefore clearly nontopological, and unconventional superconductivity is a necessary, but not sufficient, condition for realizing a TSC. Moreover, even-parity pairing inevitably leads to topologically trivial superconductors, whereas odd-parity pairing leads to TSCs if the Fermi surface contains an odd number of time-reversal invariant momenta [146, 120]. For weak spin-orbit coupling (i.e., spin is a good quantum number), odd-parity pairing corresponds to spin-triplet pairing. As a consequence of its nontrivial topology, a TSC

is guaranteed to possess protected gapless excitations on the boundary. The classification of TSCs and the nature of their boundary excitations, which are Bogoliubov quasiparticles, depend crucially on the presence or absence of internal symmetries. In particular, both time-reversal-breaking TSCs and time-reversal-invariant TSCs are of great interest. A 2D chiral $k_x \pm ik_y$ spin-triplet superconductor [60] is an example of the former class of TSCs, which is highly sought-after owing to its exotic emergent excitations. Recently, this classification has been extended to the so-called higher-order topological superconductors [132, 147, 128], that have gapped, topological surfaces and gapless Majorana modes instead on lower-dimensional boundaries, i.e., corners of a two-dimensional system or hinges for a three-dimensional system.

A chiral superconductor is one in which the phase of the complex superconducting gap function, $\Delta(\overrightarrow{k})$, winds in a clockwise or counterclockwise sense as $\overrightarrow{k}$ moves about some axis on the Fermi surface of the underlying metal. A $k_x \pm ik_y$ gap function is an example, which precesses by $\pm 2\pi$ as $\overrightarrow{k}$ follows a closed path enclosing the k_z-axis. It is a topologically non-trivial state which exhibits distinctive topological modes at surfaces and defects. A chiral gap function breaks time-reversal symmetry and is degenerate with its time-reversed partner. In situations where the k_x and k_y gap functions are degenerate, one can form linear combinations $k_x \pm ik_y$ whose absolute value squared is isotropic. A chiral superconductor results from a spontaneous symmetry breaking between the states with the two chiralities. Chiral $p-$wave superconductivity can be realized in an effectively spinless regime [64], with the necessary ingredients being spin-momentum locking, and an induced Zeeman splitting. Low-dimensional topological superconductors can be engineered by judiciously forming heterostructures with conventional bulk $s-$wave superconductors [148], or even simpler systems such as 2D semiconductor quantum wells [149, 150] or 1D semiconducting quantum wires [151–153].

While there has been tremendous effort towards engineering topological superconductivity by means of an induced $p-$wave pairing, through, for instance, the proximity effect in topological insulators [148, 154], or hybrid structures of semiconductors and superconductors [155, 156, 150], intrinsic topological superconductors are still quite rare, with Sr_2RuO_4 [157, 158, 59, 159, 160] being a popular candidate for the material realization of such a state, although the nature of the superconducting order is still under debate [161–163]. The synthesis of topological superconductors can be accomplished via proximity-induced superconductivity at the interface of conventional superconductors and semiconductors with large spin-orbit coupling [151, 156, 150, 152, 149], or by doping topological insulators, for instance $Sn_{1-x}In_xTe$ [164, 165] and $M_xBi_2Se_3$ (M = Cu, Sr, Nb) [166, 120, 167–171]. The latter class of materials are now considered as candidates for nematic superconductivity

[172, 173, 168]. There is considerable current interest in topological insulator surfaces as an environment where two-dimensional topological superconductivity can be realized, which is protected against weak disorder by $s-$wave Cooper pairing in the bulk. This makes the superconductivity much more robust than in, say, Sr_2RuO_4 [174]. In this thesis, we have shown that in the presence of weak correlations, the electronic ground state on the (001) surface of the topological crystalline insulator (TCI) $Pb_{1-x}Sn_xTe$ corresponds to a chiral $p-$wave superconducting state [175]. Low-lying Type-II Van Hove singularities [53], peculiar to the (001) surface of this material, serve to enhance the transition temperature to values parametrically higher than those predicted by BCS theory [54]. Since the surface electronic bands are effectively spinless, $s-$wave superconductivity is precluded, unless pairing occurs between electrons in different time-reversed surface bands, which is ruled out at sufficiently low carrier densities. Here, the nontrivial Berry phases associated with the electronic wavefunctions ultimately dictate the chiral $p-$wave symmetry of the superconducting order parameter. $Pb_{1-x}Sn_xTe$ thus provides a good meeting ground for various desirable attributes, under extremely accessible conditions, which is not commonly encountered.

2.3.1 Experimental signatures of chiral $p-$wave order

A chiral $p-$wave superconductor provides a natural platform for the realization of Majorana fermions [64, 63, 176], as quasiparticle excitations, since the latter require paired systems with only one active fermionic species. Majorana fermions (MF) are their own anti-particles, and have attracted massive theoretical interest due to their non-Abelian exchange statistics, meaning that the particle exchange operations do not commute, in general. A fermionic state can be obtained as a superposition of two Majorana fermions, which are spatially separated. Such a state cannot be changed by local perturbations involving one of the Majorana constituents, but can be manipulated by a physical exchange of the Majorana fermions, thereby aiding low-decoherence topological quantum computation [177, 178]. Isolated MFs occur, in general, in vortices and on edges of effectively spinless superconducting systems with triplet pairing symmetry [145] and other systems with the same topological properties. Another avenue that may be used to realize Majorana zero modes is by forming electrostatic line defects in a chiral $p-$wave superconductor [179].

Majorana fermions provide a natural way to confirm the presence of a chiral $p-$wave superconducting order, and are evidenced by zero-bias peaks in the tunneling density of states, which may, however, be obscured by resonances from subgap states at nonzero energies, and half-integer quantized conductance plateaus in a ballistic point contact [124, 180]. Alternative strategies for confirming the presence of chiral $p-$wave superconductivity include the detection of half-quantum vortices in triplet superconductors [181, 182], broken time-

reversal symmetry in muon-spin resonance (μSR) experiments [183], spontaneous surface currents at sample edges and domain walls [184, 185], evidence for triplet superconductivity from the spin susceptibility using NMR experiments [186], and evidence for odd-parity superconductivity from the tunneling current through Josephson junctions between $s-$ and $p-$wave superconductors [187]. In this thesis, we propose a much simpler strategy to detect the presence of a chiral $p-$wave superconducting order in $Pb_{1-x}Sn_xTe$, using impurity-induced subgap bound states.

Recent point-contact spectroscopy measurements [188, 189] have confirmed the existence of superconductivity on the (001) surface of $Pb_{1-x}Sn_xTe$, indicated by a sharp fall in the resistance of the point contact below a characteristic temperature (3.7-6.5 K) [188] and the appearance of a spectral gap with coherence peak-like features, and zero-bias anomalies. Note that the existence of superconductivity in a confined geometry under a superconducting point contact cannot be characterized by a directly measurable zero resistance [188]. While the drop observed in the resistance is only about 0.1%, this could be a result of the system going superconducting locally in patches, in the absence of global phase coherence. The zero-bias peaks observed are simply a consequence of Andreev tunneling, and no further information is available regarding the nature of the superconducting order. While a scanning tunneling probe would instead directly give the tunneling density of states, an appearance of a zero-bias anomaly even in STM [155, 154, 148, 150] requires further investigation, to distinguish a Majorana bound state from other possibilities like topologically trivial Andreev bound states [190–194], or even bandstructure effects [195] and stacking faults [196]. Thus, such states may not be unambiguously identifiable using existing probes [197–200]. Besides, the conditions required for realizing Majorana zero modes might not always be feasible. For instance, realizing Majorana zero modes in long linear defects requires the physical ends of the wire to be in a topological superconducting state, which may not always be the case due to the presence of disorder and external potentials. Such Majorana bound states also may not exist for other types of surface defects, such as pointlike ones.

An alternate strategy would be to go beyond the Majorana states and instead look for impurity-induced states [201–203] for probing the superconducting order, analogous to the Yu-Shiba-Rusinov states [204, 62] realized in magnetic impurities in spin-singlet superconductors. In unconventional superconductors, such states may be realized for both magnetic and non-magnetic impurities [202], and could be used for probing the superconducting order. In the literature, there have been extensive studies on using Shiba-like states to detect a chiral $p-$wave superconducting order [205–209, 203, 20]. We address the converse question: given the presence of impurity-induced subgap bound states, when do they unambiguously indicate the presence of a chiral $p-$wave order? We find that only certain parameter regimes

for the chemical potential guarantee the existence of impurity states which crucially depend on the chiral $p-$wave nature of the superconductivity. In our analysis, we first identify the parameter regimes where superconductivity may exist on the (001) surface of $Pb_{1-x}Sn_xTe$ and show that for small changes in doping, the nature of the superconducting order can change from a topological chiral $p-$wave type to a conventional $s-$wave type. In the chiral $p-$wave superconducting state, we find two distinct parameter regimes, only one of which can be used to reliably establish the existence of chiral $p-$wave superconductivity using impurity-induced Shiba-like states. In our treatment, we obtain exact analytical expressions for the bound-state spectra and wave functions, as a function of the parameters of the system, which shed light on several notable characteristics of these bound states. We show that the azimuthal angle-dependence of the wave functions in point defects can be used to distinguish between nodal and chiral superconductors. We have obtained exact analytical expressions for the bound-state wave function in a point defect, which qualitatively agree with Ref. [207], with differences related to the localization length. Incidentally, other approximate solutions proposed in the literature based on different variational ansatzes [208, 206] are inconsistent with our exact solutions. For the case of point defects, we find that the wave function corresponding to the zero-energy bound state has an internal SU(2) rotational symmetry which makes it useful as a quantum qubit. If chiral $p-$wave superconductivity is indeed established on the surface of $Pb_{1-x}Sn_xTe$, then such qubits would be relatively easy to realize and manipulate using, say, STM tips. The above properties, together with the constraints that we impose on the parameter regimes, can help identify the nature of the surface superconducting order in $Pb_{1-x}Sn_xTe$.

Chapter 3

Competing electronic instabilities on a topological crystalline insulator surface

In this part of the thesis, we employ a multipatch parquet renormalization-group (RG) analysis for studying competing electronic instabilities on the (001) surface of $Pb_{1-x}Sn_xTe$ [175]. Depending upon the sign of the Hund's splitting, which is taken into account in our analysis, we find that away from perfect nesting, either a chiral $p-$wave superconducting state is stabilized, or none of the commonly encountered electronic instabilities occurs at the one-loop level. The topological crystalline insulator surface that we consider offers certain natural advantages from an experimental point of view. It features two-dimensional Van Hove singularities [53] that are accessible through a small change in doping, unlike, say, graphene, where a very high level of doping is required to access the Van Hove singularities. Interestingly, as we show below, the $p-$wave symmetry originates not from intrinsic Fermi surface deformations, but from the nontrivial Berry phases associated with the topological states, and is hence more robust against potential disorder as compared to, say, Sr_2RuO_4 [174].

Below, we discuss the effective surface Hamiltonian for the (001) surface of $Pb_{1-x}Sn_xTe$ (written down in Ref. [52]), the projection of the interactions in the valley-spin basis to one of the surface bands, and the corresponding low-energy theory. We then describe the parquet renormalization group analysis used for studying the possible electronic instabilities in this system due to weak repulsive interactions, and the calculation of susceptibilities for different types of order, of which we find chiral $p-$wave superconductivity to be the dominant electronic order over an extensive range of parameter space of interactions.

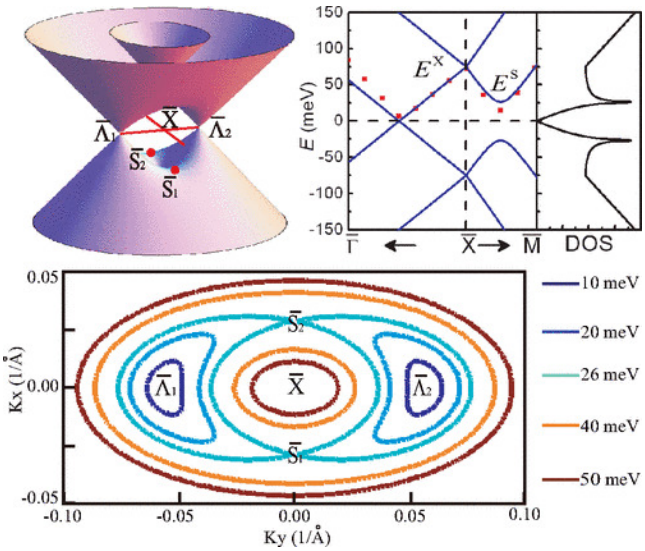

Fig. 3.1 The figure shows the k.p bandstructure in the vicinity of an $\overline{X}$ point on the (001) surface. The constant-energy contour evolves rapidly with increasing energy from the Dirac point, changing from two disconnected electron pockets to a large electron pocket and a small hole pocket via a Lifshitz transition. At this transition point, a saddle point $\overline{S}$ on the line $\overline{XM}$ leads to a Van Hove singularity in the density of states. (Figure has been reproduced from Ref. [52] with permission)

3.1 Effective surface Hamiltonian for the (001) surface of $Pb_{1-x}Sn_xTe$

The band gap minima of IV-VI semiconductors are located at the four L points in the FCC Brillouin zone. In Ref. [52], the TCI surface states are classified into two types: *Type-I*, for which all four L-points are projected to the different time-reversal invariant momenta (TRIM) in the surface Brillouin zone, and *Type-II*, for which different L-points are projected to the same surface momentum. The (001) surface belongs to the latter class of surfaces, for which the L_1 and L_2 points are projected to the $\overline{X}_1$ point on the surface, and the L_3 and L_4 points are projected to the symmetry-related $\overline{X}_2$ point. This leads to two coexisting massless Dirac fermions at $\overline{X}_1$ arising from the L_1 and the L_2 valley, respectively, and likewise at $\overline{X}_2$. The k.p Hamiltonian close to the point $\overline{X}_1$ on the (001) surface is derived on the basis of a symmetry analysis in Ref. [52], and is given by

$$H_{\overline{X}_1}(k) = (v_x k_x s_y - v_y k_y s_x) + m\tau_x + \delta s_x \tau_y, \tag{3.1}$$

where k is measured with respect to $\overline{X}_1$, $\overrightarrow{s}$ is a set of Pauli matrices associated with the two spin components associated with each valley, τ operates in valley space, and the terms m and

δ, which are off-diagonal in valley space, are added to describe intervalley scattering. The band dispersion and constant energy contours for the above surface Hamiltonian undergo a Lifshitz transition with increasing energy away from the Dirac point, and when the Fermi surface is at $\delta = 26$ meV, two saddle points $\overline{S}_1$ and $\overline{S}_2$ at momenta $(\pm\frac{m}{v_x}, 0)$ lead to a Van-Hove singularity in the density of states (see Fig. 3.1). The surface Hamiltonian corresponding to each of the $\overline{X}$ points, given in Eq. 3.1 above, comprises of four essentially spinless bands. The two bands lying closest to the chemical potential of the parent material each feature two Dirac points at $(0, \pm\sqrt{m^2+\delta^2}/v_y)$ as well as two Van Hove singularities at $(\pm m/v_x, 0)$, while the bands lying farther away in energy have a single Dirac-cone structure.

3.1.1 Projection of interactions in the valley-spin basis to a surface band

In addition to the noninteracting part of the Hamiltonian described in Eq. 3.1 above, we now consider interactions between surface electrons corresponding to different valleys and spins, which gives rise to the following terms in the Hamiltonian:

$$H_I = \frac{1}{2} \sum_{a,b,c,d,\sigma,\sigma'} U^{\sigma\sigma'}_{abcd} c^\dagger_{\sigma a} c^\dagger_{\sigma' b} c_{\sigma' c} c_{\sigma d}$$

where a, b, c, d refer to different valleys (which are either all the same, the same in pairs, or all different in the above sum), and σ, σ' refer to spins. Here, we consider $U^{\sigma\sigma'}_{abcd} = U^{\sigma\sigma'}_1$ when (a,c) belong to one $\overline{X}$ point [i.e., the L valleys corresponding to (a,c) are projected to one of the $\overline{X}$ points] and (b,d) belong to the other $\overline{X}$ point. Similarly, $U^{\sigma\sigma'}_{abcd} = U^{\sigma\sigma'}_2$ when (b,c) belong to one $\overline{X}$ point and (a,d) belong to the other, $U^{\sigma\sigma'}_3$ when (a,b) belong to one $\overline{X}$ point and (c,d) to the other, and $U^{\sigma\sigma'}_4$ when a, b, c, and d all correspond to L points projected to the same $\overline{X}$ point. The interactions depend only on the relative orientations of the spins, for example, $U^{\sigma\sigma'}$ can be written as $U^{\sigma\sigma}\delta_{\sigma\sigma'} + U^{\sigma\overline{\sigma}}(1-\delta_{\sigma\sigma'})$. In our analysis, we have projected the interactions between electrons in the valley-spin picture to the positive-energy band lying closest to the Van-Hove singularities. The resulting multiplicative form factors $u_{\sigma ai}$ (for a transformation from valley a, spin σ to the ith band) lend a momentum dependence to the effective pairing interactions obtained upon projection. We find that the spin $\uparrow$ components of the form factors have an $\exp[i\theta_k]$ dependence in momentum space and transform as $\ell = 1$ objects, whereas the phase of the spin $\downarrow$ components remains unchanged upon advancing by an angle of 2π around the $\overline{X}_i$ $(i = 1, 2)$ points, and these show an $\ell = 0$ angular dependence. These additional phase factors arise from the Berry phases associated with the surface states of the crystalline topological insulator. After projecting to the two

bands intersecting the Fermi level, we obtain the following low-energy theory

$$
\begin{aligned}
L = & \sum_{i,\sigma,\sigma'} \psi_i^\dagger (\partial_\tau - \varepsilon_k + \mu) \psi_i - \sum_i \sum_{\sigma,\sigma'} \frac{1}{2} h_4^{\sigma\sigma'} \psi_i^\dagger \psi_i^\dagger \psi_i \psi_i - \sum_{i \neq j} \sum_{\sigma,\sigma'} \frac{1}{2} [h_1^{\sigma\sigma'} \psi_i^\dagger \psi_j^\dagger \psi_i \psi_j \\
& + h_2^{\sigma\sigma'} \psi_i^\dagger \psi_j^\dagger \psi_j \psi_i + h_3^{\sigma\sigma'} \psi_i^\dagger \psi_i^\dagger \psi_j \psi_j] \\
= & \sum_i \psi_i^\dagger (\partial_\tau - \varepsilon_k + \mu) \psi_i - (h_4^0 + h_4^1) \psi_i^\dagger \psi_i^\dagger \psi_i \psi_i - \sum_{i \neq j} [(h_1^0 + h_1^1) \psi_i^\dagger \psi_j^\dagger \psi_i \psi_j \\
& + (h_2^0 + h_2^1) \psi_i^\dagger \psi_j^\dagger \psi_j \psi_i + (h_3^0 + h_3^1) \psi_i^\dagger \psi_i^\dagger \psi_j \psi_j]
\end{aligned} \tag{3.2}
$$

with $h_r^0 = \frac{1}{2} \sum_\sigma h_r^{\sigma\sigma}$and $h_r^1 = \frac{1}{2} \sum_\sigma h_r^{\sigma\overline{\sigma}}$, where the quadratic noninteracting part comes from the model in Eq. 3.1. The chemical potential value $\mu = 0$ corresponds to the system being doped to the Van Hove singularities. Here h_4 refers to scattering processes between different valleys within a band i, whereas h_1, h_2 and h_3 respectively refer to exchange processes, Coulomb interactions and pair hopping between electrons corresponding to the different bands under consideration. These processes are pictorially depicted in Fig. 3.2. Due to the distinct phase dependences associated with the form factors corresponding to spins $\uparrow$ and $\downarrow$, the effective interactions h_r after projection to the low-energy bands also either have a phase factor of $\exp[i(\theta_k - \theta_{k'})]$ (for spin-antiparallel configurations) and behave as $\ell = 1$ objects, or have no additional phase factors (for spin-parallel configurations) and behave as $\ell = 0$ objects. The coupling constants $h_r^0 \propto h_r^{\sigma\sigma}$ and $h_r^1 \propto h_r^{\sigma\overline{\sigma}}$, respectively, correspond to $\ell = 0$ and 1 angular momentum components of the interaction in our simplified model in Eq. 3.2 above. It is important to note that although the surface bands are effectively spinless, we associate spin indices $\sigma\sigma'$ with the interactions h_r in the different scattering channels r, due to the phase dependences associated with interactions between electrons with different spin configurations. In doing so, we allow for the Coulomb interactions between electrons to depend on the spin configuration being considered, thereby incorporating the effects of Hund's splitting of interactions in our treatment.

3.2 Parquet renormalization group approach for weak repulsive interactions

In BCS theory of superconductivity, the interaction between fermions and lattice vibrations effectively creates an attractive interaction between two fermions, leading to the formation of Cooper pairs. In high-T_c superconductors, on the other hand, the electron-phonon interaction is too weak to account for the observed transition temperatures, and non-phononic pairing mechanisms [210, 211] have been widely discussed. Here, we shall discuss one such possible

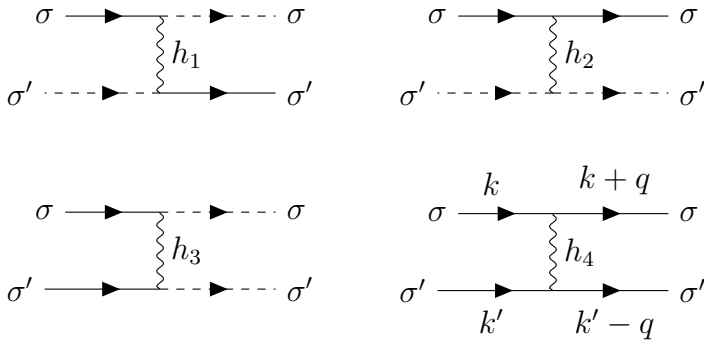

Fig. 3.2 The figure shows the different types of Coulomb interaction processes in our low-energy model. The solid lines and dashed lines denote two different patches $\overline{X}_1$ and $\overline{X}_2$ in momentum space on the (001) surface. All the vertices have momentum dependences as indicated for h_4. The σ's refer to the particular spin components of the (spinor) wave functions associated with the bands under consideration.

approach for pairing, which assumes the presence of multiple competing orders, such as superconductivity and density-wave instabilities, with fluctuations developing simultaneously at comparable energy scales. These give a progressively larger contribution to the pairing channel, and below some characteristic energy scale internally set by the system, the interaction becomes effectively attractive. The corrections to different couplings from the particle-particle and particle-hole channels, for lower and lower energies, can be analyzed using a parquet renormalization-group (RG) [57, 58] approach, which treats the different competing orders on an equal footing. This is a weak coupling approach, which involves summing series of logarithmically singular contributions to the the pairing interaction, and within which one can determine whether superconductivity is the leading instability or a density-wave order develops at a higher energy scale.

In real systems, such an approach becomes important whenever there is nesting between different pockets of the Fermi surface. For a nesting vector Q, this leads to a logarithmic divergence at zero frequency or zero temperature in the particle-hole bubble $\Pi_{ph}(Q)$, similar to the one that is always present in the particle-particle channel $\Pi_{pp}(0)$. The susceptibilities in these competing channels are given by

$$\Pi_{pp}(0,E) = -i \int \frac{d^2k d\omega}{(2\pi\hbar)^3} G^c(k,\omega+E) G^c(-k,-\omega)$$

and

$$\Pi_{ph}(Q,E) = i \int \frac{d^2k d\omega}{(2\pi\hbar)^3} G^c(k,\omega) G^f(k+Q,\omega+E)$$

where the two-point correlation function $G^{c,f} = \frac{1}{\omega - \varepsilon^{c,f}/\hbar + i\delta sgn[\omega]}$, with c and f corresponding to particles and holes respectively. When $\varepsilon^c(k) = -\varepsilon^f(k+Q)$, $\Pi_{pp}(0,E), \Pi_{ph}(Q,E) \sim \log[\frac{\Lambda}{E}]$ where E is the typical energy of external fermions, and Λ is the fermionic bandwidth. In the parquet RG approach, E is considered as a running variable, assuming its initial value to be comparable to the bandwidth Λ. The renormalization group procedure is performed for energies E that far exceed the Fermi energy E_F, and so the vertex functions in this approach depend only on the energy E and not on the momenta on the arms of the vertices. The couplings diverge at a critical energy scale, which indicates the approach towards an ordered ground state. We find that the parquet renormalization group approach is suitable for investigating possible electronic instabilities in our system, due to the presence of Fermi-surface nesting between the $\overline{X}$ points on the (001) surface, which opens up the possibility of competing density-wave instabilities.

3.3 Renormalization group analysis

To study the possible instabilities in this system, we construct a two-patch renormalization group for the interaction vertices, where the instability is indicated in the form of a pole in the vertex function. We consider only the electrons near the saddle points at $\overline{X}_1$ and $\overline{X}_2$ on the (001) surface. As discussed in the previous section, we distinguish between coupling constants with different spin combinations ($\uparrow\uparrow$ or $\uparrow\downarrow$) and write separate RG equations for the two kinds of interactions. Due to the transformation properties of the corresponding interactions, i.e. $\ell = 0$ or $\ell = 1$, we shall henceforth refer to $h_r^{\sigma\sigma}$ (where $\sigma = \uparrow, \downarrow$) as h_r^0 and $h_r^{\sigma\overline{\sigma}}$ as h_r^1.

We perform RG analysis up to one-loop level, integrating out high-energy degrees of freedom gradually from an energy cutoff Λ, which is the bandwidth. The susceptibilities in the different channels schematically behave as $\chi_0^{pp}(\omega) \sim \ln[\Lambda/\omega]\ln[\Lambda/\max(\omega, E_F)]$, $\chi_Q^{ph}(\omega) \sim \ln[\Lambda/\max(\omega, E_F)]\ln[\Lambda/\max(\omega, E_F, t)]$ and $\chi_0^{ph}(\omega), \chi_Q^{pp}(\omega) \sim \ln[\Lambda/\max(\omega, E_F)]$, where ω denotes the energy away from the Van Hove singularities, E_F refers to the Fermi energy, and t represents terms in the Hamiltonian that destroy the perfect nesting. We use $y \equiv \ln^2[\Lambda/\omega] \sim \chi_0^{pp}$ as the RG flow parameter, and describe the relative weight of the other channels as $d_1(y) = \frac{d\chi_Q^{ph}}{dy}$, $d_2(y) = \frac{d\chi_0^{ph}}{dy}$ and $d_3(y) = -\frac{d\chi_Q^{pp}}{dy}$. In our treatment, $d_1(y)$ is taken to be a function $\frac{1}{\sqrt{1+y}}$, interpolating smoothly in between the limits $d_1(y=0) = 1$ and $d_1(y \gg 1) = \frac{1}{\sqrt{y}}$, and $d_2, d_3 \ll d_1$. The multiplicative factor $d_1(y)$ essentially incorporates the effects of imperfect nesting in our analysis. The RG equations are obtained by evaluating second-order diagrams and collecting the respective combinatoric prefactors, for each of

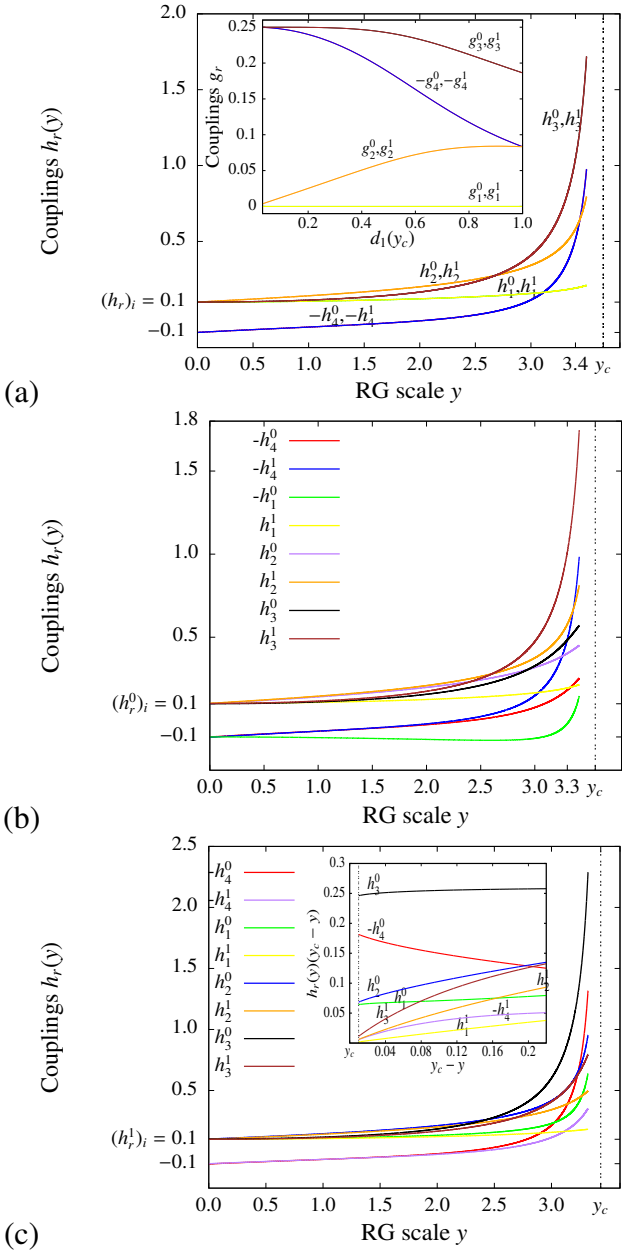

Fig. 3.3 The figure shows the flow of couplings with renormalization-group scale y, starting with repulsive interactions. In (a), the couplings in different angular momentum channels (h_r^0 and h_r^1) are assumed to be degenerate initially, at $(h_r^{0,1})_{initial} = 0.1$. The inset shows the evolution of the fixed-point couplings g_r^ℓ ($\ell = 0, 1$) as a function of $d_1(y_c)$ ($= \frac{1}{\sqrt{1+y_c}}$), which is the ratio of the particle-hole to particle-particle susceptibilities at the fixed point y_c. In (b), the $\ell = 1$ components of all the couplings are chosen to be larger than the $\ell = 0$ components by 2% initially, i.e. $\frac{|h_r^1 - h_r^0|}{|h_r^0|} = 0.02$, where $(h_r^0)_{initial} = 0.1$. In (c), the $\ell = 0$ components of all the couplings are chosen to be larger than the $\ell = 1$ components by 2% initially, i.e. $\frac{|h_r^0 - h_r^1|}{|h_r^1|} = 0.02$, where $(h_r^1)_{initial} = 0.1$. The inset in (c) shows the behavior of $h_r(y)(y_c - y)$ as a function of $(y_c - y)$ close to the fixed point y_c. The y-intercepts of the different curves show the fixed-point values g_r^ℓ for the couplings $h_r^\ell(y)$. We find pair hopping between patches (h_3) and on-patch scattering (h_4) to be the dominant scattering channels in all cases, irrespective of the initial conditions for the different scattering channels h_r ($r = 1 - 4$). In $\ell = 1$ and $\ell = 0$ components of h_3 and $(-h_4)$ dominate in (b) and (c), respectively.

the interactions h_1, h_2, h_3 and h_4. The diagrams corresponding to the renormalization of the interaction h_2 are shown in Fig. 3.4. The RG equations obtained are given by (where we have used the notation $\sigma\sigma \equiv 0$ and $\sigma\overline{\sigma} \equiv 1$ for each of the couplings)

$$\frac{dh_1^0}{dy} = 2d_1(-(h_1^0)^2 - (h_3^1)^2 - (h_1^1)^2 + 2h_1^0h_2^0 + (h_3^0)^2) \tag{3.3}$$

$$\frac{dh_1^1}{dy} = 2d_1(-2h_1^0h_1^1 + 2h_1^1h_2^0), \tag{3.4}$$

$$\frac{dh_2^0}{dy} = 2d_1((h_2^0)^2 + (h_3^0)^2), \tag{3.5}$$

$$\frac{dh_2^1}{dy} = 2d_1((h_2^1)^2 + (h_3^1)^2), \tag{3.6}$$

$$\frac{dh_3^0}{dy} = -4h_4^0h_3^0 + 2d_1(4h_2^0h_3^0 - 2h_1^1h_3^1), \tag{3.7}$$

$$\frac{dh_3^1}{dy} = -4h_4^1h_3^1 + 2d_1(2h_2^1h_3^1 - 2h_1^0h_3^1 + 2h_2^0h_3^1), \tag{3.8}$$

$$\frac{dh_4^0}{dy} = -2((h_4^0)^2 + (h_3^0)^2), \tag{3.9}$$

$$\frac{dh_4^1}{dy} = -2((h_4^1)^2 + (h_3^1)^2). \tag{3.10}$$

These coupled differential equations are then solved, starting from initial values of interactions in the weak-coupling regime ($h_i^0 = h_i^1 \sim 0.1$). The results of our RG analysis for the cases where (a) the couplings in the $\ell = 0$ and $\ell = 1$ channels are chosen to be degenerate initially, (b) the couplings in the $\ell = 1$ channel are chosen to dominate initially, and (c) the couplings in the $\ell = 0$ channel are chosen to dominate initially, are illustrated in Fig. 3.3. The RG flows are found to be extremely sensitive to the sign of the Hund's splitting, and the final set of dominant couplings g_r^ℓ near the critical point of the RG correspond to the value of ℓ which has been chosen to dominate initially. In contrast, the results are remarkably insensitive to the magnitude as well as sign of an initial splitting introduced between the couplings h_r corresponding to the different scattering channels $r = 1-4$. This feature is illustrated in Fig. 1 in Appendix-A.

Each of the couplings associated with the RG flow has an asymptotic form $h_r^\ell(y) = \frac{g_r^\ell}{y_c - y}$ near the the critical point y_c of the RG flow. In order to determine the behavior of the fixed point values g_r^ℓ for the different couplings as a function of $d_1(y_c)$, we substitute this asymptotic form into the RG equations to obtain polynomial equations, which are illustrated in Appendix-A. These coupled equations are then solved with appropriate initial conditions, to determine g_r^ℓ ($\ell = 0, 1$) as a function of $d_1(y_c)$, which is the ratio of the particle-hole and

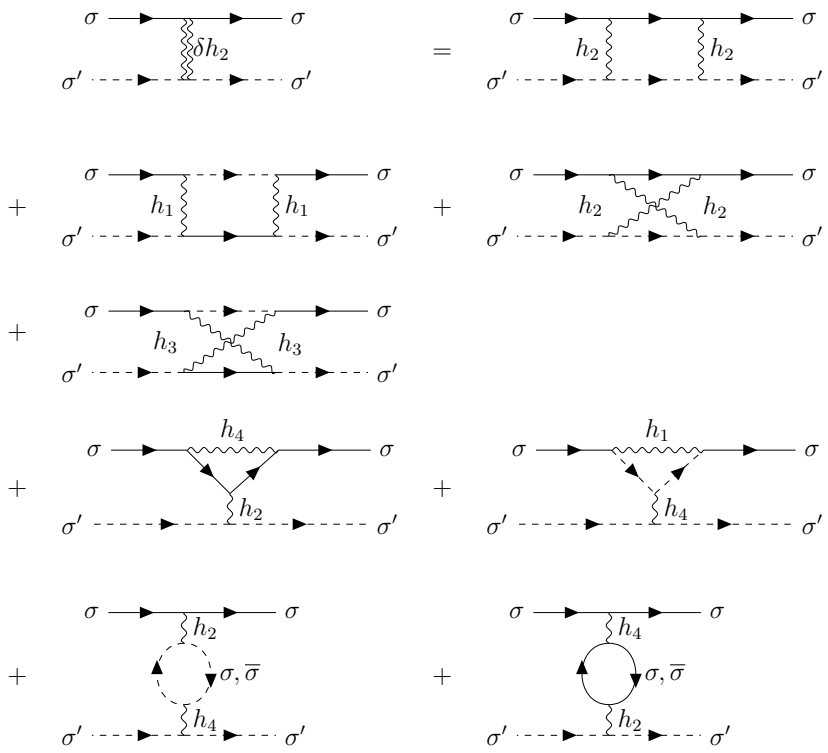

Fig. 3.4 The figure shows the diagrams for one-loop renormalization of the coupling h_2. The diagrams for h_1, h_3 and h_4 are similarly obtained.

particle-particle susceptibilities at the fixed point y_c. The behavior of g_r^ℓ as a function of $d_1(y_c)$ when all the couplings are chosen to be degenerate initially, is shown in the inset in Fig. 3.3 (a). The corresponding behavior when the degeneracy between the couplings in the $\ell = 0$ and $\ell = 1$ channels is lifted (such that $g_r^0 > g_r^1$ for all i) is shown in Fig. 2 in Appendix-A (here we have only shown the behavior of the couplings g_r^0, as the fixed-point values g_r^1 turn out to be very small in this case).

3.3.1 Susceptibilities for different types of order

We now investigate the instabilities of the system by evaluating the susceptibilities χ for various types of order, introducing infinitesimal test vertices corresponding to different kinds of pairing into the action, such as $\triangle_a \psi^\dagger_{a\sigma} \psi^\dagger_{a\sigma'} + \triangle^*_a \psi_{a\sigma} \psi_{a\sigma'}$ for the patch $a = 1, 2$ (where the spin labels σ, σ' are meant to simply denote the presence or absence of the phase factors $\exp[i\theta_k]$) corresponding to particle-particle pairing on the patch.

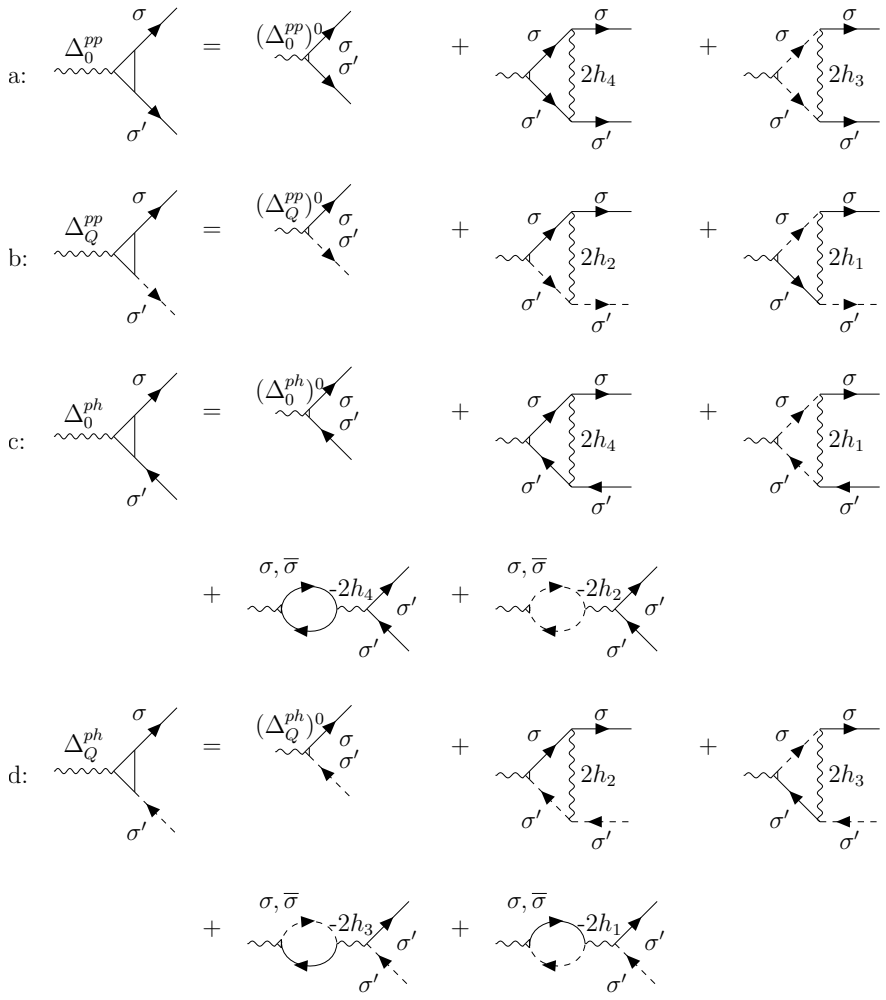

Fig. 3.5 The figure shows the test vertex renormalization corresponding to (a) particle-particle pairing on the patch, (b) particle-particle pairing between patches, (c) particle-hole pairing on the patch and (d) particle-hole pairing between patches, where Q refers to the nesting vector between the patches $\overline{X}_1$ and $\overline{X}_2$ in two dimensions.

The renormalization of the test vertex for particle-particle pairing on a patch is governed by the equation

$$\frac{\partial}{\partial y}\begin{pmatrix}\Delta_1\\ \Delta_2\end{pmatrix} = 2\begin{pmatrix}h_4^1 & h_3^1\\ h_3^1 & h_4^1\end{pmatrix}\begin{pmatrix}\Delta_1\\ \Delta_2\end{pmatrix} \tag{3.11}$$

since we can only consider Cooper pairing in the p-wave channel for spinless electrons. By transforming to the eigenvector basis, we can obtain different possible order parameters, and choose the one corresponding to the most negative eigenvalue. The vertices with positive eigenvalues are suppressed under RG flow.

We diagonalize the Eq. 3.11 above and substitute the asymptotic form of the interactions in the most negative eigenvalue. This gives us the exponent α for the divergence of the susceptibility $\chi \propto (y_c - y)^{\alpha}$ for p-wave superconductivity. The renormalization of the test vertex corresponding to particle-hole pairing between the patches, in the $\ell = 0$ channel is given by

$$\frac{\partial}{\partial y}\begin{pmatrix}\Delta_{12}\\ \Delta_{21}\end{pmatrix} = -2d_1(y)\begin{pmatrix}h_2^0 - h_1^0 - h_1^1 & -h_3^1\\ -h_3^1 & h_2^0 - h_1^0 - h_1^1\end{pmatrix}\begin{pmatrix}\Delta_{12}\\ \Delta_{21}\end{pmatrix} \tag{3.12}$$

and in the $\ell = 1$ channel, by

$$\frac{\partial}{\partial y}\begin{pmatrix}\Delta_{12}\\ \Delta_{21}\end{pmatrix} = -2d_1(y)\begin{pmatrix}h_2^1 & h_3^1\\ h_3^1 & h_2^1\end{pmatrix}\begin{pmatrix}\Delta_{12}\\ \Delta_{21}\end{pmatrix} \tag{3.13}$$

The renormalization of the test vertex corresponding to particle-particle pairing between the patches, in the $\ell = 0$ channel, is given by

$$\frac{\partial}{\partial y}\begin{pmatrix}\Delta_{12}\\ \Delta_{21}\end{pmatrix} = 2d_3(y)\begin{pmatrix}h_2^0 & h_1^0\\ h_1^0 & h_2^0\end{pmatrix}\begin{pmatrix}\Delta_{12}\\ \Delta_{21}\end{pmatrix} \tag{3.14}$$

and in the $\ell = 1$ channel, by

$$\frac{\partial}{\partial y}\begin{pmatrix}\Delta_{12}\\ \Delta_{21}\end{pmatrix} = 2d_3(y)\begin{pmatrix}h_2^1 & h_1^1\\ h_1^1 & h_2^1\end{pmatrix}\begin{pmatrix}\Delta_{12}\\ \Delta_{21}\end{pmatrix} \tag{3.15}$$

The renormalization of the test vertex corresponding to particle-hole pairing on a patch, in the $\ell = 0$ channel, is given by

$$\frac{\partial}{\partial y}\begin{pmatrix}\Delta_1\\ \Delta_2\end{pmatrix} = -2d_2(y)\begin{pmatrix}-h_4^1 & h_1^0 - h_2^0 - h_2^1\\ h_1^0 - h_2^0 - h_2^1 & -h_4^1\end{pmatrix}\begin{pmatrix}\Delta_1\\ \Delta_2\end{pmatrix} \tag{3.16}$$

and in the $\ell = 1$ channel, is given by

$$\frac{\partial}{\partial y}\begin{pmatrix}\Delta_1\\ \Delta_2\end{pmatrix} = -2d_2(y)\begin{pmatrix}h_4^1 & h_1^1\\ h_1^1 & h_4^1\end{pmatrix}\begin{pmatrix}\Delta_1\\ \Delta_2\end{pmatrix} \tag{3.17}$$

The diagrams corresponding to the renormalization of the different kinds of pairing vertices are shown in Fig. 3.5. The most negative eigenvalue for Cooper pairing on the patch is given by $2(-h_3^1+h_4^1)$ which corresponds to the eigenvector $\frac{1}{\sqrt{2}}\begin{pmatrix}-1 & 1\end{pmatrix}$, competing with those for CDW and SDW order, given by $-2(h_3^1-h_1^0-h_1^1+h_2^0)d_1(y)$ (corresponding to the eigenvector $\frac{1}{\sqrt{2}}\begin{pmatrix}-1 & 1\end{pmatrix}$) and $-2(h_3^1+h_2^1)d_1(y)$ (corresponding to the eigenvector $\frac{1}{\sqrt{2}}\begin{pmatrix}1 & 1\end{pmatrix}$) respectively. This is followed by particle-hole pairing on a patch in the $\ell = 0$ channel, with the more negative eigenvalue given by $-2(-h_4^1-(h_1^0-h_2^0-h_2^1))d_2(y)$ (corresponding to the eigenvector $\frac{1}{\sqrt{2}}\begin{pmatrix}-1 & 1\end{pmatrix}$). Thus, the dominant instability of our system, namely p-wave superconductivity, appears in the $\ell = 1$ channel, whereas the dominant coupling in the $\ell = 0$ channel does not lead to any instability due to the absence of s- or d-wave superconductivity on the patch.

The exponents for intrapatch p-wave pairing, charge-density wave (CDW), spin-density wave (SDW), uniform spin, charge compressibility (κ) and finite-momentum π pairing are given by-

$$\begin{aligned}
\alpha_{\rm pw} &= 2(-g_3^1+g_4^1),\\
\alpha_{\rm CDW} &= -2(g_3^1-g_1^0-g_1^1+g_2^0)d_1(y_c),\\
\alpha_{\rm SDW} &= -2(g_3^1+g_2^1)d_1(y_c),\\
\alpha_{\kappa} &= -2(-g_4^1-(g_1^0-g_2^0-g_2^1))d_2(y_c),\\
\alpha_{s} &= -2(g_4^1+g_1^1)d_2(y_c),\\
\alpha_{\pi}^0 &= 2(g_2^0-g_1^0)d_3(y_c),\\
\alpha_{\pi}^1 &= 2(g_2^1-g_1^1)d_3(y_c).
\end{aligned} \tag{3.18}$$

The p-wave order here is chiral since its symmetry is dictated by the aforementioned $\exp[i\theta_k]$ dependence of the Berry phase factors in the wave functions. Note that this is a finite-momentum pairing, with each patch $\overline{X}_i$ located at a finite momentum with respect to the $\overline{\Gamma}$ point on the surface. Furthermore, the relative phase of the p-wave order on different patches is π, which means that we have $d-$wave order between the patches. Comparison between the values of the exponents for p-wave pairing, SDW, CDW and charge compressibility, as a function of $d_1(y_c)$ shows that the most divergent susceptibility is p-wave superconductivity

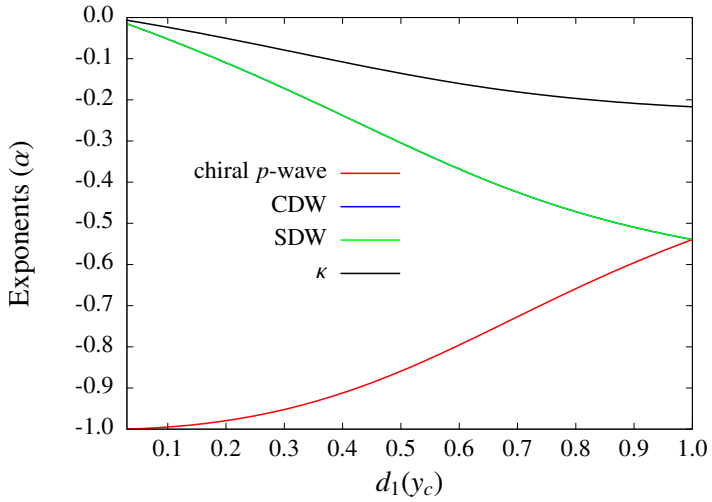

Fig. 3.6 The exponents α, which are negative, corresponding to the various susceptibilities: chiral $p-$wave superconductivity, CDW, SDW, and uniform charge compressibility (κ), plotted as a function of $d_1(y_c)$ for the case in which each of the couplings g_r^ℓ for $r = 1-4$ and $\ell = 0,1$ is degenerate. The order of these exponents indicates that chiral $p-$wave superconductivity is the leading instability (with the most negative exponent α_{pw}) throughout, and CDW and SDW have nearly the same values of exponents α in this case.

throughout the parameter range $0 < d_1(y_c) < 1$ (see fig. 3.6). The CDW and SDW instabilities show a weaker divergence, and are followed by charge compressibility. The exponents for uniform spin susceptibility and π pairing are always positive and hence, these orders are suppressed. In the case of perfect nesting, i.e. $d_1 = 1$, the SDW and CDW instabilities become degenerate with p-wave superconductivity.

Now, if a finite Hund's splitting is introduced initially such that $h_r^1 > h_r^0$, the above analysis holds and $p-$wave superconductivity is still the dominant instability. However, for an initial Hund's splitting of the opposite sign, i.e. $h_r^0 > h_r^1$, we find that the dominant couplings g_r^ℓ at the instability threshold correspond to $\ell = 0$ (see fig. 3.3 (b) and (c)). In this case, the exponents α for each of the susceptibilities χ turn out to be either positive or numerically close to zero. This is due to subtle cancellations between contributions from the dominant couplings in different scattering channels. Thus, none of the instabilities considered above are found to occur in this case within the one-loop approximation. Clearly, the nature of instabilities in this system is crucially dependent on the sign of the Hund's splitting.

3.4 Effect of an external magnetization

Here, we address the question of how robust such a superconducting order is against a time-reversal symmetry breaking perturbation, such as proximity coupling to an external

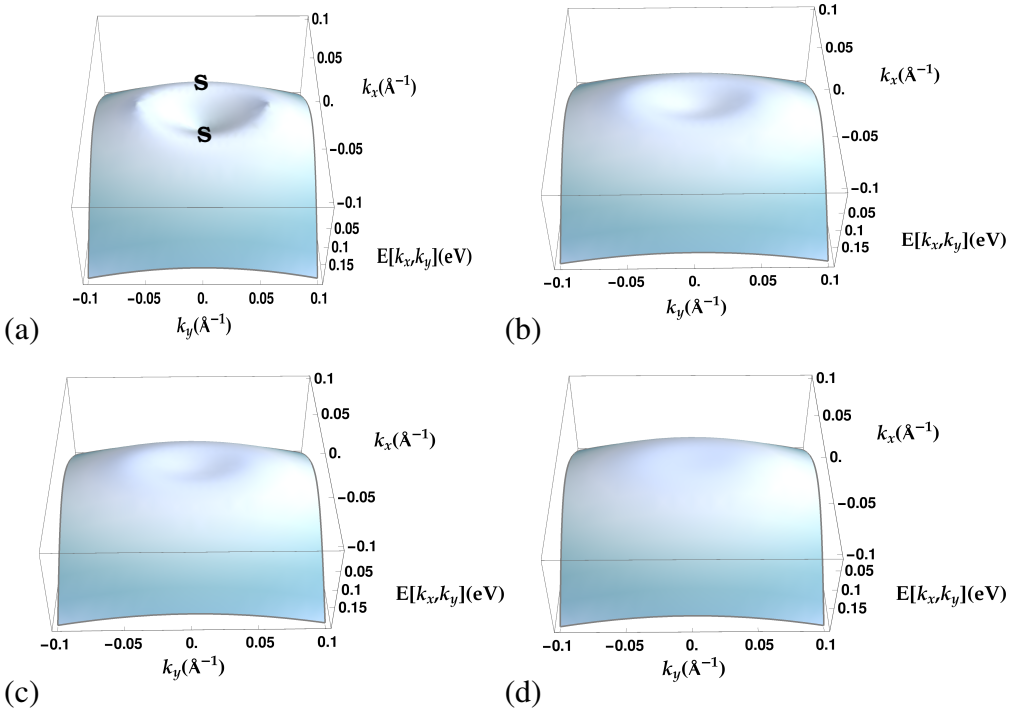

Fig. 3.7 The two-dimensional Van-Hove singularities on the TCI surface (indicated by '**S**') for (a) $M = 0.0$, (b) $M = 0.04$, (c) $M = 0.05$, and (d) $M = 0.07$ (in eV) where $v_x = 2.4$ eV $\mathring{A}^{-1}$, $v_y = 1.3$ eV $\mathring{A}^{-1}$, $m = 0.07$ eV and $\delta = 0.026$ eV (values taken from Ref. [52]). We find that beyond $M \approx 0.05$ eV, there are no Van-Hove singularities in the surface electronic spectrum.

magnetization [212]. We show that the robustness of the surface superconducting order against an external magnetization is enhanced by the presence of a finite Hund's interaction. Specifically, the critical value of spin-splitting (induced by the magnetization), beyond which p-wave superconductivity is no longer possible, scales directly with the size of the Hund's splitting with respect to the repulsive electron interaction strength.

We introduce the effect of an external magnetization by adding a Zeeman splitting term M to the noninteracting Hamiltonian in Eq. 3.1. In the presence of such a spin-splitting term, the degeneracy between spins $\uparrow$ and $\downarrow$ is broken, and the complex form factors $u_\uparrow$ and $u_\downarrow$ differ both in amplitude and phase. This gives rise to additional components for the couplings h_r. To simplify our analysis, we have integrated out the momentum-dependence of the absolute values of the form factors $|u_\uparrow(\overrightarrow{k},M)|^2$ and $|u_\downarrow(\overrightarrow{k},M)|^2$ for the two spin components, over a suitable range of two-dimensional momenta (k_x,k_y) around the $\overline{X}$ points (see fig. 3.7), and normalized the results with respect to $|u_\uparrow(\overrightarrow{k},0)|^2$ and $|u_\downarrow(k,0)|^2$ respectively. Henceforth, we shall denote these k-integrated form factors by $v_\uparrow$ and $v_\downarrow$ for simplicity. The couplings constants h_r associated with the RG flows either involve two factors of either $v_\uparrow$ or $v_\downarrow$, or one factor of each. Clearly, for $M>0$, we have $v_\uparrow(M)>1$ and $v_\downarrow(M)<1$ for the positive energy eigenstates, and the ratio $\frac{v_\uparrow(M)}{v_\downarrow(M)}$ increases with an increase in M. Corresponding to every scattering channel h_r, we then have four components $h_r^{\uparrow\uparrow}$, $h_r^{\downarrow\downarrow}$, $h_r^{\uparrow\downarrow}$ and $h_r^{\downarrow\uparrow}$, alternately denoted by h_r^0, h_r^2, h_r^1 and h_r^3 respectively. This gives us a set of 16 coupling constants. For $M \gtrsim 0.05$ eV, one also has to take into account the absence of the Van-Hove singularities in the spectrum (as illustrated in Fig. 3.7). We have performed calculations for higher values of magnetization as well, and found that the qualitative behavior of the system in that regime is very similar to what we discuss below. Therefore, we confine our attention to situations where Van-Hove singularities are present, since that gives us high transition temperatures even in the weak-coupling regime. The final set of RG equations obtained by taking into account the multiplicative factors v_σ and $v_{\overline{\sigma}}$ are given in Appendix-A. To determine the possible electronic instabilities in this system, we evaluate the susceptibilities χ for various types of order, as before, by writing down renormalization equations for the corresponding test vertices, although the total number of instabilities possible increases in this case due to the lifting of spin degeneracy by the Zeeman splitting term in the Hamiltonian. The exponents α for different types of pairing now also involve the $k-$integrated form factors.

3.4.1 Ladder RG equations in the absence of Hund's splitting

Let us first consider a situation where the various components of interactions h_r in the different scattering channels $r=1-4$ are taken to be identical initially, with no Hund's

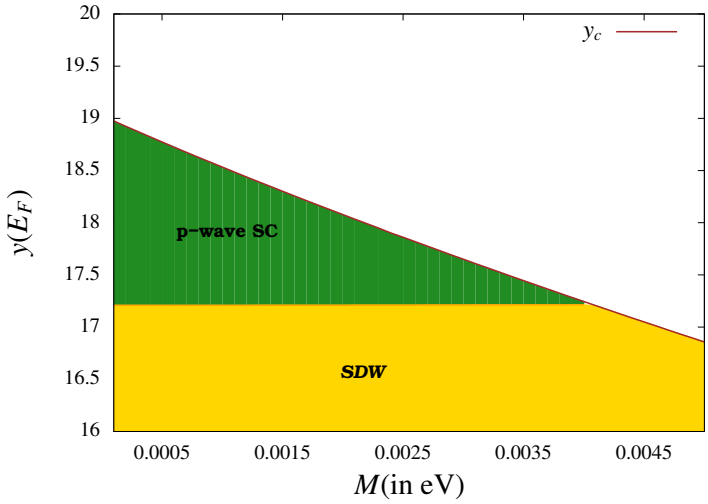

Fig. 3.8 The phase diagram for $y(E_F)$ as a function of the spin-splitting M when the initial value of each of the dimensionless RG couplings is chosen to be equal to 0.03. This shows that for large electron densities, it is possible to stabilize $p-$wave superconductivity for a range of values of the Fermi energy E_F, up till $M \sim 4$ meV (in this case). The values on the y-axis as well as the value of M up to which p-wave superconductivity may be stabilized depend on the initial interaction strength. The latter decreases with an increase in the strength of electronic interactions.

splitting present. In this case, we find that even for a very small value of Zeeman splitting M, the leading components of the different kinds of interactions near the fixed point y_c correspond to spin $\uparrow$ (i.e. the $\ell = 0$ channel). Now, if we introduce test vertices for different kinds of pairing and calculate the exponents for the divergence of the respective susceptibilities, we find that each of the exponents α is either positive or numerically close to zero. This indicates the absence of any electronic instabilities in this case. Clearly, p-wave superconductivity cannot be stabilized at energies corresponding to the fixed point of the parquet RG. However, when the Fermi energy E_F associated with the system exceeds the energy ω_c corresponding to the critical point y_c, the RG flow must be terminated at E_F, and any possible instabilities will then depend on the order of the different couplings at the Fermi energy. These are determined using a ladder RG approach, which is described in detail in Ref. [213].

Two kinds of vertices continue to flow logarithmically at energies below the Fermi energy E_F: vertices with zero total momentum, and with total momentum exactly equal to the nesting vector Q in two dimensions. The vertices with zero total momentum are the h_3 and h_4 terms in our RG analysis and the vertices with total momentum Q are the h_1, h_2 and h_3 terms. The values of h_r at E_F act as the bare couplings for the theory at $\omega < E_F$. There are two kinds of h_3 vertices with a momentum transfer Q, h_{3a} and h_{3b} and we denote the h_3 vertex with zero total momentum as h_{3c}. We shall refer to the vertices with zero total momentum

as $h_r(0)$ and the vertices with total momentum Q as $h_r(Q)$. The ladder RG equations are obtained by considering those diagrams which still yield a logarithmic divergence.

The ladder RG equations for our system, where now $y \equiv \ln[\frac{E_F}{\omega}]$, are given in Appendix-B. These equations can be solved to give

$$h_3^{\sigma\overline{\sigma}}(0) - h_4^{\sigma\overline{\sigma}}(0) = \frac{(h_3^{\sigma\overline{\sigma}})_{E_F} - (h_4^{\sigma\overline{\sigma}})_{E_F}}{1 - 2v_\sigma v_{\overline{\sigma}}((h_3^{\sigma\overline{\sigma}})_{E_F} - (h_4^{\sigma\overline{\sigma}})_{E_F})\log[\frac{E_F}{\omega}]}$$

for the superconducting vertex. A similar situation arises for the SDW instability in this regime. The competition between these instabilities depends on the respective energies at which different combinations of couplings diverge, and thus, on their values at the Fermi energy E_F. The first instability occurs in the channel for which the coupling at $\omega \sim E_F$ is the largest.

Thus, we find that for relatively large electron densities, when the Fermi energy E_F exceeds the energy (ω_c) corresponding to the critical point of the RG flow y_c, p-wave superconducting order can be stabilized on the TCI surface up to a small value of the spin-splitting M ($\sim$ 1 meV). For larger values of Zeeman splitting introduced by an external magnetization, we find that a spin density wave (SDW) modulation may be possible over and above the expected uniform spin polarization on the surface, if the number density of electrons is sufficiently large. Although p-wave superconductivity is degraded even by an infinitesimal external magnetization in the absence of Hund's splitting, it is thus possible to stabilize this phase over a range of electron densities (and corresponding Fermi energies E_F). A phase diagram for $y(E_F)$ as a function of the spin-splitting term M is shown in Fig. 3.8 for an initial value of 0.03 for each of the dimensionless couplings. It should be noted that the exact values on the $y-$axis, as well as the value of spin-splitting M (on the x-axis) beyond which p-wave superconductivity is no longer possible, are both dependent on the initial interaction strength being considered. In particular, we find that the range of values of M for which $p-$wave superconductivity may be stabilized decreases with an increase in the strength of electronic interactions.

3.4.2 Critical value of Zeeman splitting for a finite Hund's splitting

For a multiorbital system like $Pb_{1-x}Sn_xTe$, one must also take into account the effects of Hund's splitting. This effect can be built into our RG analysis by assuming the initial values of interactions in each of the scattering channels r to be such that $(h_r^{\sigma\overline{\sigma}} - h_r^{\sigma\sigma}) > 0$ (where $\sigma = \uparrow, \downarrow$). As seen in the previous section, in the presence of an external magnetization, p-wave superconductivity is destroyed (at the parquet level) even by a small value of Zeeman

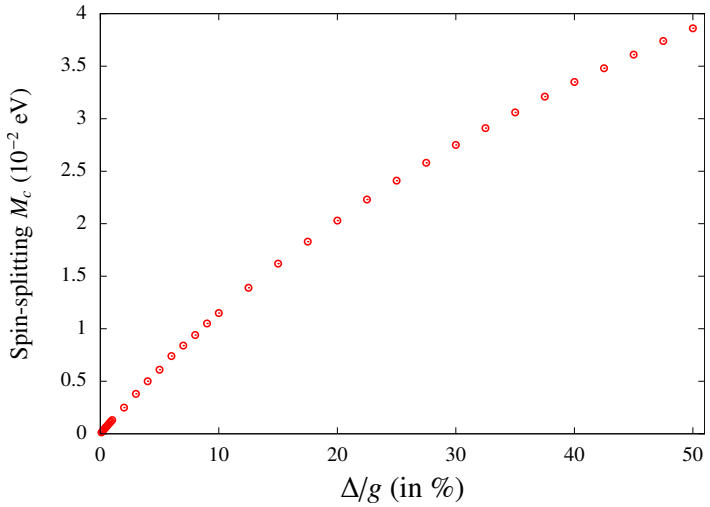

Fig. 3.9 The behavior of the critical value of the spin-splitting M_c (in eV) as a function of the Hund's splitting Δ as a percentage of the initial interaction g (i.e. $h_r^{\sigma\sigma} = g$ initially for $r = 1-4$ and $\sigma = \uparrow, \downarrow$), where $g = 0.1$ in this case. We find this behavior to be extremely insensitive to the initial value considered for the interactions.

splitting. However, this is no longer true if a finite Hund's splitting is introduced initially. For a Hund's splitting of $\triangle = h_r^{\sigma\overline{\sigma}} - h_r^{\sigma\sigma}$ (for each scattering channel r, where $\sigma = \uparrow, \downarrow$), p-wave superconductivity continues to be the leading instability at the parquet level up to a finite value of the Zeeman splitting M (which depends on the value of $\triangle$ being considered). Corresponding to each value of Δ, a critical value of the spin-splitting M_c is obtained such that for $M > M_c$, p-wave superconductivity is no longer possible. The variation of M_c as a function of the percentage Hund's splitting $\frac{\Delta}{g}$ (where g denotes the initial value chosen for $h_r^{\sigma\sigma}$ for $r = 1-4$ with $\sigma = \uparrow, \downarrow$) is shown in Fig. 3.9 for $g = 0.1$. The behavior of M_c as a function of $\frac{\Delta}{g}$ turns out to be remarkably insensitive to value of g, i.e. the initial interaction strength being considered (within the regime where perturbation theory is valid). To illustrate the nature of the most divergent couplings in the two limits, RG flows for $M < M_c$ and $M > M_c$ with a dimensionless initial repulsive interaction of 0.1 and a Hund's splitting of 5% ($\frac{|h_r^{\sigma\overline{\sigma}} - h_r^{\sigma\sigma}|}{|h_r^{\sigma\sigma}|} = 0.05$) introduced initially, where the critical value of the Zeeman splitting $M_c \approx 6.1$ meV, are shown in the Fig. 3 in Appendix-B. The corresponding behavior of $h_r^{\sigma\sigma'}(y)(y_c - y)$ as a function of $(y_c - y)$, which illustrates the order of the fixed point values $g_r^{\sigma\sigma'}$ for the different couplings in the above-mentioned two cases, is shown in the Fig. 4 in Appendix-B.

3.5 Summary

To summarize, we have studied competing electronic instabilities on the (001) surface of $Pb_{1-x}Sn_xTe$ using a parquet renormalization group analysis and established that chiral $p-$wave superconductivity is the dominant electronic instability in this system. The (001) surface features a double-Dirac cone structure, along with Type-II Van Hove singularities, which enhance the effective transition temperatures for competing Fermi-surface instabilities brought about by weak repulsive interactions. The chiral nature of the superconducting order arises not due to Fermi-surface deformations but due to the Berry phases associated with the surface states. The approximate Fermi-surface nesting on the (001) surface makes it crucial to study phase competition by taking into account competing instabilities in the particle-particle and particle-hole channels. We have further studied the effect of an external Zeeman spin-splitting field on the chiral $p-$wave order and find that in the presence of a finite Hund's splitting, there exists a critical value of the Zeeman field beyond which chiral $p-$wave order is no longer present. This implies that multiorbital effects in this system play an important role in stabilizing electronic order on the surface.

Chapter 4

Impurity-induced subgap states as an experimental signature of chiral $p-$wave order

Recent point-contact spectroscopy measurements [188, 189] have confirmed the existence of superconductivity on the (001) surface of $Pb_{1-x}Sn_xTe$. In these experiments, the superconductivity is indicated by a sharp fall in the resistance of the point contact below a characteristic temperature (3.7-6.5 K) along with the appearance of a spectral gap with coherence peak-like features, and zero-bias anomalies, which are a consequence of Andreev tunneling. However, the nature of the superconducting order remains to be ascertained. On the other hand, zero-bias anomalies appearing in scanning tunneling spectra, which have been discussed extensively as signatures of Majorana bound states [214, 167, 215], may also originate from other independent causes such as topologically trivial Andreev bound states [191, 190, 194, 192], band-structure effects [195] and stacking faults [196, 216]. While it has been shown that Majorana bound states can be realized at the end points of linear defects in a chiral $p-$wave superconductor [179], these may not exist for other types of surface defects, such as pointlike ones, or may be difficult to detect experimentally. An alternate strategy would be to go beyond the Majorana states and instead use impurity-induced Shiba-like states [204, 62] for probing the superconducting order. In this part of the thesis, we identify the parameter regimes of doping where a chiral $p-$wave superconducting order may be realized on the TCI surface, and where impurity-induced Shiba-like subgap states can be reliably used to establish the existence of the chiral $p-$wave order [217]. We also obtain exact analytical expressions for the bound-state spectra and wave functions, as a function of the parameters of the system, and our analysis sheds light upon the properties of the bound states that can be used to identify the nature of the superconducting order.

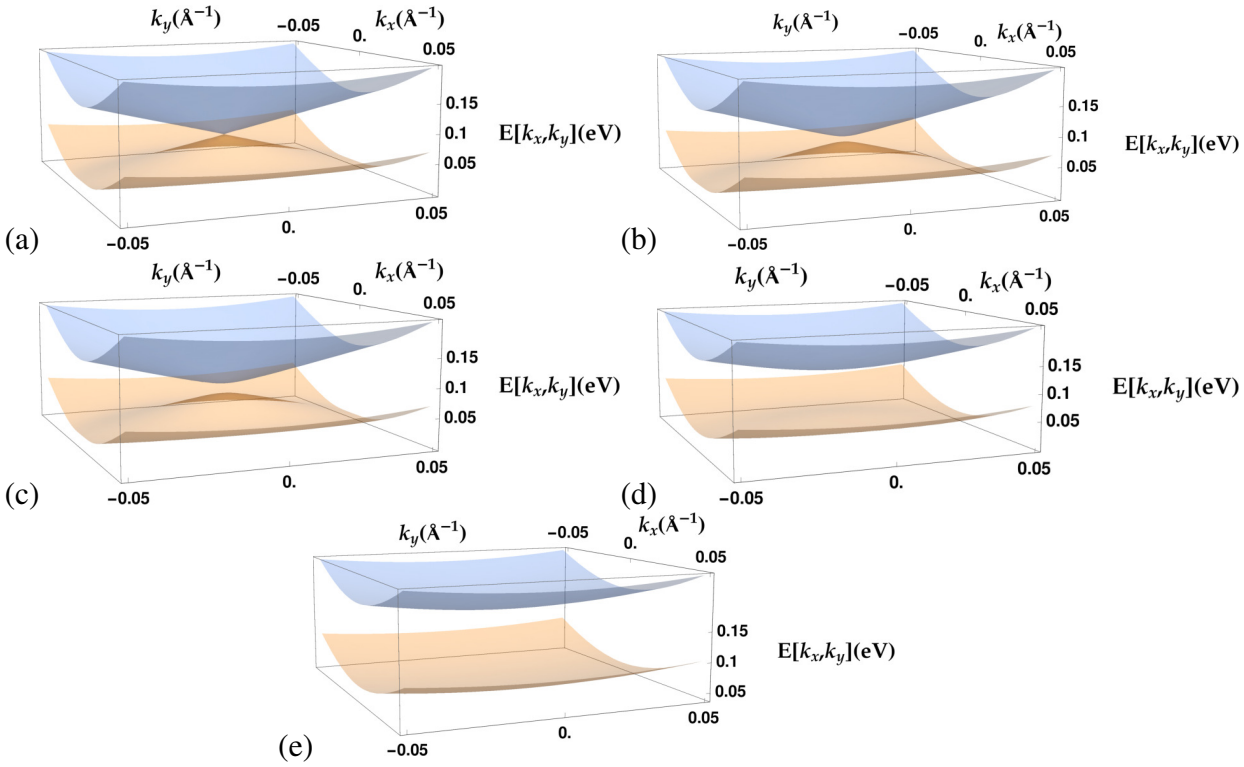

Fig. 4.1 The figure shows the bandstructure of the two upper surface bands in the vicinity of the $\overline{X}$ point as a function of (k_x, k_y) in the presence of a Zeeman spin-splitting of magnitude M, of different strengths; (a) $M = 0.0$, (b) $M = 0.005$, (c) $M = 0.01$, (d) $M = 0.05$, (e) $M = 0.1$ (in eV). Note that a gap is introduced at the $\overline{X}$ point as M is turned on, and with increasing values of M, this gap increases, and the curvature of the lower band gradually changes sign. A change in the curvature can also affect the nature of the impurity-induced bound states realized in the chiral $p-$wave superconducting state. In the paper, we work in the regime $M < m$, where the mass term $m = 0.07$ eV determines the value of the energy at the $\overline{X}$ point measured with respect to the pair of Dirac points.

4.1 Setting up the Nambu Hamiltonian

By examining the surface Hamiltonian in Eq. 3.1, it is evident that the two positive energy bands (and likewise the two negative energy ones) touch each other at the $\overline{X}$ point, due to time-reversal symmetry, with a massless Dirac-like dispersion in its vicinity. By introducing a small Zeeman spin-splitting field, one can break the time-reversal symmetry in this system and lift the degeneracy between the two bands at the $\overline{X}$ point. We introduce a Zeeman spin-splitting term Ms_z in the non-interacting surface Hamiltonian in Eq. 3.1, which lifts the degeneracy between the two bands at the $\overline{X}$ point, and results in the following dispersions for

the four surface bands

$$\varepsilon_{k,\pm} = \pm\sqrt{k_x^2 v_x^2 + k_y^2 v_y^2 + m^2 + \delta^2 + M^2 \pm 2\sqrt{M^2 m^2 + k_x^2 m^2 v_x^2 + k_y^2 (m^2+\delta^2) v_y^2}}. \quad (4.1)$$

For surface momenta (k_x, k_y) in the vicinity of the $\overline{X}$ point, we now have a massive Dirac-like dispersion, which can be approximately written as

$$\varepsilon_{k_x,k_y} = C - A(k_x^2 + k_y^2), \quad (4.2)$$

for the lower energy surface band, with $C = \sqrt{(M-m)^2 + \delta^2}$ and $A \sim 1/(MC)$, measured with respect to the pair of Dirac points lying on either side of the $\overline{X}$ point. Since we are interested in low values of doping, we will confine our attention to the regime corresponding to small momenta (k_x, k_y), where $M < m$. Please refer to Fig. 4.1 for a pictorial depiction of the surface bandstructure in the vicinity of the $\overline{X}$ point, in the presence of a Zeeman splitting term.

In our analysis of impurity-induced bound states in a chiral $p-$wave superconductor, we shall work with the following Bogoliubov-de Gennes (BdG) Hamiltonian:

$$H_0(k) = \begin{pmatrix} \varepsilon_{k_x,k_y} - \mu & \Delta(k_x - ik_y) \\ \Delta(k_x + ik_y) & -\varepsilon_{k_x,k_y} + \mu \end{pmatrix}, \quad (4.3)$$

where ε_{k_x,k_y} refers to the noninteracting dispersion in Eq. 4.2 and μ refers to the chemical potential. This Hamiltonian acts in the Nambu space $(c_k, c_{-k}^\dagger)$ where c_k are the effectively spinless fermions in the lower energy surface band, and $\Delta_k \equiv < c_k c_{-k} > = \Delta(k_x - ik_y)$ is the superconducting order parameter. In the absence of Δ, Eq. 4.3 would correspond to two copies of the Hamiltonian of a nonrelativistic particle whose energies are reckoned from an arbitrary value μ.

Substituting the expression for $\varepsilon_{k_x k_y}$ from Eq. 4.2 above, the spectrum corresponding to the Nambu Hamiltonian in Eq. 4.3 is given by $E = \pm\sqrt{(Ak^2 + \mu')^2 + \Delta^2 k^2}$, where $k^2 = k_x^2 + k_y^2$, and $\mu' = \mu - C$ is an effective chemical potential reckoned from the top of the band, corresponding to the energy value closest to the higher energy surface band. We introduce dimensionless quantities

$$\lambda = \frac{\Delta^2}{2A|\mu'|} \quad (4.4)$$

and

$$\varepsilon = \frac{E}{|\mu'|}, \quad (4.5)$$

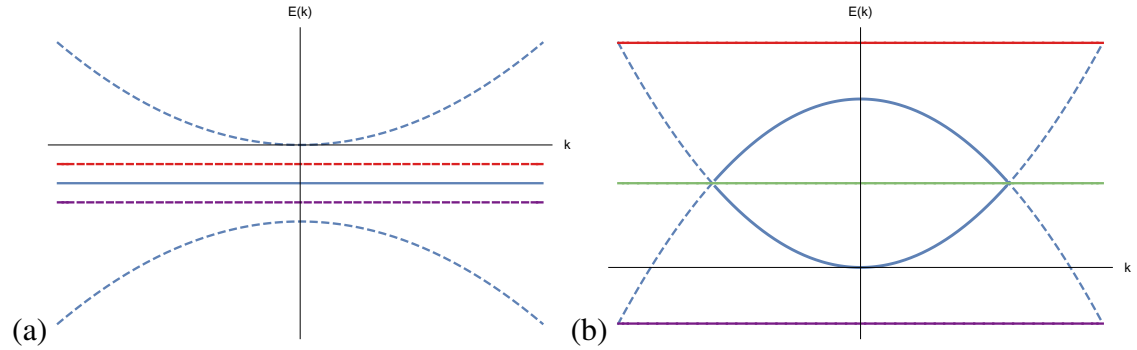

Fig. 4.2 The figure shows a schematic illustration of the Nambu bands when (a) $\mu < 0$, and the chemical potential lies in the gap (b) $\mu > 0$ and the chemical potential intersects the bands, in the absence of the chiral $p-$wave order parameter Δ. The bound state energies denoted by the red and purple lines lie within the gap in (a) and intersect the bands in (b). The chemical potential μ lies in the centre and is denoted by the blue line in (a) and the green line in (b). The filled and empty part of the bands are represented by solid and dashed lines respectively. Clearly, in (a) both the bands as well as the impurity states are empty.

which appear frequently in our analysis. For non-zero values of μ, the spectrum of the BdG Hamiltonian is gapped if Δ is finite. We look specifically for bound states which lie within the gap.

4.2 Impurity-induced subgap bound states

In order to understand the principle behind the classification of impurity-induced states in different parameter regimes for our system, we first consider the simpler problem of impurity-induced states in doped semiconductors, and the difference in the nature of the impurity bound states in the presence and absence of superconductivity, as well as the role played by the position of the chemical potential in determining this difference.

4.2.1 Impurity states in doped semiconductors

It is well-known that in one dimension, a bound state always exists for a nonrelativistic particle in the presence of an attractive Delta-function potential. Consider a single impurity in a semiconductor, and writing down the Schrodinger equation in momentum space, we have

$$(\varepsilon_k - \mu)\psi_k + \int dk' V_{k,k'} \psi_{k'} = E\psi_k \tag{4.6}$$

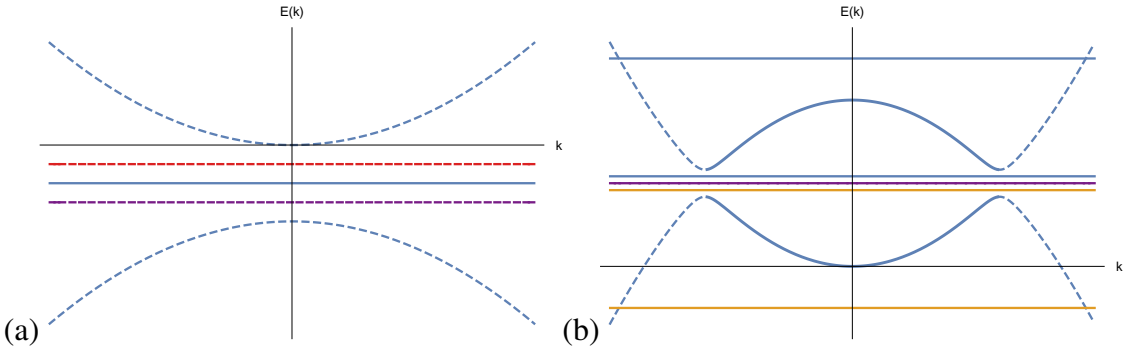

Fig. 4.3 The figure shows a schematic illustration of the Nambu bands when (a) $\mu < 0$, and the chemical potential lies in the gap (b) $\mu > 0$ and the chemical potential intersects the bands, in the presence of the chiral $p-$wave order parameter Δ. Clearly, an additional band gap opens in (b) due to the superconducting order. The impurity levels denoted by the red and purple lines in (a) lie within the gap, while in (b), a pair of impurity levels denoted by blue and yellow lines lie within the smaller gap while another pair intersects the two bands. The chemical potential μ lies in the centre and is denoted by the blue line in (a) and the purple line in (b). The filled and empty part of the bands are represented by solid and dashed lines respectively. In (a), both the bands as well as the impurity states are empty.

where $V_{k,k'} = V_0$ and μ denotes the chemical potential. Using

$$\psi_k = \frac{-V_0 \int dk' \psi_{k'}}{(\varepsilon_k - \mu - E)}$$

and integrating both sides over the momentum k, we obtain the following condition on the defect potential strength V_0 for realizing impurity-induced bound states

$$V_0 = \frac{-1}{\int \frac{dk}{(\varepsilon_k - \mu - E)}}$$

which always gives rise to a solution, provided the integrand does not have any real poles. When such impurity bound states are present, they appear at an energy value proportional to $\sqrt{V_0}$ below the bottom of the conduction band and move further downwards as V_0 increases. If ε_k is the valence band of a semiconductor, then the V_0 must be positive, and the bound states appear above the top of the valence band. The existence of the impurity band is independent of the chemical potential μ, but the chemical potential determines whether the impurity band is occupied or not.

Now, the same problem can be reexpressed in the Nambu representation by introducing another copy of the problem which is related to the first one by a particle-hole transformation. In the Nambu representation, the impurity bound states appear exactly as discussed above,

except that since there are now two copies, for each positive impurity level, there is a corresponding negative one with the same magnitude. Consider the example of an impurity bound state arising from donor dopants in a semiconductor, and $\varepsilon_k > 0$ corresponds to the conduction band. The chemical potential is the reference energy from which all energies are measured, and in this case, the negative value of μ implies that the chemical potential does not intersect the bands, and both the bands are empty. This is illustrated in Fig. 4.2 (a) above. On the other hand, when $\mu > 0$, the bands as well as the impurity levels cross the Fermi level, and become occupied, resulting in a new situation depicted in Fig. 4.2 (b). This is merely an artefact of the chemical potential changing sign and the levels that have crossed are those whose nature has changed from being empty to being occupied.

The situation changes dramatically in the presence of a chiral $p-$wave superconducting order. If the chemical potential $\mu < 0$, the impurity levels remain empty but the bands shift in magnitude, as shown in Fig. 4.3 (a). Here, we continue to obtain subgap states and the impurity levels are indistinguishable from those in semiconductors. However, when $\mu > 0$, the presence of superconductivity introduces a gap at the points where the two dispersing bands intersected, as shown in the Fig. 4.3 (b). In this regime, the impurity levels which were formerly present only near the extrema of the upper and lower Nambu bands abruptly collapse to take values within the gap, and therefore, we now obtain subgap states. Thus, in the presence of a chiral $p-$wave order, if $\mu < 0$, one continues to obtain subgap states which are indistinguishable from impurity states in semiconductors, while if $\mu > 0$, new subgap states appear due to the superconducting order in the system.

In an analogous manner, we identify different parameter regimes of doping for the (001) surface of $Pb_{1-x}Sn_xTe$, classified as *the normal gap* and the *inverted gap* regimes, only in the latter of which one can realize subgap bound states depending crucially upon the existence of the chiral $p-$wave order.

4.2.2 Conditions for obtaining subgap bound states

We derive the general condition for realizing subgap bound states localized in one or more directions, associated with point or linear defects on the surface of the TCI, modeling such defects by a multidimensional Dirac delta-function $V(x_i) = V_0 \prod_i \delta(x_i)$, where i refers to the dimension, and V_0 represents the strength of the defect potential. The delta-function approximation for the potential defects is justified, provided that the defect potential is sufficiently smooth on the scale of the lattice constant (to avoid scattering processes between the $\overline{X}_1$ and $\overline{X}_2$ points) but nevertheless, short-ranged compared to the wavelength of the electrons.

The Schrödinger equation in momentum space, in the presence of the defect potential is given by

$$H_0(k)\psi_k + \int (d^d k') V_{k,k'} \psi_{k'} = E\psi_k, \tag{4.7}$$

where $H_0(k)$ is defined in Eq. 4.3 above, E refers to the value of the bound state energy, and $V_{k,k'} = V_0\sigma_z$ for the case of a point defect, and $2\pi V_0 \delta(k_y - k_y')\sigma_z$ for a linear defect along the $y-$direction. In the latter case, the integration over k_y' gets rid of the Delta function, leading to an equation which is diagonal in k_y but mixes the k_x components.

Inverting Eq. 4.7, we have

$$\psi_k = -[H_0(k) - EI]^{-1} V_0 \sigma_z \int (d^d k') \psi_{k'}, \tag{4.8}$$

where it is understood in Eq. 4.8 above and also in the analysis that follows that the integration runs only over k_x for a linear defect along the $y-$direction. Next, we integrate both sides over k, cancel the common term $\int (d^d k)\psi_k$ on both sides and arrive at the following condition:

$$\mathrm{Det}\{-\int (d^d k)[H_0(k) - EI]^{-1} V_0 \sigma_z - I\} = 0, \tag{4.9}$$

for the bound state. Here the integration over each component of k ranges from $-\infty$ to ∞. Note that when $\int (d^d k)\psi_k = 0$, the wavefunction vanishes at the origin, and the above condition is no longer applicable, since we cannot cancel the common terms. This is, for example, true for topologically non-trivial zero-energy Majorana bound states in linear defects, for which the real-space wavefunction acquires its peak values at the physical ends of the defect and decays into the interior. When the defect being considered is infinitely long in one of the directions, the ends not being a part of the system, one cannot mathematically realize Majorana bound states within this approach. Here we have explicitly excluded such states from consideration.

Using the expression for $H_0(k)$ in Eq. 4.3, the condition in Eq. 4.9 translates to

$$\mathrm{Det}\begin{pmatrix} -V_0 I_1(0,0,E) - 1 & V_0 I_3(0,0,E) \\ -V_0 I_4(0,0,E) & -V_0 I_2(0,0,E) - 1 \end{pmatrix} = 0, \tag{4.10}$$

where we define

$$I_{1,2}(x,y,E) = \int_{-\infty}^{\infty} (dk_x)(dk_y) \exp[ik_x x] \exp[ik_y y] \frac{\varepsilon_{k_x,k_y} - \mu \pm E}{(\varepsilon_{k_x,k_y} - \mu)^2 - E^2 + \Delta^2(k_x^2 + k_y^2)}, \tag{4.11}$$

and

$$I_{3,4}(x,y,E) = \int_{-\infty}^{\infty} (dk_x)(dk_y) \exp[ik_x x] \exp[ik_y y] \frac{\Delta(k_x \mp ik_y)}{(\varepsilon_{k_x,k_y} - \mu)^2 - E^2 + \Delta^2(k_x^2 + k_y^2)}. \quad (4.12)$$

Let us consider first the case of point defects. From Eq. 4.10, we obtain the following condition for the strength of the defect potential V_0 that gives a bound state at energy E:

$$(V_0 I_1(0,0,E) + 1)(V_0 I_2(0,0,E) + 1) = 0. \quad (4.13)$$

From Eq. 4.13, it is evident that for a given value of V_0, we have a pair of bound states with energies $\pm E$, which is a reflection of particle-hole symmetry of the BdG Hamiltonian. Conversely, for every value of the bound state energy there exist two possible values for the strength of the defect potential, V_0, which do not in general have the same magnitude, for which one may realize such a state.

For a line defect of infinite length along, say, the $y-$direction, the defect potential may be written as $V(x) = V_0 \delta(x)$, such that the translational symmetry is broken only along the $x-$direction. In this case, we obtain, from Eq. 4.10, the following condition for realizing a subgap bound state with an energy E, where k_y is conserved and takes real values.

$$(V_0 I_1(0,0,E) + 1)(V_0 I_2(0,0,E) + 1) + V_0^2 I_3(0,0,E) I_4(0,0,E) = 0. \quad (4.14)$$

The relation between V_0 and E is

$$V_0(E) = \frac{-(I_1 + I_2) \pm \sqrt{(I_1 - I_2)^2 - 4 I_3 I_4}}{2(I_1 I_2 + I_3 I_4)}. \quad (4.15)$$

Since V_0 is real, the discriminant must be positive, resulting in a condition which relates the allowed values of the bound state energy to the quantum number k_y i.e. $\min(E_g^2, (\mu')^2) \geq E^2 \geq \Delta^2 k_y^2$. The lowest energy bound states clearly correspond to the case where $k_y = 0$. This leads to the conditions $1 + I_1 V_0 = 0$, or $1 + I_2 V_0 = 0$.

From Eq. 4.8, we can also obtain expressions for the bound state wavefunctions. Taking an inverse Fourier transform on both sides, we obtain the following expression for the wavefunction in real space:

$$\psi(x,y) = \begin{pmatrix} a(x,y) \\ b(x,y) \end{pmatrix} = (-V_0) \begin{pmatrix} I_1(x,y,E) a_0 - I_3(x,y,E) b_0 \\ I_2(x,y,E) b_0 + I_4(x,y,E) a_0 \end{pmatrix}, \quad (4.16)$$

where $\psi_0 = \begin{pmatrix} a_0 \\ b_0 \end{pmatrix}$ is the real-space wavefunction at the origin, i.e. $\psi(0,0)$, and $I_{1,2}(x,y,E)$ and $I_{3,4}(x,y,E)$ are as defined in Eqs. 4.11 and 4.12. The normalization condition is

$$\int dx \int dy (|a(x,y)|^2 + |b(x,y)|^2) = 1. \tag{4.17}$$

For the case of a point defect, we find that, for any non-zero value of the bound state energy E, putting $x = y = 0$ on both sides of Eq. 4.16 above results in the elimination of one of the components a_0 or b_0 when the condition in Eq. 4.13 is satisfied. For $E = 0$, however, it simply gives rise to a consistency condition without yielding any new information about the components at the origin, and the only constraint on the constants a_0 and b_0 is then the normalization condition in Eq. 4.17. This is a manifestation of an internal SU(2) rotational symmetry (in particle-hole space), which makes the zero energy state centered at the origin useful as a possible quantum qubit. A similar condition is also obtained for a linear defect, but in the specific case where $k_y = 0$. Since there are arbitrarily close bound states parametrized by nonzero k_y, the zero energy state is not useful as a qubit for the case of linear defects.

4.3 Bound state spectra and wavefunctions

In obtaining the analytical expressions for the bound state spectra and wavefunctions, we shall distinguish between the situations where the chemical potential lies within the conventional or *normal* band gap between the pair of surface bands, and those where it intersects the lower surface conduction band, giving rise to an *inverted* band gap at small momenta. We shall find that the subgap states that arise in the *inverted band gap* situation crucially depend on the existence of the chiral $p-$wave order. On the other hand, in the *normal band gap* situation, the impurity bound states are not qualitatively affected in the limit where the chiral $p-$wave order is absent. A schematic of the band structure near the $\overline{X}$ point on the (001) surface, together with various representative positions for the chemical potential is shown in Fig. 4.4. If the gap is sufficiently large and the Fermi level does not intersect the upper band, then (interband) $s-$wave superconductivity, which occurs in case (a) of Fig. 4.4, is precluded. For the case (b) in Fig. 4.4 where the chemical potential does not intersect the lower surface conduction band, the band gap is conventional, as in, say, a semiconductor, and we call it *normal*. For the case (c) in Fig. 4.4, where it intersects this band, an additional band gap opens up at the points of intersection (not depicted in Fig. 4.4), due to the presence of the chiral $p-$wave superconducting order. This corresponds to an *inverted band gap*. In what

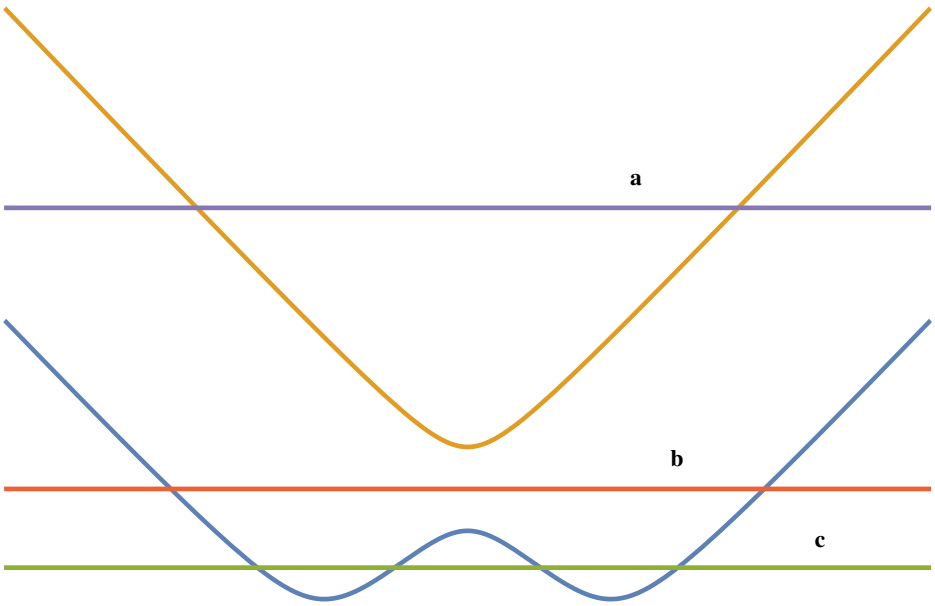

Fig. 4.4 The figure shows a schematic illustration of the bandstructure in the vicinity of the $\overline{X}$ point, and three different doping regimes that can either result in qualitatively different electronic instabilities on the (001) surface of $Pb_{1-x}Sn_xTe$ (i.e. either conventional $s-$wave or chiral $p-$wave order), or lead to a difference in the nature of impurity-induced bound states realized in a chiral $p-$wave superconducting state. In (a), the Fermi level intersects two of the surface bands, which are time-reversed counterparts. In this case, interband pairing of electrons gives rise to $s-$wave superconductivity, and no Shiba-like states exist for potential defects on the surface. In (b) and (c), the pairing of the surface electrons is of the chiral $p-$wave type. We show in the paper that only the latter case, (c), when the Fermi level intersects the lower surface conduction band, Shiba-like subgap states can be unambiguously attributed to the presence of topological superconductivity.

follows, we will be working with the valence band, as that is the physical situation prevailing in our system.

4.3.1 Point defects

Let us first consider the case of a point defect. In plane polar coordinates, Eq. 4.13, relating the impurity strength to the bound state energy E, takes the form

$$\frac{1}{V_0} = \frac{1}{4\pi}\int_0^{\Lambda^2} d\upsilon \frac{(A\upsilon+\mu') \mp E}{(A\upsilon+\mu')^2 - E^2 + \Delta^2\upsilon}, \tag{4.18}$$

where $\upsilon = k^2$ and $\mu' \equiv \mu - C$, and Λ is the large momentum cutoff, physically corresponding to the inverse of the width of the potential well, which is approximated to be a Delta-function potential in our treatment. We now examine Eq. 4.18 respectively in the *normal* and *inverted* band gap regimes.

Conditions for bound states in different parameter regimes

(a) Normal band gap: $\mu' > 0$

When the chemical potential $\mu > C$ (or $\mu' > 0$), the condition for subgap bound states in Eq. 4.18 above evaluates to

$$\frac{1}{V_0} \approx \frac{1}{2A\sqrt{(\lambda+1)^2-(1-\varepsilon^2)}}\left[(\lambda\pm\varepsilon)\ln\left|\frac{\lambda+1-\sqrt{(\lambda+1)^2-(1-\varepsilon^2)}}{\lambda+1+\sqrt{(\lambda+1)^2-(1-\varepsilon^2)}}\right|\right.$$

$$\left. +\sqrt{(\lambda+1)^2-(1-\varepsilon^2)}\left(\ln\left|\frac{A^2\Lambda^4}{|\mu'|^2(1-\varepsilon^2)}\right|\right)\right]. \tag{4.19}$$

For any value of the bound-state energy $|E| < \mu'$, we find that $(\lambda\pm\varepsilon) < \sqrt{(\lambda+1)^2-(1-\varepsilon^2)}$, implying that V_0 is always a positive quantity. Physically, this corresponds to impurity (hole) states near the valence band of a semiconductor, and in this regime, one always obtains subgap states, even when Δ is turned off. The impurity levels here lie in the manner shown in Fig. 4.3 (a).

(b) Inverted band gap: $\mu' < 0$

Here, the chemical potential $\mu < C$, or $\mu' < 0$, and this corresponds to the *inverted band gap* situation, which corresponds to the expression in Eq. 4.19 above, with $\lambda \to -\lambda$. In this case,

a gap opens either at $k = 0$ or at the points of intersection of the two Nambu bands (see Fig. 4.3 (b)). If, in this regime, Δ is turned off, this gap will close and the impurity levels will be pushed away to the positions originally predicted for impurity states in a semiconductor (see Fig. 4.2 (b)).

Exponentially decaying bound state wavefunctions for point defects

Let us now calculate the expressions for the bound state wavefunctions for the case of a point defect. From Eq. 4.16, it can be seen that the spatial dependence of the bound-state wavefunctions is determined by the integrals $I_{1,2}(x,y,E)$ and $I_{3,4}(x,y,E)$, defined in Eqs. 4.11 and 4.12 respectively. In plane polar coordinates, these equations assume the form

$$I_1(r) = -\frac{1}{(2\pi)^2}\int dk d\phi\, k \exp[ikr\cos[\theta-\phi]]\frac{(Ak^2+\mu')\mp E}{(Ak^2+\mu')^2-E^2+\Delta^2k^2} \tag{4.20}$$

and

$$I_2(r,\theta) = \frac{1}{(2\pi)^2}\exp[i\theta]\int dk d\phi\, k \exp[ikr\cos[\phi]]\exp[i\phi]\frac{\Delta k}{(Ak^2+\mu')^2-E^2+\Delta^2k^2} \tag{4.21}$$

where $\mu' \equiv \mu - C$, $k = \sqrt{k_x^2+k_y^2}$, and $\tan[\phi] = y/x$. We illustrate the specific case of $E = 0$ where simple analytical expressions for the wavefunctions can be obtained in terms of elementary functions. Qualitatively similar results are expected for other bound-state energies with $E \neq 0$. We once again consider regimes with a *normal* and an *inverted* band gap.

(a) Normal band gap: $\mu' > 0$

Using the well-known result $\int d\phi \exp[ikr\cos[\theta-\phi] = 2\pi J_0(kr)$, the expression of $I_1(r)$ from Eq. 4.20 is as follows:

$$\begin{aligned} I_1(r) &= \frac{1}{4\pi}\int dk k J_0(kr)\frac{2}{A(\alpha+\beta)}\left(\frac{\alpha}{k^2+\alpha^2}+\frac{\beta}{k^2+\beta^2}\right) \\ &= -\frac{1}{2\pi A(\alpha+\beta)}\left(\alpha K_0(\alpha r)+\beta K_0(\beta r)\right), \end{aligned} \tag{4.22}$$

where $\alpha,\beta = \sqrt{\mu'/A}((\sqrt{(\lambda+2}\pm\sqrt{\lambda})/\sqrt{2})$.

Thus, we find that $I_1(r)$ is an exponentially decaying function of at large distances r from the position of the defect. Note that when $\Delta = 0$, i.e. $\lambda = 0$, α and β are real, giving rise to exponentially decaying states.

Similarly, using the result $\int d\phi \exp\{ikr\cos[\theta-\phi]\}\exp[i\phi] = i\exp[i\theta]2\pi J_1(kr)$, we may simplify the expression for I_2 given in Eq. 4.21 as

$$\begin{aligned} I_2(r,\theta) &= \frac{-i\exp[i\theta]}{2\pi A(\alpha+\beta)}\int \frac{dx}{r} J_1(x)\left(\frac{x^2}{x^2+\alpha^2 r^2} - \frac{x^2}{x^2+\beta^2 r^2}\right) \\ &= \frac{-i\exp[i\theta]}{2\pi A(\alpha+\beta)}\frac{1}{r}\left(K_1(\alpha r) - K_1(\beta r)\right), \end{aligned} \tag{4.23}$$

where $kr \equiv x$, $\alpha,\beta = \sqrt{\mu'/A}((\sqrt{\lambda+2} \pm \sqrt{\lambda})/\sqrt{2})$, and in the second line we have used the relation [218]

$$\int_0^\infty dx \frac{xJ_0(ax)}{x^2+\alpha^2 r^2} = K_0(a\alpha r), \tag{4.24}$$

differentiated both sides with respect to the parameter a and taken the limit $a \to 1$, to obtain Eq. 4.23 above. We therefore find that the function $I_2(r,\theta)$ decays exponentially at large distances.

(b) Inverted band gap: $\mu' < 0$

Here, we consider a situation where $\mu < C$, or $\mu' < 0$, and repeat the analysis of the previous section by replacing μ' by $-|\mu'|$ in Eqs. 4.20 and 4.21.

For $\lambda \geq 2$, we then have,

$$\begin{aligned} I_1(r) &= \frac{1}{2\pi}\int dk\, kJ_0(kr)\frac{1}{A(\alpha-\beta)}\left(\frac{2\alpha}{k^2+\alpha^2} - \frac{2\beta}{k^2+\beta^2}\right) \\ &= \frac{1}{2\pi A(\beta-\alpha)}\left(\alpha K_0(\alpha r) - \beta K_0(\beta r)\right), \end{aligned}$$

where now $\alpha,\beta = \sqrt{\mu'/A}((\sqrt{\lambda} \pm \sqrt{\lambda-2})/\sqrt{2})$. Similarly, from Eq. 4.21, we write the expression for $I_2(r,\theta)$ as

$$\begin{aligned} I_2(r,\theta) &= \frac{i}{2\pi}\exp[i\theta]\int dk J_1(kr)\frac{1}{(A)}\frac{1}{(\beta-\alpha))}\left(\frac{x^2}{x^2+\alpha^2 r^2} - \frac{x^2}{x^2+\beta^2 r^2}\right) \\ &= \frac{i\exp[i\theta]}{2\pi A(\beta-\alpha)}\frac{1}{r}\left(K_1(\alpha r) - K_1(\beta r)\right) \end{aligned}$$

where $\alpha,\beta = \sqrt{\mu'/A}((\sqrt{\lambda} \pm \sqrt{\lambda-2})/\sqrt{2})$, following steps similar to the previous case, where $\mu' > 0$. The results obtained are identical for $\lambda < 2$, but with $\alpha,\beta = \sqrt{|\mu'|/A}((\sqrt{\lambda} \mp i(\sqrt{2-\lambda})/\sqrt{2})$. Please refer to Appendix-C for a detailed derivation of the asymptotic forms of the bound state wavefunctions.

In contrast to a chiral superconductor, a nodal superconductor gives a qualitatively different wavefunction for the impurity bound state. For instance, when the superconducting order parameter $\Delta_k = \Delta k \cos[\phi]$, we have

$$I_2(r,\theta) = \frac{\cos[\theta]}{(2\pi)} \int dk\, k \frac{\Delta k}{(Ak^2+\mu')^2 + \Delta^2 k^2} i J_1(kr).$$

Similarly, for $\Delta_k = \Delta k \sin[\phi]$,

$$I_2(r,\theta) = \frac{\sin[\theta]}{(2\pi)} \int dk\, k \frac{\Delta k}{(Ak^2+\mu')^2 + \Delta^2 k^2} i J_1(kr).$$

Thus, unlike a chiral $p-$wave superconductor, the above types of superconducting order feature nodal lines in the bound-state wavefunction, at large distances from the position of the defect. One could use STM imaging of the bound-state wavefunctions as a means to distinguish between nodal and chiral $p-$wave order on the surface.

4.3.2 Line defects

Here we study the nature of bound states for long linear defects. In this case, we write the defect potential as $V(x,y) = V_0\delta(x\cos[\alpha] + y\sin[\alpha])$, and consider the special case of $\alpha = 0$, i.e. $V(x) = V_0\delta(x)$. Once again, we study the two regimes with a *normal* and an *inverted* band gap, respectively.

(a) Normal band gap: $\mu' > 0$

Following Eq. 4.14, the relation between V_0 and the bound state energy E (for $k_y = 0$) is given by

$$\frac{1}{V_0} = \frac{1}{(2\pi)} \int_0^\infty \frac{dy}{2\sqrt{y}} \frac{(-Ay - \mu' \pm E)}{A^2(y+a)(y+b)}, \tag{4.25}$$

where $\mu' \equiv \mu - C$, $y = k_x^2$ and $a,b = (\mu'/A)((\lambda+1 \mp \sqrt{((\lambda+1)^2 - (1-\varepsilon^2)})$. Evaluating the integral in Eq. 4.25, we arrive at

$$V_{0,\pm} = \frac{4A(\sqrt{a}+\sqrt{b})}{(1+\sqrt{(1\mp\varepsilon)/(1\pm\varepsilon)})}, \tag{4.26}$$

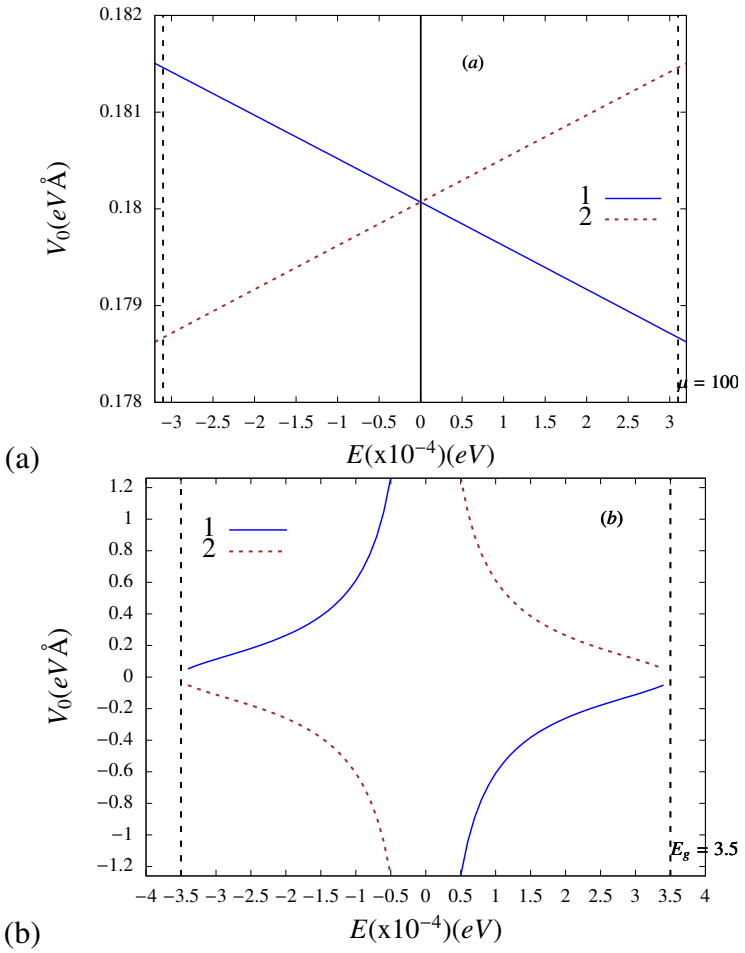

Fig. 4.5 The figure shows the variation in the strength of the defect potential V_0 required to give a subgap bound state, as a function of the magnitude of the bound state energy E for a line defect. The cases considered are: (a) $\mu' > 0$ for a *normal* band gap (b) $\mu' < 0$ for an *inverted* band gap. The parameters chosen are $A = 4.0$ eVÅ, $\mu' = 20$ meV and $\Delta = 5$ meVÅ. We find the behavior to be qualitatively different in the two cases. In the latter case, $V_0 \to \infty$ as $E \to 0$ and the defect potential strength V_0 can change sign, which opens up the possibility of realizing subgap bound states for both potential wells and barriers of various sizes. Here, *1* and *2,* denoted by the solid and dashed curves respectively, refer to the two solutions obtained for the strength of the potential V_0. The dashed line refers to the value of the energy gap, which is given by $2|\mu'|$ for the topologically trivial regime in (a) and $2E_g$ for the topologically nontrivial regime in (b).

with $\sqrt{ab} = |\mu'|\sqrt{1-\varepsilon^2}/A$. The variation of V_0 as a function of the bound state energy E is shown in Fig. 4.5. Here we find a trivial crossing of the energy level with the chemical potential as V_0 is tuned, which does not depend on the presence of superconductivity. We emphasize here that the crossing that we observe is an artefact of the Nambu representation, and would appear even in the absence of superconductivity.

The subgap bound states in this case form a part of a continuum of states parametrized by different values of k_y. The corresponding expression obtained by solving Eq. 4.14 for a finite, real value of k_y is given by

$$V_{0,\pm} = \frac{2A(\sqrt{a}+\sqrt{b})\sqrt{1\pm\varepsilon_e}\left(\sqrt{1\mp\varepsilon_e}+\sqrt{1\pm\varepsilon_e}\right)}{\left(\sqrt{1-\varepsilon_e^2}+1\right)},$$

with $a,b = (\mu_e/A)(\lambda_e+1\mp\sqrt{(\lambda_e+1)^2-(1-\varepsilon_e^2)})$, $\mu_e = \mu'+Ak_y^2$, $E_e^2 = E^2-\Delta^2k_y^2$ and $\lambda_e = \Delta^2/(2A|\mu_e|)$. Clearly, V_0 is always positive in this case, corresponding to hole-like states near the valence band.

(b) Inverted band gap: $\mu' < 0$

When the chemical potential intersects the lower surface conduction band, we have $\mu' < 0$. Evaluating the resulting integral from Eq. 4.14, we obtain the relation

$$V_{0,\pm} = \frac{4A(\sqrt{a}+\sqrt{b})}{(1-\sqrt{(1\pm\varepsilon)/(1\mp\varepsilon)})}, \tag{4.27}$$

where $a,b = (|\mu'|/A)(\lambda-1\mp\sqrt{(\lambda-1)^2-(1-\varepsilon^2)})$. Clearly, in this case, the amplitude of the defect potential may change sign depending upon the value of the bound state energy E under consideration, and in general, subgap bound states can be realized for both potential wells and barriers, corresponding to particle-like and hole-like states, as is also evident from Fig. 4.5. The defect potential strength corresponding to the bound state solutions move further away as we approach $\varepsilon \to 0$, as illustrated in Fig. 4.5 (b).

Similarly, for a finite, real value of k_y, we obtain the relation

$$V_{0,\pm} = \frac{2A(\sqrt{a}+\sqrt{b})\sqrt{1\mp\varepsilon_e}\left(\sqrt{1\pm\varepsilon_e}-\sqrt{1\mp\varepsilon_e}\right)}{\left(\sqrt{1-\varepsilon_e^2}-1\right)},$$

where $\mu_e = \mu'-Ak_y^2$, $E_e^2 = E^2-\Delta^2k_y^2$, and $a,b = (|\mu_e|/A)(\lambda_e-1\mp\sqrt{(\lambda_e-1)^2-(1-\varepsilon_e^2)})$. Note that the above expression is only applicable in the regime where $\varepsilon_e^2 < 1$.

On the other hand, for $\varepsilon_e^2 > 1$, which can only be satisfied for $\mu' < 0$, we have the alternate expression

$$V_{0,\pm} = \frac{4A^2\sqrt{b}\,(b+a)\,(Ab+|\mu_e|\,(1\pm\varepsilon_e))}{(A^2b^2+2A|\mu_e|b+\mu_e^2\,(1-\varepsilon_e^2))}, \tag{4.28}$$

where $a,b = (\mu_e/A)(\sqrt{(\lambda_e-1)^2-(1-\varepsilon_e^2)} \mp (\lambda_e-1))$. The RHS in Eq. 4.28 may change sign for bound state energies satisfying the condition $|\varepsilon_e| > \lambda_e$.

4.4 Summary

In summary, we have examined the parameter regimes where a chiral $p-$wave superconducting order can exist on the (001) surface of $Pb_{1-x}Sn_xTe$, depending upon the position of the chemical potential and the strength of the Zeeman splitting. Within the chiral $p-$wave regime, we further identified two situations, corresponding to the *normal* and the *inverted band gap* and showed that although Shiba-like subgap states can exist in both these regimes, only in the latter case, such states can be attributed to the presence of a chiral $p-$wave superconducting order. As a possible application of our results, we show that for the case of point defects, the wavefunctions corresponding to the zero-energy bound states have an internal SU(2) rotational symmetry, which makes them useful as possible quantum qubits. We have obtained exact analytical expressions for the bound state spectra and wavefunctions in different regimes, and used the properties of these states to identify the chiral $p-$wave nature of the superconducting order.

HIGH FIELD MAGNETORESPONSE OF A KITAEV MATERIAL: SIGNATURES OF FIELD-INDUCED SPIN LIQUID PHYSICS

Chapter 5

Kitaev materials: spin-orbit physics in correlated electron systems

In recent times, the emergence of novel quantum states of matter in correlated electron systems with strong spin–orbit coupling (SOC) has been a subject of great interest, both theoretically and experimentally [21, 22]. The combination of electronic correlations and SOC engenders many new and exotic quantum phases of matter, such as topological insulators and superconductors [25, 105, 145], unconventional magnetism [219] and spin liquids [220–225]. While 3d transition metal oxide systems form a traditional playground for strong correlation effects [35, 226], it has recently been realized that 4d and 5d transition metal compounds provide an excellent platform for realizing the cooperative effects of electron correlations and strong spin-orbit coupling [21]. The latter class of materials are expected to show metallic behavior owing to their relatively larger electronic bandwidths, but are instead found to host exotic insulating states, now recognized to be narrow-gap Mott states aided by strong spin-orbit coupling [227]. Such systems are governed by a combination of electronic correlations, spin-orbit entanglement, and crystal-field effects, and give rise to peculiar correlated ground states and excitations. They exhibit magnetic states with unusually low ordered moments, which are best described as effective pseudospin $\widetilde{j} = \frac{1}{2}$ entities [18, 227, 228], due to the strong spin-orbit coupling. In particular, these have been proposed to realize the physics of the Kitaev spin model [77] with bond-dependent spin-spin interactions on a 2D honeycomb lattice, which harbors gapped and gapless spin-liquid states with emergent Majorana fermionic excitations. The search for a quantum spin liquid (QSL) [5, 6], a collective quantum state with long-range entanglement and fractionalized excitations, has been a long-standing quest in modern Condensed Matter Physics, and is a part of the greater initiative towards understanding the existence and nature of phases beyond Landau's theory of spontaneous symmetry breaking. The realization of spin liquid states in actual

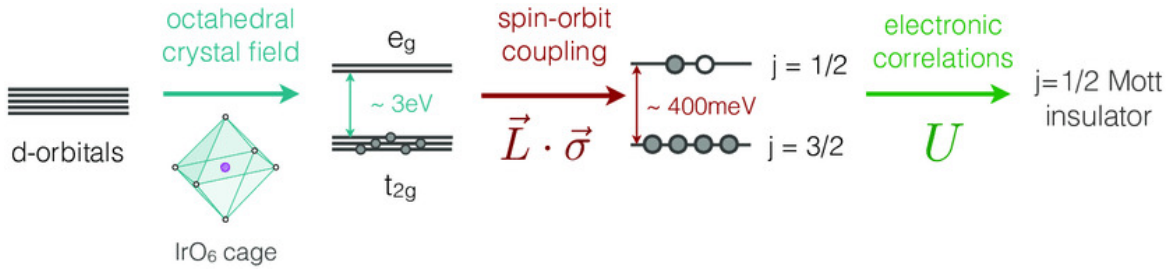

Fig. 5.1 The figure depicts the formation of spin-orbit entangled $\widetilde{j} = 1/2$ moments for ions in a d^5 electronic configuration such as for the iridium ion Ir^{4+}. The degeneracy between the 5d orbitals is lifted by the crystal field splitting due to the octahedral environment, and the t_{2g} and e_g sets of orbitals have different energies. The large SOC acts within the t_{2g} manifold, which can be mapped to effective $\widetilde{l} = 1$ operators, giving rise to $\widetilde{j} = \frac{1}{2}$ and $\widetilde{j} = \frac{3}{2}$ states. A finite Mott-like gap is then introduced in the $\widetilde{j} = \frac{1}{2}$ bands. (Figure has been reproduced from Ref. [46])

materials represents a significant experimental and theoretical challenge, and there has been considerable progress in this direction owing to the emergence of these so-called 'Kitaev materials' [46]. In particular, the honeycomb iridates A_2IrO_3 (A=Na,Li) [68] and $\alpha-RuCl_3$ [72] have attracted much theoretical and experimental attention as promising candidates for realizing the physics of the Kitaev honeycomb model.

In this thesis, we focus our attention on the alkali iridate Na_2IrO_3, and probe the underlying interactions in this material by using a combination of magnetometry studies, at very high magnetic fields up to 60 T, and large-scale exact diagonalization simulations [229]. From our analysis, we find evidence for strong ferromagnetic Kitaev correlations in this system, and signatures of the much sought-after field-induced quantum spin liquid state, which has also been discussed extensively in the context of $\alpha-RuCl_3$ [73, 74, 230, 231].

5.1 Properties of 5d transition metal oxides: Mott physics and local moment formation

Here, we discuss the formation of spin-orbit entangled $\widetilde{j} = \frac{1}{2}$ moments in 4d and 5d transition metal compounds, considering, in particular, the example of the $5d^5$ system Na_2IrO_3, which is relevant for the purpose of this thesis.

In Na_2IrO_3, each iridium ion is surrounded by an octahedral cage of oxygen O^{2-}anions with a sixfold coordination, and is in the Ir^{4+} configuration, with five electrons in the 5d subshell. The arrangement of the negatively charged oxygen ions, in a distribution that is not spherically symmetric, leads to a splitting in the ten-fold degeneracy of the 5d orbitals,

known as the crystal field splitting. In octahedrally coordinated compounds with an O_h point group symmetry, the d-levels are split into four-fold degenerate e_g and six-fold degenerate t_{2g} subspaces. The t_{2g} orbitals have a lower energy as compared to the e_g orbitals, and in the limit where the octahedral crystal splitting is large, the e_g manifold can be projected out. Since the Hund's coupling, favoring a high-spin state, is almost an order of magnitude smaller than the crystal field energy scale in these systems, the five electrons in the t_{2g} manifold give rise to a low spin-1/2 configuration. One can then treat the spin-orbit interaction in the e_g and t_{2g} subspaces separately, with the latter being equivalent to a triply degenerate manifold of atomic p-orbitals. This is because the angular momentum of the d-orbitals, projected to the t_{2g} subspace, can be mapped to a set of effective $\widetilde{l} = 1$ angular momentum operators, with an additional minus sign. Next, taking the spin-orbit coupling term into consideration, the t_{2g} multiplet is split into a $\widetilde{j} = \frac{1}{2}$ doublet and a $\widetilde{j} = \frac{3}{2}$ quartet. The $\widetilde{j} = \frac{3}{2}$ quartet is lower in energy, and the $\widetilde{j} = \frac{1}{2}$ Kramers' doublet accommodates one electron, or equivalently one hole. Please see Fig. 5.1 for an illustration of the process of formation of these local moments. Due to the orbital component, the $\widetilde{j} = \frac{1}{2}$ moments and their exchange interactions are sensitive to the bonding geometries on the lattice. The $\widetilde{j} = \frac{1}{2}$ bands have a relatively narrow bandwidth, and even a modest onsite Coulomb repulsion U can open a Mott-like gap in the half-filled band.

5.2 Kitaev physics in transition metal compounds

The Kitaev honeycomb model [77] is one of the few known examples of theoretical models exhibiting a quantum spin liquid ground state, and it has been proposed that such an interaction can be realized between the $\widetilde{j} = \frac{1}{2}$ pseudo-spins in the classes of spin-orbit entangled Mott insulators discussed above [18]. Here, we briefly describe the salient features of this model, and discuss how the bonding geometries in the honeycomb iridates give rise to a dominant bond-directional Kitaev interaction, along with other competing isotropic and anisotropic interaction terms, which constitute the effective spin models used for describing these materials.

5.2.1 The Kitaev model

The Kitaev model is an example of a Kugel-Khomskii compass model [232, 233], in which spin–spin interactions along each bond are anisotropic, and depend on the orientation of the bond. This model comprises of spin-1/2 degrees of freedom on a honeycomb lattice, coupled via strongly anisotropic nearest-neighbor Ising interactions with bond-dependent easy axes,

given by

$$H = \sum_{<ij>,\gamma} J_{ij} S_i^\gamma S_j^\gamma,$$

where $\gamma = \{x, y, z\}$ and the bond $< ij >$ is of type γ. Each site thus corresponds to three flavors of bonds. An exact solution of the model can be obtained by representing the spin operators in terms of four types of Majorana fermions $\{b_i^x, b_i^y, b_i^z, c_i\}$, such that $S_i^\gamma = \frac{i}{2} b_i^\gamma c_i$. The Hamiltonian is then written as

$$H = \frac{1}{4} \sum_{<ij>} b_i^\gamma b_j^\gamma c_i c_j$$

The bilinear operators $\widehat{u}_{ij} = i b_i^\gamma b_j^\gamma$ commute with each other as well as the Hamiltonian, and can be replaced by their expectation values. This gives rise to the quadratic Hamiltonian

$$H = -\frac{i}{4} \sum_{<ij>} < \widehat{u}_{ij} > c_i c_j.$$

This form can be exactly diagonalized for a given configuration of $< \widehat{u}_{ij} >$, reducing to a non-interacting Majorana hopping Hamiltonian in a static background Z_2 gauge field. The Hilbert space on each site is enlarged from dimension 2 to 4, but the physical Hilbert space can be recovered by using a projection operator $P_j = \frac{1}{2}(1 + b_x^j b_y^j b_z^j c^j)$ for each lattice site. The projection operator acting on a site j flips all the $\widehat{u}$ operators emanating from this site. The emergent flux degrees of freedom are described by the plaquette operator $W_p = S_1^x S_2^y S_3^z S_4^x S_5^y S_6^z = \prod_{i=1}^6 u_{i,i+1}$. The eigenvalues of the plaquette operator are ± 1. All the plaquette operators commute with each other and with the Hamiltonian, and thus describe constants of motion. As a result of the macroscopic number of conserved quantities, the discussion can be restricted to a given flux sector. On the honeycomb lattice, the lowest energy corresponds to a situation with $W_p = +1$ on every hexagonal plaquette, i.e. the 'flux-free' condition. The ground state is a spin-liquid with short-range nearest neighbour spin-spin correlations, and consists of localized and itinerant Majorana fermions [176]. When one of the coupling constants of the model, J_γ is much larger than the others, the system is in a gapped QSL phase, whereas an extended gapless QSL is realized around the isotropic point $J_x = J_y = J_z = J_K$.

5.2.2 Bonding geometries and magnetic interactions

The honeycomb iridates A_2IrO_3 (A=Na,Li) consist of layers of edge-sharing IrO_6 octahedra, alternating with layers of Li/Na atoms. The Ir ions in each layer lie on a honeycomb lattice.

For Na_2IrO_3, the unit cell is known to have a monoclinic C2/m symmetry [86], and the IrO_6 octahedra are slightly asymmetric. The geometric orientation of the neighbouring octahedra plays a crucial role in determining the microscopic exchange of the magnetic moments located on the Ir ions at the center of these octahedra. As discussed in the previous section, in the case of the honeycomb iridates, neighboring IrO_6 octahedra share edges, and the two symmetric Ir-O-Ir exchange paths, with bond angles of 90°, lead to the emergence of Kitaev-like interactions in this system. In contrast, for perovskite iridates, such as Sr_2IrO_4 [36], two neighboring IrO_6 octahedra share a corner, with a single Ir-O-Ir exchange path, referred to as a $180^\circ-$bond. This is illustrated in Fig. 5.2.

Given the spin-orbital nature of the local moments, the interactions between them are expected to be highly anisotropic. In general, these can be written as

$$H = \sum_{ij} J_{ij}\mathbf{S_i}.\mathbf{S_j} + D_{ij}.(\mathbf{S_i}\times\mathbf{S_j}) + \mathbf{S_i}.\Gamma_{ij}.\mathbf{S_j} \tag{5.1}$$

where J_{ij} is the isotropic Heisenberg coupling, D_{ij} is Dzyaloshinskii-Moriya (DM) vector [234, 4] and Γ_{ij} is the symmetric pseudo-dipolar tensor. The realization of a pure Kitaev model requires that $J_{ij}, D_{ij} \to 0$ for every bond and only one component of the Γ_{ij} tensor remains nonzero. For idealized edge-sharing octahedra with inversion symmetry, all leading order contributions to the interactions vanish, and at the next higher order, the only nonzero component of Γ_{ij} is the Kitaev term. This is because the hopping of holes between the $\widetilde{j} = \frac{1}{2}$ states vanishes due to an interference between the symmetrically placed superexchange paths, via the oxygen 2p orbitals. As the next higher order contribution, bond-directional interactions arise from hopping between a $\widetilde{j} = \frac{1}{2}$ state and the $m = \pm\frac{3}{2}$ component of the $\widetilde{j} = \frac{3}{2}$ quartet of the adjacent site, and the Hund's coupling J_H between the $\widetilde{j} = \frac{1}{2}$ and excited $\widetilde{j} = \frac{3}{2}$ moments [18], which determine the strength of the Kitaev interaction.

In real materials, the magnetic interactions involve various competing terms along with the Kitaev interaction. In the presence of a direct overlap of Ir 5d orbitals, and due to the spatially extended nature of these orbitals, nearest-neighbor and further neighbor Heisenberg terms must both be taken into account in a realistic scenario. A symmetric off-diagonal exchange Γ is also allowed by symmetry [78], considering the most idealized crystal structure. An additional symmetric off-diagonal exchange Γ' is introduced due to the trigonal distortion of the oxygen octahedra [79]. The effective magnetic interactions between the local moments

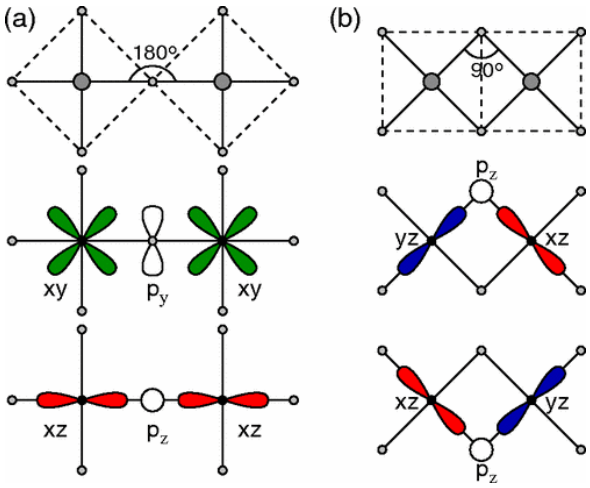

Fig. 5.2 The figure shows two possible geometries of a TM-O-TM bond with corresponding orbitals active along these bonds. The large (small) dots stand for the transition metal (oxygen) ions. (a) A 180°-bond formed by corner-shared octahedra, and (b) a 90°-bond formed by edge-shared octahedra. (Figure has been reproduced from Ref. [18] with permission)

are thus written as

$$H = \sum_{<ij>,\gamma(\alpha\beta)} J_{ij}\mathbf{S_i}.\mathbf{S_j} + K_{ij}S_i^{\gamma}S_j^{\gamma} + \Gamma_{ij}(S_i^{\alpha}S_j^{\beta} + S_i^{\beta}S_j^{\alpha}) + \Gamma'_{ij}(S_i^{\beta}S_j^{\gamma} + S_i^{\gamma}S_j^{\beta} + S_i^{\alpha}S_j^{\gamma} + S_i^{\gamma}S_j^{\alpha}) + \sum_{\ll ij \gg} J_2\mathbf{S_i}.\mathbf{S_j} + \sum_{\lll ij \ggg} J_3\mathbf{S_i}.\mathbf{S_j} \quad (5.2)$$

where γ refers to the spin component corresponding to the bond $< ij >$ under consideration, $\ll ij \gg$ and $\lll ij \ggg$ refer to the next-nearest and next-to-next nearest neighbor bonds respectively, and α and β correspond to the remaining two components. The phase diagram of the above Hamiltonian in Eq. 5.2 has been studied in great detail. The first extension considered for the Kitaev model on the honeycomb lattice was with an isotropic Heisenberg term, to yield the Kitaev-Heisenberg model. The importance of longer range Heisenberg interactions J_2 and J_3 [70, 235], and finite nearest-neighbor off-diagonal interactions Γ and Γ' [78, 79], and the role of the next nearest neighbor Kitaev interaction (K_2) [82] were later investigated.

5.3 Sodium iridate: existing results

Na_2IrO_3 is a layered Mott insulator with a bulk charge gap $E_g = 340$ meV [69] and spin-orbit coupling strength $\lambda \approx 0.5$ eV [21]. The bulk electrical resistivity of this material shows an insulating behavior with large room-temperature values (∼20-35 Ω cm), a pronounced

increase upon cooling and strong directional anisotropy [236, 87]. The magnetic susceptibility follows a Curie-Weiss law at high temperatures, with the Curie-Weiss temperature $\Theta_{CW} \approx -116$ K and an effective Ir moment $\mu_{eff} = 1.82\mu_B$, close to the value of $1.74\mu_B$ expected for spin-1/2 moments [68, 236, 86]. The effective moments are weakly dependent on the field direction, but the magnetic susceptibility is strongly anisotropic, indicated by the strong directional dependence of the Curie-Weiss temperature Θ_{CW}. X-ray absorption spectroscopy indicates a small admixture of $\widetilde{j} = \frac{1}{2}$ and $\widetilde{j} = \frac{3}{2}$ states [237]. A small trigonal distortion of the IrO_6 octahedra results in a crystal field splitting of the $\widetilde{j} = \frac{3}{2}$ states of about 110 meV, from resonant inelastic x-ray scattering (RIXS) measurements [238, 239], which, however, is considerably smaller than the typical strength of the spin-orbit coupling in the iridates. Neutron and x-ray diffraction [68], inelastic neutron scattering (INS) [86], and resonant inelastic x-ray scattering (RIXS) [71] measurements reveal a low temperature zigzag ordered state with an ordered moment $\mu_{ord} \approx 0.2\mu_B$, and with moments ordered at 45° from the crystallographic ab plane and the cubic x,y axes of the IrO_6 octahedra [236, 86, 68]. The ordering temperature T_N is found to be ≈ 15 K [68]. The suppression of the ordering temperature far below the Curie-Weiss temperature indicates the presence of strong frustration in the system.

On the theoretical front, the parameter space of couplings for Na_2IrO_3 has thus far been constrained using ab initio computations [81, 70, 84, 85], numerical techniques such as exact diagonalization [78, 79, 67, 228], classical Monte Carlo simulations [82, 240], and degenerate perturbation theory [67, 228, 235, 78, 79], as well as experimental investigation [86]. The simplest competing interaction term considered along with a dominant Kitaev exchange is an isotropic nearest-neighbor Heisenberg term. Within the nearest-neighbor Heisenberg-Kitaev model, with the Heisenberg interaction $J_H > 0$ and the Kitaev interaction $J_K < 0$ [70, 87, 235] (as suggested by quantum chemistry and other ab-initio calculations), a zigzag magnetic order cannot be realized. It was later realized that the zigzag order can be restored by the presence of second- and third-neighbor Heisenberg couplings (J_2,J_3) [70, 235], large anisotropic Γ/Γ' [78, 79], and enhanced by the presence of a second-neighbor Kitaev coupling K_2 [82]. Even within the nearest-neighbor model, a zigzag ground state can be obtained provided we consider a ferromagnetic Heisenberg interaction $J_H < 0$ and an antiferromagnetic Kitaev term $J_K > 0$ [67].

For our calculations, we refer to a model with a dominant antiferromagnetic Kitaev exchange as *Model A*, and a model with a dominant ferromagnetic Kitaev and a smaller antiferromagnetic Heisenberg term as *Model B* when accompanied by further-neighbor Heisenberg interactions, and *Model C* when supplemented by additional anisotropic inter-

actions. We distinguish between these different categories of models using the high-field magnetoresponse of Na_2IrO_3, accompanied by exact diagonalization simulations.

5.4 Open questions: spin liquid physics in Kitaev materials

Although most of the known Kitaev materials have been found to exhibit magnetic order at sufficiently low temperatures, due to the presence of competing isotropic interactions along with the dominant Kitaev term, the possibility of tuning these systems towards a spin liquid ground state using external parameters such as an applied pressure [241, 20] or magnetic field [242–244] has been extensively explored. In particular, there have been numerous studies, aiming to confirm the presence of a field-induced spin liquid phase in the 4d transition metal compound $\alpha-RuCl_3$, and to understand the nature of this phase. $\alpha-RuCl_3$, which has a lower ordering temperature and a more idealized honeycomb lattice structure as compared to Na_2IrO_3, has emerged as an extremely popular candidate for realizing Kitaev physics in recent times [242, 245]. Among the most prominent findings in this material, a robust magnetic scattering continuum has been observed in inelastic neutron scattering (INS) [242, 246] as well as Raman scattering [247, 248] studies, and has been interpreted as a signature of fractionalized excitations. In the latter case, the asymptotic two-fermion form has been fitted to the Raman scattering response, indicating the presence of fermionic excitations. More recently, new field dependent INS [249] and Raman scattering [250] experiments have been performed, which use improved experimental methods and analysis, and explore higher field regimes. Besides, experimental avenues such as specific heat [243, 251], magnetic susceptibility [251], nuclear magnetic resonance (NMR) [73, 251], electron spin resonance (ESR) [252], thermal conductivity [88, 253, 254], terahertz spectroscopy [244, 74, 255, 256] and magnetization [88] measurements have been explored to understand the nature of the excitations in the high-field phase, and in particular, whether these are gapped or gapless excitations. Recently, there has been evidence for a quantized thermal Hall conductance [231] in $\alpha-RuCl_3$ at low temperatures, as a function of the applied magnetic field, with the quantization value being half of the two-dimensional thermal Hall conductance of the integer quantum Hall effect. This half-integer quantization of the thermal Hall conductance is a signature of topologically protected chiral edge currents of charge-neutral Majorana fermions, which can be treated as half of a conventional fermion. These results demonstrate the fractionalization of spins into itinerant Majorana fermions and Z_2 fluxes, which is predicted to occur in Kitaev spin liquids [77]. Motivated by this

observation, the effects of non-Kitaev exchange interactions on the gapped chiral spin liquid state have also been investigated recently [257], and it has been found that off-diagonal exchange interaction Γ' significantly enhances the mass gap of the Majorana fermions, which explains the temperatures at which the quantized thermal Hall conductance is apparently observed. However, the observed quantization is not unambiguous, and if not quantized, there are other effects, such as the Berry curvature of magnon bands [258] or the interplay of a second-neighbor Dzyaloshinskii-Moriya interaction and a Zeeman coupling for emergent spinons in non-Kitaev spin liquids [259], that can explain the non-trivial value of the thermal Hall conductance at low temperatures and high fields.

The role of the high-field torque response in understanding the nature of the field-induced spin liquid phase has generally been underemphasized, although it has gained some popularity in recent times [260, 261]. In this connection, our collaborators from Dr. Suchitra Sebastian's group in Cavendish laboratory have performed high-field torque magnetometry measurements [262] for fields up to 60 T, for Na_2IrO_3, a sister Kitaev material of $\alpha-RuCl_3$, where most of the interesting physics is found to occur at much higher energy scales. These measurements were among the first for a Kitaev material at such high fields, and revealed hitherto unknown features, later theoretically interpreted by us, and described in this thesis, to possibly provide evidence for a field-induced spin liquid phase in this material. The experimental data shows a robust characteristic nonmonotonous peak-dip feature in the torque response, corresponding to the zigzag ordering scale of Na_2IrO_3. The high-field measurements enable us to access a regime where the behavior of the system is governed entirely by the Kitaev interaction. From our numerical simulations, we find that for field values exceeding the position of the peak-dip feature, there is no dominant magnetic order in the system. The spin-spin correlations tend to decay, beyond the nearest neighbors, with increasing magnetic field strength, thus implying the presence of a short-range correlated phase at high fields. Our conclusions are supported by recent resonant inelastic x-ray scattering (RIXS) results on Na_2IrO_3 and $\alpha-Li_2IrO_3$ [263], where a broad continuum of magnetic excitations that persists up to at least 300 K has been observed. RIXS measurements of the dynamical structure factor for energies within the continuum show that dynamical spin-spin correlations are restricted to nearest neighbors. This is consistent with the interpretation of a field-induced spin liquid phase at high fields, as evidenced by continuum scattering and a possible half-quantized thermal Hall conductivity in the case of $\alpha-RuCl_3$. Incidentally, a similar peak-dip feature has also been observed for $\alpha-RuCl_3$ [88], at an energy scale corresponding to the zigzag ordering scale of that material, and is found to disappear at temperatures exceeding the zigzag ordering temperature (≈ 7 K). However, no theoretical interpretation of this feature has been provided. Our work explores

underlying universalities in these Kitaev materials, and we expect many of our results to hold for $\alpha-\mathrm{RuCl_3}$ as well.

Chapter 6

High-field torque magnetometry in Na_2IrO_3: possibility of a field-induced spin liquid phase

In this part of the thesis, the magnetoresponse of the Mott-insulating honeycomb iridate Na_2IrO_3 is investigated using torque magnetometry measurements at high fields up to 60 T [229]. A robust characteristic peak-dip structure is observed in the torque response at magnetic fields corresponding to an energy scale close to the zigzag ordering temperature ($\approx$ 15 K) of this material. Using exact diagonalization simulations, we show that such a distinctive feature in the torque response constrains the effective spin models for these classes of Kitaev materials to ones with a dominant ferromagnetic Kitaev interaction, while alternative models with a dominant antiferromagnetic Kitaev interaction are excluded. We further show that, at high magnetic fields, long range spin correlation functions decay rapidly beyond the nearest neighbor, which indicates the possibility of a transition to a field-induced quantum spin liquid phase beyond the position of the peak-dip feature in the torque response. Below, we describe the experimental details, theoretical modeling, exact diagonalization algorithm and the results of our calculations.

My role in this joint experiment-theory work, reported below, has been the performance of extensive numerical simulations over a large parameter space, and the theoretical interpretation of the results.

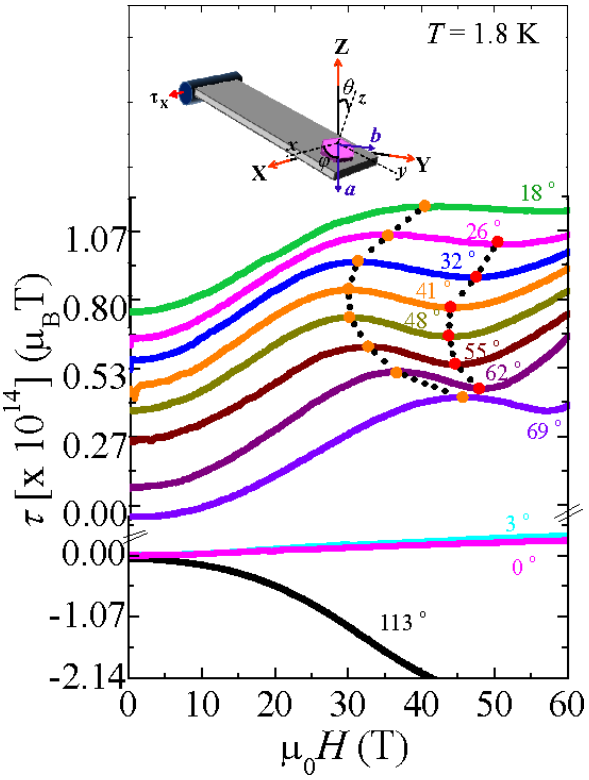

Fig. 6.1 The figure shows the magnetic torque (τ) measured as a function of magnetic field for different polar angular orientations (θ) and azimuthal angle $\phi = 90°$. A peak dip structure is observed in the magnetic torque, and is seen to evolve with θ. Individual torque curves have been offset for clarity. (Inset: a crystal on the cantilever with the various coordinate systems: XYZ $\rightarrow$ lab frame; xyz $\rightarrow$ frame fixed to the cantilever, so that X and x coincide. θ is the angle that the normal to the crystal makes with the magnetic field, and the measured magnetic torque along the X direction is referred to as τ.)

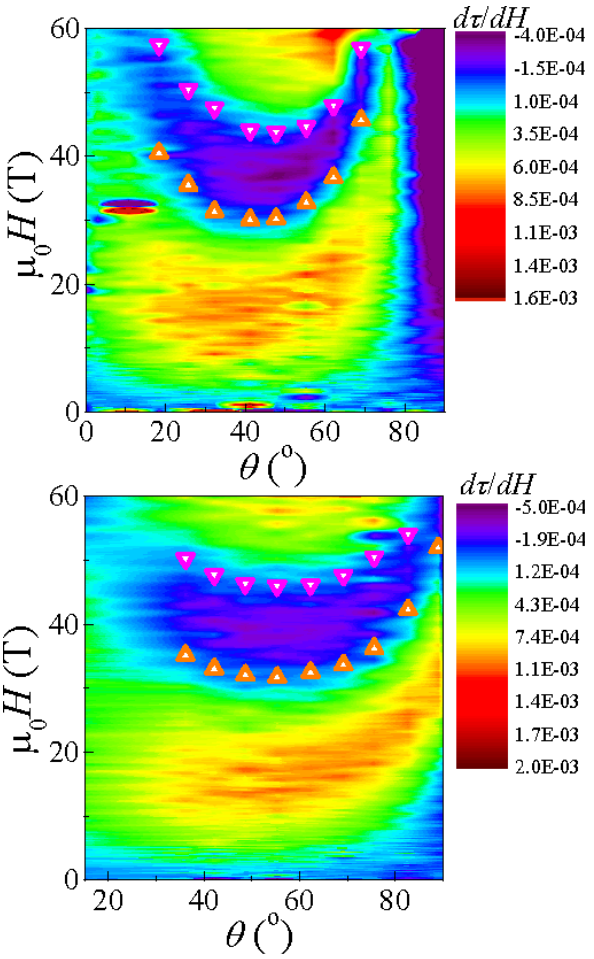

Fig. 6.2 The figure shows the derivative of experimentally measured magnetic torque with respect to magnetic field ($\frac{d\tau}{dH}$) as a function of magnetic field and angle (θ) for $\phi = 90^\circ$ (top) and $\phi = 0^\circ$ (bottom). The position of the maxima in the torque is indicated by regular triangles, while that of the subsequent minima is marked by inverted triangles.

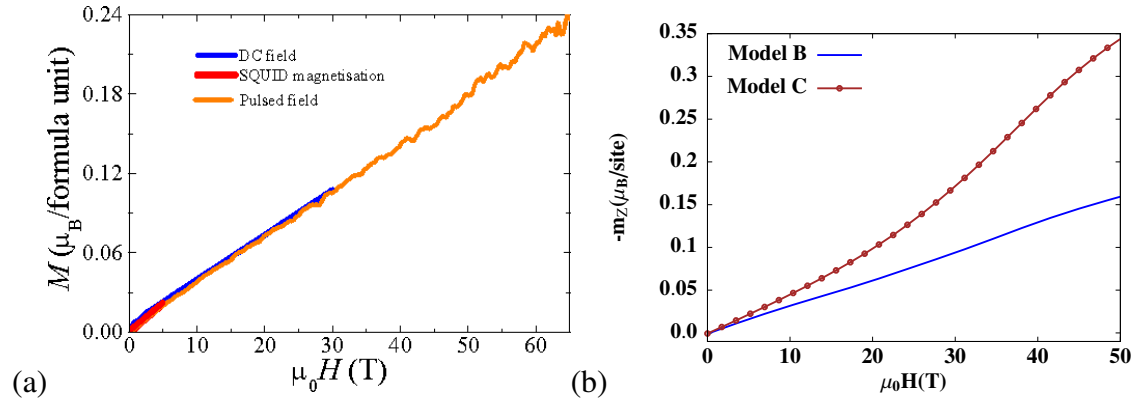

Fig. 6.3 The figure shows the (a) isotropic magnetization measured using an extraction magnetometer in pulsed magnetic fields, and using a force magnetometer in DC fields, which shows no features up to 60 T, where the calibration is performed using magnetization measurements on a pellet of Na_2IrO_3 in a SQUID magnetometer, and the (b) isotropic magnetization m_Z (in μ_B per atom) calculated as a function of field, for *Model B* with $J_h = 2.4$, $J_K = -12.0$, $J_2 = 1.6$, $J_3 = 1.2$ (in meV) for the orientation $\theta = 18^\circ$, $\phi = 90^\circ$, and for *Model C* with $J_h = 4.0$, $J_K = -16.0$, $\Gamma = 2.4$ and $\Gamma' = -3.2$ (in meV), for the orientation $\theta = 36^\circ$, $\phi = 0^\circ$.

6.1 Experimental details and salient features of the data

A single crystal of Na_2IrO_3, of dimension $\approx 100\ \mu m$ on a side, with a much smaller thickness, was mounted on a piezoresistive cantilever and measured on an in situ rotating stage in pulsed magnetic fields up to 60 T. The torque response (τ) was measured as a function of the magnetic field at various fixed angles ($0^\circ \lesssim \theta \lesssim 90^\circ$) of the crystalline axis normal to the honeycomb lattice, with respect to the magnetic-field axis. A distinctive nonmonotonic feature is observed in the magnetic torque response. A peak in the magnetic torque in the vicinity of 30–40 T is followed by a dip in the vicinity of 45–55 T. The peak and dip features are separated by as much as ≈ 15 T near $\theta \approx 45^\circ - 55^\circ$, but draw closer together at angles closer to $\theta \approx 0^\circ$ and $\theta \approx 90^\circ$. The experimental torque response, for a range of angles θ, is depicted in Fig. 6.1. In the vicinity of $\theta \approx 0^\circ$ and $\theta \approx 90^\circ$, the peak and dip features are seen to merge into a single plateaulike feature. This evolution of the signature peak-dip feature as a function of field-inclination angle and magnetic field is shown in Fig. 6.2 for two different azimuthal orientations ($\phi = 0^\circ, 90^\circ$), where ϕ is the angle that the crystallographic a axis makes with the axis of rotation of the cantilever. The high-field torque response of Na_2IrO_3 was independently measured for two crystals, for three different azimuthal orientations (ϕ = 0°, 90° and 180°), at a temperature of 1.8 K and results for both were found to be very similar. The signature peak-dip feature is found to disappear above the zigzag ordering temperature. Meanwhile, the isotropic magnetization (m_Z) measured using an extraction magnetometer in

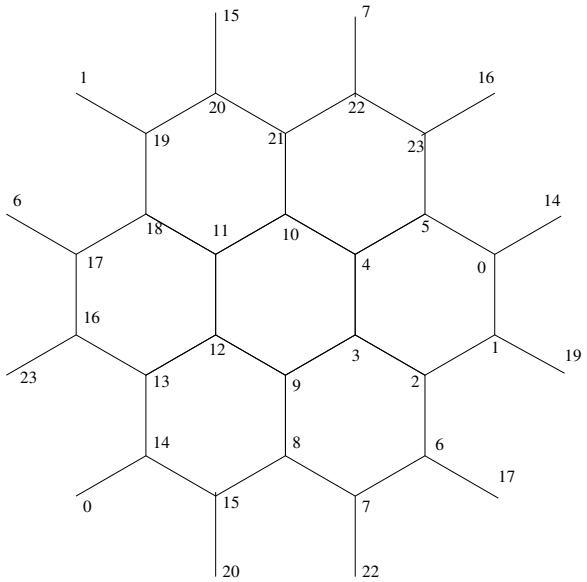

Fig. 6.4 The figure shows our hexagonal 24-site fragment with periodic boundary conditions.

Model	J_h	J_K	J_2	J_3	Γ	Γ'
Antiferromagnetic Kitaev (*Model A*)	-	+	×	×	×	×
Ferromagnetic Kitaev (*Model B*)	+	-	+	+	×	×
Ferromagnetic Kitaev (*Model C*)	+	-	×	×	+	-

Table 6.1 Models considered for exact diagonalization calculations, where J_h refers to the nearest-neighbor Heisenberg interaction, J_K refers to the Kitaev interaction, J_2 and J_3 refer to further-neighbor Heisenberg terms, and Γ and Γ' refer to symmetric off-diagonal exchange interactions.

pulsed magnetic fields up to 60 T, and a force magnetometer in steady fields up to 30 T, is found to be largely featureless and to increase linearly with magnetic field up to 60 T (see Fig. 6.3).

6.2 Theoretical Modeling

We use theoretical modeling of the nonmonotonous peak-dip features that we observe in the high field torque response, in order to distinguish between potential microscopic models. Our starting point is the usual spin Hamiltonian [235, 67] with nearest-neighbor Kitaev and Heisenberg interactions:

$$J_h \sum_{<ij>} \vec{\sigma_i}.\vec{\sigma_j} + J_K \sum_{<ij>} \sigma_i^\gamma \sigma_j^\gamma \tag{6.1}$$

where $\gamma = x, y, z$ labels an axis in spin space and a bond direction of the honeycomb lattice, and the Hamiltonian is expressed in terms of Pauli matrices $\overrightarrow{\sigma_i}$. *Model A* with dominant antiferromagnetic Kitaev correlations is parameterized by nearest-neighbor interactions $J_h < 0$ and $J_K > 0$ [67]. In *Model B*, further neighbor antiferromagnetic Heisenberg couplings J_2 and J_3 are introduced up to the third nearest neighbor [70], along with $J_h > 0$ and $J_K < 0$. In *Model C*, bond-dependent nearest-neighbor off-diagonal terms $H_{od}^{(\gamma)} = \Gamma \sum_{\alpha \neq \beta \neq \gamma} \sum_{\{i,j\}} (\sigma_i^\alpha \sigma_j^\beta + \sigma_i^\beta \sigma_j^\alpha)$ (α and β are the two remaining directions apart from the Kitaev bond direction γ) [78] and $H'_{od} = \Gamma' \sum_{\alpha \neq \beta \neq \gamma} \sum_{\{i,j\}} (\sigma_i^\beta \sigma_j^\gamma + \sigma_i^\gamma \sigma_j^\beta + \sigma_i^\alpha \sigma_j^\gamma + \sigma_i^\gamma \sigma_j^\alpha)$ [79] accounting for trigonal distortions of the oxygen octahedra are introduced. The main parameters of these models are summarized in Table 6.1.

For our calculations, we use a hexagonal 24-site cluster with periodic boundary conditions (see Fig. 6.4). The effect of the applied magnetic field $\overrightarrow{H} = H\hat{z}$ (in the lab frame) on the system is described by $H_{mag} = (\frac{g}{2}) \sum_i \sum_\gamma h_\gamma \sigma_i^\gamma$, with $g \sim 1.78$ [67] being the Lande g factor, assumed to be a constant, and $\overrightarrow{h} = (h_x, h_y, h_z)$ being the field as expressed in the crystal octahedron frame. Exact diagonalization calculations for the ground state energy and eigenvector are performed using a modified Lanczos algorithm. The code was benchmarked by reproducing the results in Ref. [67]. The N lattice sites were numbered $0, 1, 2...N-1$ (for $N = 24$), and specific pairs of these sites were identified as 'bonds' or 'links', of type x, y or z. Every site has a spin with two possible states $|1>$ or $|0>$. The system then has 2^N configurations or underlying basis states, where each configuration is denoted by $|s_{N-1}, s_{N-2}...s_0>$ with $s_i = 0, 1$. Corresponding to such a set of binary numbers, we have a decimal equivalent given by $|s_{N-1}\mathrm{x}2^{\mathrm{N}-1} + \mathrm{s}_{\mathrm{N}-2}\mathrm{x}2^{\mathrm{N}-2} + ... + \mathrm{s}_0\mathrm{x}2^0>$. The basis vectors were thus denoted as $|0>$, $|1>...|2^{N-1}>$. An arbitrary state vector $|\psi>$ can be expanded in terms of these basis vectors as $|\psi> = \sum_{i=0}^{2^{N-1}} a_i |i>$. The ground state Ψ_0 for this Hamiltonian H_0 was determined using the Modified Lanczos algorithm.

6.2.1 Modified Lanczos algorithm

The Modified Lanczos algorithm [264] requires the initial selection of a trial vector ψ_0 (constructed using a random number generator in our case) which should have a nonzero projection on the true ground state of the system in order for the algorithm to converge properly. A normalized state ψ_1, orthogonal to ψ_0, is defined as

$$\psi_1 = \frac{H_0\psi_0 - < H_0 > \psi_0}{\sqrt{< H_0^2 > - < H_0 >^2}}. \tag{6.2}$$

In the basis $\{\psi_0, \psi_1\}$, H_0 has a 2x2 representation which is easily diagonalized. Its lowest eigenvalue and corresponding eigenvector are better approximations to the true ground state energy and wavefunction than the quantities $< H_0 >$ and ψ_0 considered initially. The improved energy and wavefunction are given by

$$\varepsilon =< H_0 > +b\alpha \tag{6.3}$$

and

$$\widetilde{\psi}_0 = \frac{\psi_0 + \alpha\psi_1}{\sqrt{1+\alpha^2}} \tag{6.4}$$

where $b = \sqrt{< H_0^2 > - < H_0 >^2}$, $f = \frac{<H_0^3> -3<H_0><H_0^2> +2<H_0>^3}{2b^3}$ and $\alpha = f - \sqrt{1+f^2}$. The method can be iterated by considering $\widetilde{\psi}_0$ as a new trial vector and repeating the above steps. The Modified Lanczos method helps in obtaining a reasonably good approximation to the actual ground state of the system while storing only three vectors, ψ_0, $H_0\psi_0$ and $H_0^2\psi_0$ rather than the entire Hamiltonian in the spin basis representation. This is especially advantageous as the number of basis vectors increases rapidly with the number of spin sites. In the regular Lanczos algorithm, the matrix is first reduced to a tridiagonal form before computing the ground state eigenvector. However, there can be issues with the convergence to the true ground state because of loss of orthogonality among the vectors. This is circumvented in this algorithm as orthogonality is enforced at each and every step of the iteration.

After the determination of the ground state Ψ_0 to a reasonable approximation, the magnetization $\overrightarrow{m_{|\psi>}}$ was obtained in this state with components (m_x, m_y, m_z), where $m_\gamma =< \psi|\sum_{i=0}^{N-1}\sigma_i^\gamma|\psi >$, and was transformed to the lab frame from the octahedral frame, the components in the lab frame being (m_X, m_Y, m_Z). Finally, in the lab frame, the torque response is calculated as $\Gamma_X = m_Y H$.

6.2.2 Coordinate system transformations

For our exact diagonalization calculations, we have transformed the external magnetic field from the laboratory frame to the IrO_6 octahedral frame by defining intermediate crystal and cantilever axes, and transformed the calculated magnetization back from this frame to the lab frame. We explain the transformations used in the following:

Notations: *Laboratory axes*: $\hat{X}, \hat{Y}, \hat{Z}$

Cantilever axes: $\hat{x}$,$\hat{y}$,$\hat{z}$

Crystal axes: $\hat{a}, \hat{b}, \hat{c}$

Octahedral axes: $\hat{p}, \hat{q}, \hat{r}$

Laboratory to cantilever axes: The lab $\hat{X}$-axis and the cantilever $\hat{x}$-axis are always coincident. Let θ be the angle between the $\hat{Z}$ and $\hat{z}$ axes.We have

$$|\hat{x}\hat{y}\hat{z}> = M_{Lab\to Canti}|\hat{X}\hat{Y}\hat{Z}>$$

$$|\hat{X}\hat{Y}\hat{Z}> = L_{Canti\to Lab}|\hat{x}\hat{y}\hat{z}>$$

where

$$M_{Lab\to Canti} = \begin{pmatrix} 1 & 0 & 0 \\ 0 & \cos\theta & -\sin\theta \\ 0 & \sin\theta & \cos\theta \end{pmatrix}$$

$$L_{Canti\to Lab} = \begin{pmatrix} 1 & 0 & 0 \\ 0 & \cos\theta & \sin\theta \\ 0 & -\sin\theta & \cos\theta \end{pmatrix}$$

Cantilever to crystal axes: The honeycomb layer formed by the Ir atoms resides on the crystallographic *ab* plane. Let the $\hat{a}$-axis of the crystal make an angle ϕ with the $\hat{x}$-axis of the cantilever. Then,

$$|\hat{a}\hat{b}\hat{c}> = M_{Canti\to Crystal}|\hat{x}\hat{y}\hat{z}>$$

$$|\hat{x}\hat{y}\hat{z}> = L_{Crystal\to Canti}|\hat{a}\hat{b}\hat{c}>$$

$$M_{Canti\to Crystal} = \begin{pmatrix} \cos\phi & \sin\phi & 0 \\ -\sin\phi & \cos\phi & 0 \\ 0 & 0 & 1 \end{pmatrix}$$

$$L_{Crystal\to Canti} = \begin{pmatrix} \cos\phi & -\sin\phi & 0 \\ \sin\phi & \cos\phi & 0 \\ 0 & 0 & 1 \end{pmatrix}$$

Crystal to octahedral axes: Since the [111] direction in the octahedral frame is perpendicular to the honeycomb lattice, the unit vectors are related as follows:

$$\hat{c} = \frac{\hat{p}+\hat{q}+\hat{r}}{\sqrt{3}}$$

$$\hat{b} = \frac{-\hat{p}+\hat{q}}{\sqrt{2}}$$

$$\hat{a} = \frac{\hat{p}+\hat{q}-2\hat{r}}{\sqrt{6}}$$

Then,

$$|\hat{p}\hat{q}\hat{r}>= M_{Crystal\to Octa}|\hat{a}\hat{b}\hat{c}>$$

$$|\hat{a}\hat{b}\hat{c}>= L_{Octa\to Crystal}|\hat{p}\hat{q}\hat{r}>$$

$$M_{Crystal\to Octa} = \begin{pmatrix} \frac{1}{\sqrt{6}} & -\frac{1}{\sqrt{2}} & \frac{1}{\sqrt{3}} \\ \frac{1}{\sqrt{6}} & \frac{1}{\sqrt{2}} & \frac{1}{\sqrt{3}} \\ -\sqrt{\frac{2}{3}} & 0 & \frac{1}{\sqrt{3}} \end{pmatrix}$$

$$L_{Octa\to Crystal} = \begin{pmatrix} \frac{1}{\sqrt{6}} & \frac{1}{\sqrt{6}} & -\sqrt{\frac{2}{3}} \\ -\frac{1}{\sqrt{2}} & \frac{1}{\sqrt{2}} & 0 \\ \frac{1}{\sqrt{3}} & \frac{1}{\sqrt{3}} & \frac{1}{\sqrt{3}} \end{pmatrix}$$

Lab to octahedral and octahedral to lab frame: Let the components of the magnetic field be $(0,0,H)$ in the lab frame and (h_p,h_q,h_r) in the octahedral frame. Then

$$|h_p h_q h_r >= M_{Crystal\to Octa}M_{Canti\to Crystal}M_{Lab\to Canti}|00H>$$

which finally gives us

$$h_p = (-\frac{1}{\sqrt{6}}\sin\theta\sin\phi + \frac{1}{\sqrt{2}}\sin\theta\cos\phi + \frac{1}{\sqrt{3}}\cos\theta)H$$

$$h_q = (-\frac{1}{\sqrt{6}}\sin\theta\sin\phi - \frac{1}{\sqrt{2}}\sin\theta\cos\phi + \frac{1}{\sqrt{3}}\cos\theta)H$$

$$h_r = (\sqrt{\frac{2}{3}}\sin\theta\sin\phi + \frac{1}{\sqrt{3}}\cos\theta)H$$

Let the components of the magnetization vector $\overrightarrow{m}$ be (m_X,m_Y,m_Z) in the lab frame and (m_p,m_q,m_r) in the octahedral frame. Then,

$$|m_X m_Y m_Z >= L_{Canti\to Lab}L_{Crystal\to Canti}L_{Octa\to Crystal}|m_p m_q m_r>$$

from where we find

$$m_Z = (-\frac{m_p}{\sqrt{6}} - \frac{m_q}{\sqrt{6}} + m_r\sqrt{\frac{2}{3}})\sin\theta\sin\phi + \frac{m_p - m_q}{\sqrt{2}}\sin\theta\cos\phi + \frac{(m_p + m_q + m_r)}{\sqrt{3}}\cos\theta$$

and

$$m_Y = (\frac{m_p}{\sqrt{6}} + \frac{m_q}{\sqrt{6}} - m_r\sqrt{\frac{2}{3}})\cos\theta\sin\phi + \frac{(-m_p + m_q)}{\sqrt{2}}\cos\theta\cos\phi + \frac{(m_p + m_q + m_r)}{\sqrt{3}}\sin\theta$$

6.2.3 Structure factor calculations

The chosen parameter sets are verified to be consistent with the zigzag ground state of Na_2IrO_3 by calculating the adapted structure factors $S(\overrightarrow{Q})$ [265] acting as order parameters, to determine different phases of the system in the presence of an applied magnetic field. The corresponding dominant order wavevectors $\overrightarrow{Q} = \overrightarrow{Q_{max}}$ characterize the nature of the magnetic ordering in various field regimes. The static structure factors $S(\overrightarrow{Q})$ for different spin configurations are given by

$$S^{\gamma}_{zigzag} = \frac{1}{N^2}\sum_{r,r',\beta,\beta'} \exp[i\overrightarrow{Q_\gamma}.(\overrightarrow{r'} - \overrightarrow{r})]\nu_{\beta,\beta'}(<\overrightarrow{\sigma_{r,\beta}}.\overrightarrow{\sigma_{r',\beta'}}> - \sum_{\gamma} <\sigma^{\gamma}_{r,\beta}><\sigma^{\gamma}_{r',\beta'}>) \quad (6.5)$$

$$S_{Neel} = \frac{1}{N^2}\sum_{r,r',\beta,\beta'} \nu_{\beta,\beta'}(<\overrightarrow{\sigma_{r,\beta}}.\overrightarrow{\sigma_{r',\beta'}}> - \sum_{\gamma} <\sigma^{\gamma}_{r,\beta}><\sigma^{\gamma}_{r',\beta'}>) \quad (6.6)$$

$$S_{FM} = \frac{1}{N^2}\sum_{r,r',\beta,\beta'} (<\overrightarrow{\sigma_{r,\beta}}.\overrightarrow{\sigma_{r',\beta'}}> - \sum_{\gamma} <\sigma^{\gamma}_{r,\beta}><\sigma^{\gamma}_{r',\beta'}>) \quad (6.7)$$

$$S^{\gamma}_{stripy} = \frac{1}{N^2}\sum_{r,r',\beta,\beta'} \exp[i\overrightarrow{Q_\gamma}.(\overrightarrow{r'} - \overrightarrow{r})](<\overrightarrow{\sigma_{r,\beta}}.\overrightarrow{\sigma_{r',\beta'}}> - \sum_{\gamma} <\sigma^{\gamma}_{r,\beta}><\sigma^{\gamma}_{r',\beta'}>) \quad (6.8)$$

where each site is labeled by an index i and a position in the unit cell $\overrightarrow{r}$,β denotes the sublattice index ($\beta = A, B$), and $\gamma = x, y$ or z. The contribution to the structure factors coming from the alignment of the spins with the field direction has explicitly been deducted in this definition. The structure factors for the four different phases are plotted as a function of field for different models in Fig. 6.5, which clearly shows that AFM zigzag is the dominant spin configuration among these, in all cases.

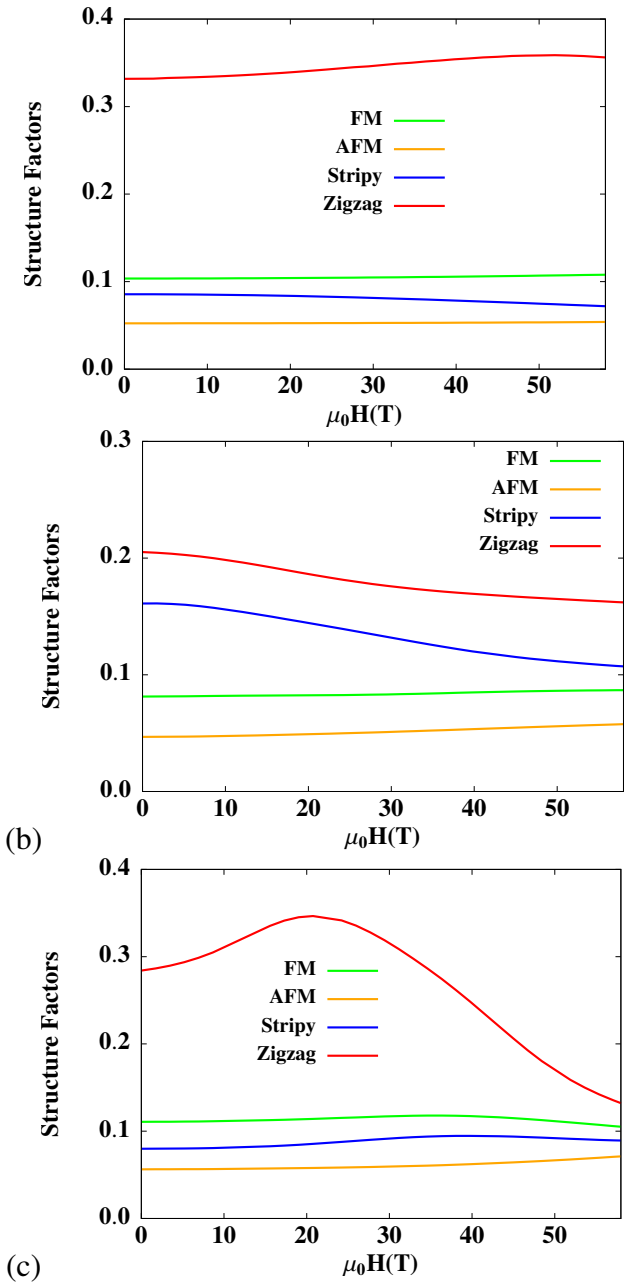

Fig. 6.5 The figure shows the evolution of structure factors for different ordered phases as a function of the field for (a) *Model A* with $J_h = -4.0$, $J_{\rm K} = 21.0$ (in meV), (b) *Model B* with, for instance, $J_h = 2.4$, $J_{\rm K} = -20.0$, $J_2 = 1.6$, $J_3 = 1.2$ (in meV) , and (c) *Model C* with $J_h = 4.0$, $J_{\rm K} = -16.0$, $\Gamma = 2.4$ and $\Gamma' = -3.2$ (in meV).

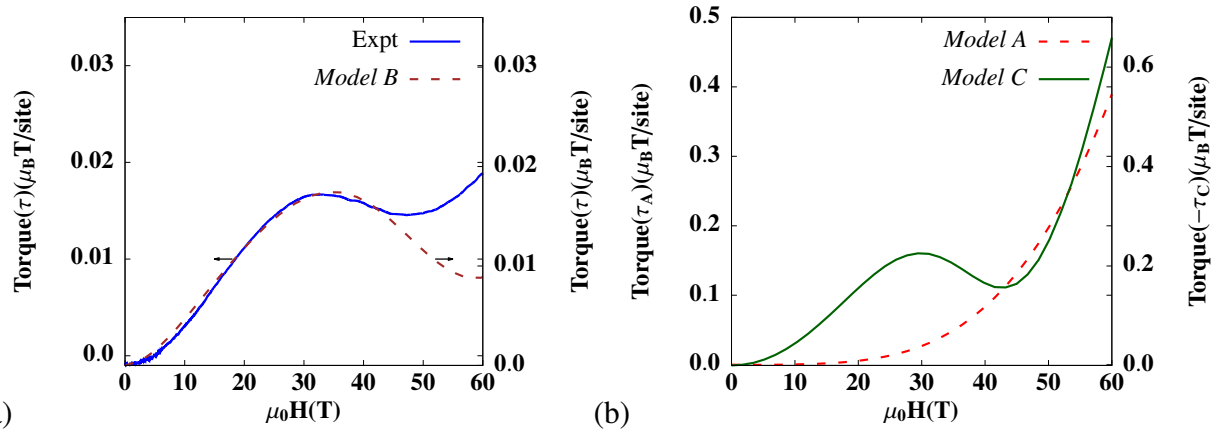

Fig. 6.6 (a) Magnetic torque as a function of magnetic field (in $\mu_B T$ per site) for *Model B* (denoted by τ_B) with parameters $J_h = 3.6$, $J_K = -30.0$ (in meV) for antiferromagnetic Heisenberg and dominant ferromagnetic Kitaev correlations, corresponding to the orientation $\theta = 42^\circ$, $\phi = 0^\circ$. In this case, further neighbor interactions $J_2 = 0.6$, $J_3 = 1.8$ (in meV) are necessary to stabilize a zigzag ground state. The experimental data (solid line) for this orientation is plotted along with the torque response (dashed line) calculated for this model for comparison. (b) Magnetic torque calculated as a function of magnetic field (in $\mu_B T$ per site) for *Model A* (denoted by τ_A) with parameters $J_h = -4.0$, $J_K = 21.0$ (in meV) for ferromagnetic Heisenberg and dominant antiferromagnetic Kitaev interactions, corresponding to the orientation $\theta = 36^\circ$, $\phi = 0^\circ$, and for *Model C* (denoted by τ_C) with parameters $J_h = 4.0$, $J_K = -16.0$, $\Gamma = 2.4$, and $\Gamma' = -3.2$ (in meV) for antiferromagnetic Heisenberg and dominant ferromagnetic Kitaev exchange, corresponding to the same orientation. In *Model A* (dashed line) characterized by a stable zigzag phase, no peak-dip feature appears, unlike experimental observations. In contrast, in *Model C* (solid line), where a fine-tuned zigzag phase requires the introduction of nearest-neighbor anisotropic terms Γ and Γ', the magnetic-field dependence of magnetic torque shows a peak-dip feature corresponding with experiment.

6.3 Numerical exact diagonalization results for the torque response

The calculated magnetic torque responses for the different models are shown in Fig. 6.6. We find the peak-dip feature in the magnetic torque response to be reproduced only by models with dominant ferromagnetic Kitaev interactions (i.e., *Models B* and *C*), whereas models with dominant antiferromagnetic Kitaev interactions (i.e., *Model A*) display instead a monotonic increase in the magnetic torque with magnetic field. The main parameters of the models considered for our simulations are summarized in Table 6.1. Fig. 6.7 shows the evolution of the peak-dip feature as a function of the field-inclination angle θ and the magnetic field for *Model B*, calculated using exact diagonalization. We have performed exact diagonalization

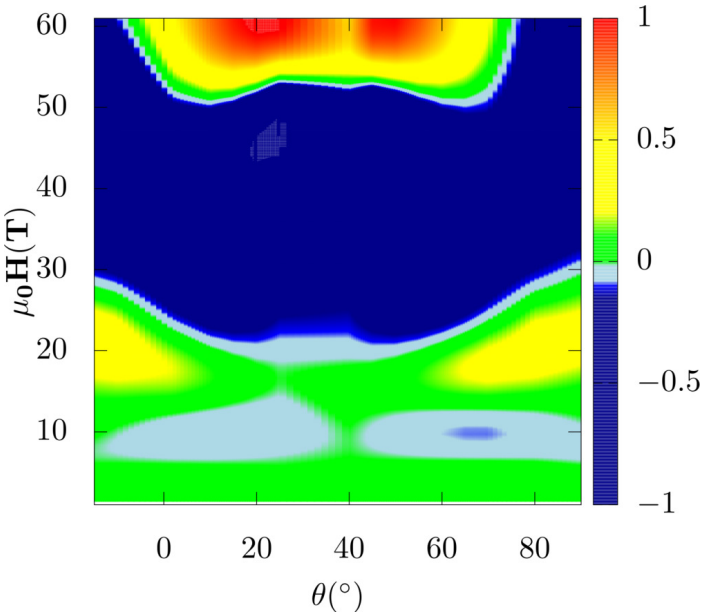

Fig. 6.7 Calculated contour plot of $\frac{d\tau}{dH}$ in the $\theta - H$ plane, for parameters $J_h = 3.6$, $J_K = -18.0$, $J_2 = 2.4$, and $J_3 = 1.8$ (in meV), i.e., *Model B*, corresponding to the azimuthal angle $\phi = 20^\circ$. We find that the position of the peak-dip feature, indicated by the regions where $\frac{d\tau}{dH}$ changes sign, shifts closer to the origin for increasing (decreasing) values of the polar angle θ for θ close to 0° (90°), in agreement with the experimental results. At the extreme values of θ, the width of the region of nonmonotonicity increases, which is at variance with experiment. The torque values obtained in our simulations can be negative, and in such cases we plot $-\frac{d\tau}{dH}$ instead.

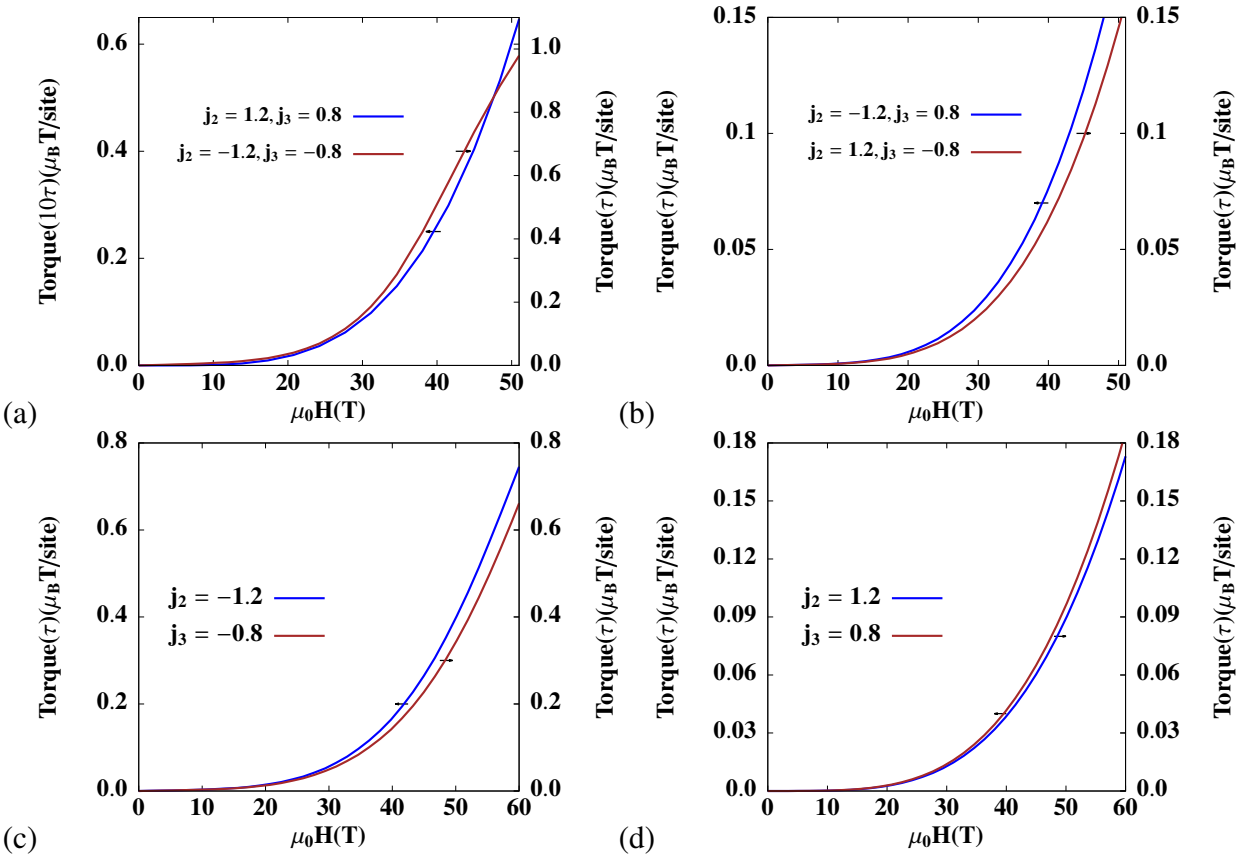

Fig. 6.8 The figures show the calculated torque response for different models with a ferromagnetic Heisenberg and antiferromagnetic Kitaev interaction with further neighbor Heisenberg interactions. Figures (a) and (b) correspond to $J_h = -4.0$, $J_K = 21.0$ (in meV) for the orientation $\theta = 48^\circ$, $\phi = 90^\circ$, for J_2 and J_3 interactions as indicated in the figure. We observe that further neighbour interactions J_2 and J_3 do not give rise to any peak-dip features in the torque response. In figures (c) and (d) above, we have considered combinations of parameters for $J_h = -4.0$, $J_K = 21.0$ (in meV) with either J_2 or J_3 terms present but not both. In (c), we consider J_2 or J_3 which is ferromagnetic and in (d), we consider these interactions to be antiferromagnetic, both for the orientation $\theta = 48^\circ$, $\phi = 90^\circ$. In neither case do we see any peak-dip features in the torque response.

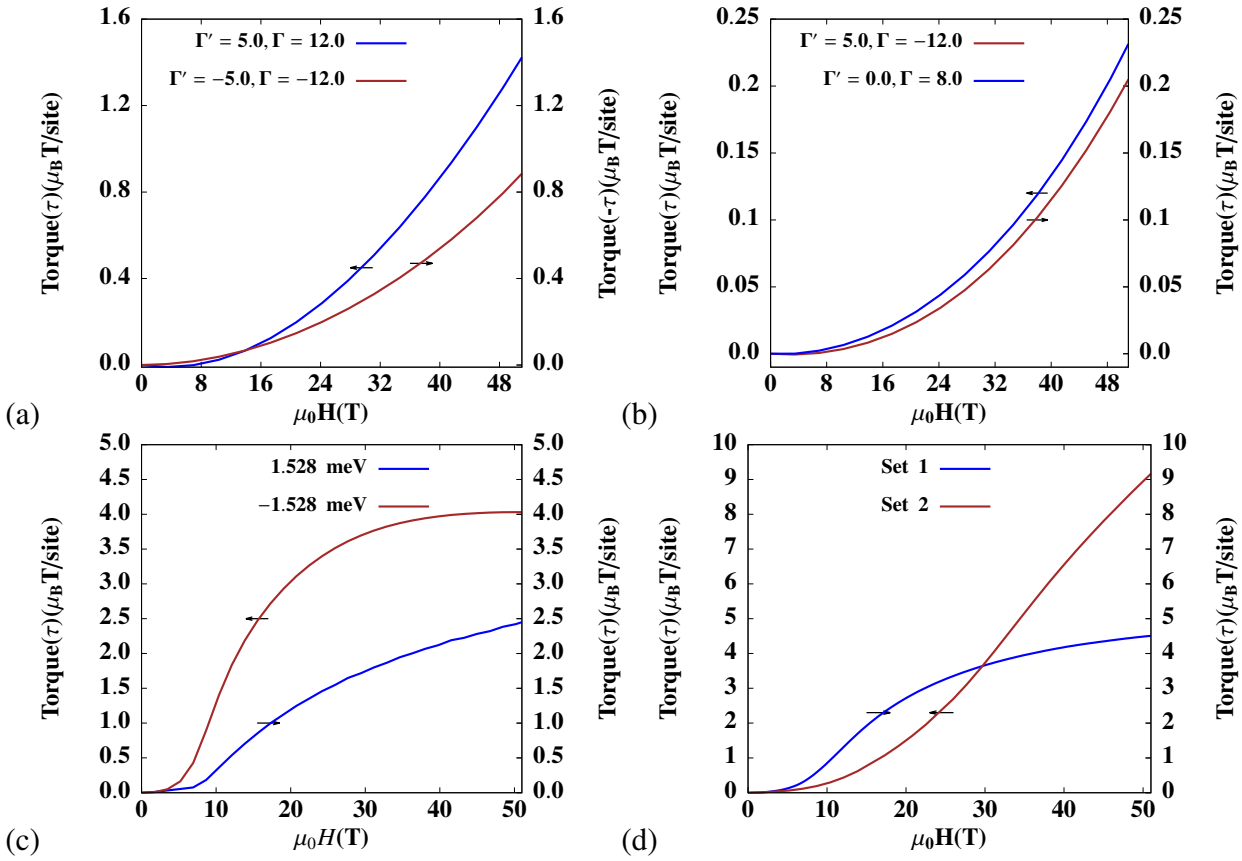

Fig. 6.9 The figures show the calculated torque response for different models with a ferromagnetic Heisenberg and antiferromagnetic Kitaev interaction with additional anisotropic parameters Γ and Γ'. Figures (a) and (b) show the calculated values of the torque for models with $J_h = -8.0$, $J_K = 40.0$ (in meV), for the orientation $\theta = 36^\circ$, $\phi = 0^\circ$, with Γ and Γ' values as indicated. We observe that additional Γ and Γ' terms do not give rise to any peak-dip features in the torque response. Figure (c) corresponds to parameter values $J_h = -1.84$, $J_K = 3.2$ (in meV) for the orientation $\theta = 69^\circ$, $\phi = 90^\circ$ with an additional Γ term with values indicated in the figure. Figure (d) shows the torque response for two sets of parameters with $J_h < 0$, $J_K > 0$ and $\Gamma > 0$ at different orientations of the field. Here **Set 1** corresponds to $J_h = -1.84$, $J_K = 3.2$ and $\Gamma = 1.528$ (in meV) for $\theta = 36^\circ$ and $\phi = 0^\circ$, and **Set 2** corresponds to $J_h = -12.0$, $J_K = 17.0$, and $\Gamma = 12.0$ (in meV) for $\theta = 48^\circ$ and $\phi = 90^\circ$.

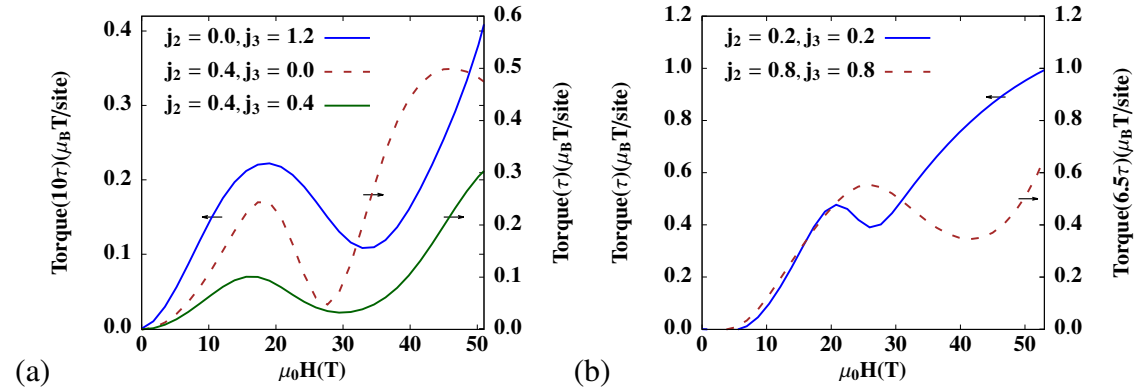

Fig. 6.10 The figure illustrates the calculated torque response for models with $J_h > 0$, $J_K < 0$ and various combinations of additional interactions J_2 and J_3. Here (a) shows the torque response for $J_h = 2.4$, $J_k = -20.0$ (in meV) for $\theta = 36^\circ$ and $\phi = 0^\circ$ with J_2 and J_3 values as indicated (in meV), and (b) shows the torque response for two sets of data where Set 1 corresponds to $J_h = 2.4$, $J_K = -12.0$, $J_2 = 0.2$ and $J_3 = 0.2$ (in meV) for $\theta = 32^\circ$ and $\phi = 90^\circ$, while Set 2 corresponds to $J_h = 2.4$, $J_K = -12.0$, $J_2 = 0.8$ and $J_3 = 0.8$ (in meV) for $\theta = 41^\circ$ and $\phi = 90^\circ$. We observe that peak-dip features, sometimes more than one, are observed in the expected field range for all of these models, even though most of them do not exhibit a zigzag ground state order. Moreover, the shift in the position of the peak-dip feature with an increase in the values of the parameters J_2 and J_3 is clearly seen in (b).

simulations for magnetic fields up to 300 T for *Model A* (for the parameters provided in the caption in Fig. 6.6), and found a single peak in the magnetic torque response at a magnetic field slightly lower than 150 T, beyond which the torque decreases with increase in field strength and no further features are observed in the torque response. We have also considered variants of *Model A* with isotropic J_2 and J_3 as well as anisotropic exchange interactions (see Figures 6.8 and 6.9), and have confirmed that this model does not give a peak-dip feature in its torque response, even with additional interaction terms present. Our results strongly indicate that Na_2IrO_3 is described by a model dominated by ferromagnetic Kitaev exchange. The distinctive peak-dip feature in the torque response thus provides an independent handle for constraining experimental data. Of the two types of ferromagnetic Kitaev exchange models we consider, in *Model B*, the peak-dip feature is observed over a large parameter range (in fact, larger than the space over which a zigzag ground state is seen, as illustrated in Fig. 6.10), while in *Model C*, the peak-dip feature only appears upon inclusion of a significant $\Gamma' < 0$ term, which physically is associated with trigonal distortion in Na_2IrO_3. The inclusion of significant anisotropic terms in *Model B* does not yield additional peak-dip features, with the peak-dip surviving only for relatively small values of additional anisotropic interactions.

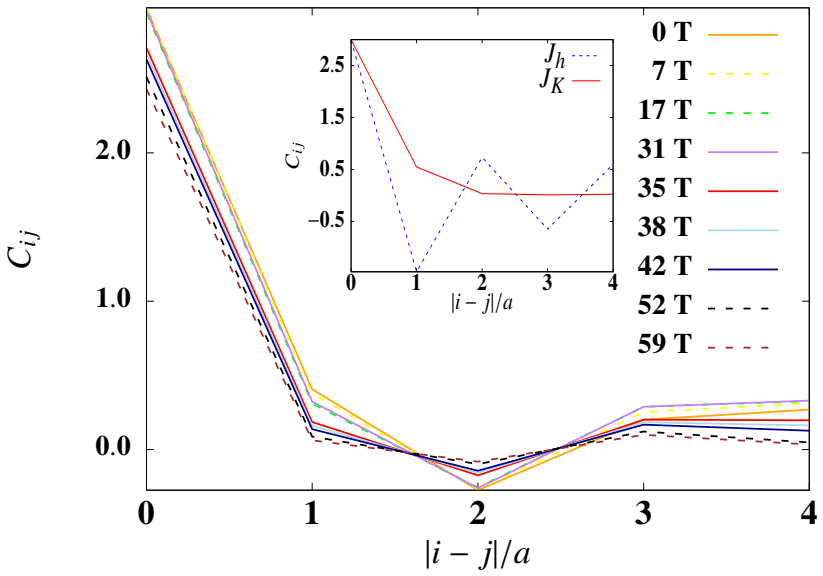

Fig. 6.11 The figure shows the correlation functions C_{ij} calculated as a function of $\frac{|i-j|}{a}$, a being the distance between two neighboring sites, with parameters $J_h = 4.0$, $J_K = -16.0$, $\Gamma = 2.4$, and $\Gamma' = -3.2$ (in meV), for an orientation of $\theta = 36^\circ$, $\phi = 0^\circ$. The inset shows the corresponding plots for a pure Heisenberg model with $J_h = 16.0$ meV (blue) and for a pure Kitaev model with $J_K = -16.0$ meV (red). It can be clearly seen that for higher fields (>35 T), the correlation functions fall rapidly with distance and behave more and more like those of a pure Kitaev model, characterized by a spin liquid ground state.

6.4 Spin-spin correlation functions as evidence for a field-induced spin liquid state

We have computed the evolution of the spin correlation functions with distance for increasing magnetic-field values. The extent of decay of the correlation functions with distance reveals the presence or absence of long range correlations in the high field regime. The correlation functions $C_{ij} =< (\overrightarrow{\sigma_i} - < \overrightarrow{\sigma_i} >).(\overrightarrow{\sigma_j} - < \overrightarrow{\sigma_j} >) >$ are calculated for a chosen set of neighboring sites in our 24-site cluster and plotted in Fig. 6.11 as a function of $\frac{|i-j|}{a}$ (a being the distance between nearest neighbour sites) for different values of the applied field. We find that the decay of the correlation functions C_{ij} as a function of $\frac{|i-j|}{a}$ is much faster at relatively higher values of the applied field, and the amplitude of the oscillation of the correlation functions falls off rapidly with increasing fields, in particular above the zigzag ordering scale. Furthermore, structure factor calculations do not show a crossover from antiferromagnetic zigzag order to any of the known ordered states, considered by us, at the position of the metamagnetic transition manifested through the peak dip in the transverse magnetization. Indications therefore are that the high magnetic-field regime beyond the

peak-dip feature manifests spin-liquid physics in Na_2IrO_3. Our work sheds light on the universality of magnetic-field-induced quantum spin liquid physics in Kitaev systems, which we find to be signaled by the peak dip structure in the anisotropic magnetization at the zigzag ordering scale, also recently reported in $\alpha-RuCl_3$ [88], where no theoretical explanation for such features has been sought so far.

6.5 Summary

In summary, we have studied the high-field torque response of various effective spin models used in the literature to describe the behavior of the alkali Iridate Na_2IrO_3, known to be a Kitaev candidate, using large-scale exact diagonalization simulations. We have considered broadly three classes of models, and their variants: *Model A*, which is a nearest-neighbor model with a ferromagnetic Heisenberg and antiferromagnetic Kitaev interaction, *Model B*, which comprises a ferromagnetic Kitaev along with antiferromagnetic Heisenberg interactions up to the third neighbor, and *Model C*, which considers nearest-neighbor symmetric off-diagonal exchange interactions along with a ferromagnetic Kitaev and antiferromagnetic Heisenberg interactions. We have compared our results with experimental torque magnetometry measurements of Na_2IrO_3 for fields up to 60 T, which feature robust peak-dip features in the range 20-40 T for a range of orientations of the normal to the sample with the respect to the direction of the applied field. We have found that such features can only be reproduced by models with a ferromagnetic Kitaev interaction and not by their antiferromagnetic Kitaev counterparts. We have also shown that beyond the position of the peak-dip feature, the spin-spin correlation functions become increasingly short-ranged for higher field values, thus indicating the possibility of quantum spin liquid physics in this regime. Our results are consistent with the observation of a continuous spectrum of excitations [246, 74], as well as, possibly, a half-quantized thermal Hall conductivity [231] for field values exceeding the zigzag energy scale for $\alpha-RuCl_3$. We have illustrated the underlying universalities of the Kitaev materials Na_2IrO_3 and $\alpha-RuCl_3$, where a similar peak-dip feature has been observed recently.

PHASE COMPETITION AND CRITICAL BEHAVIOR IN THREE SPINLESS COUPLED LUTTINGER LIQUID SYSTEMS

Chapter 7

Competing phases and critical phenomena in three coupled spinless Luttinger liquid systems

7.1 Introduction

The problem of coupled one-dimensional systems of interacting fermions has received considerable attention in the literature, appearing in diverse contexts. These provide a testing ground for theoretical ideas developed for higher-dimensional systems, and a platform for realizing exotic phases of matter [266–269]. For models of interacting fermions in two spatial dimensions, it is usually a nontrivial task to ascertain phase diagrams of strongly correlated systems, due to the lack of accurate, systematic, nonperturbative methods. On the other hand, there are reliable nonperturbative methods available in one dimension such as bosonization [37] and the density matrix renormalization group (DMRG) method [270, 271]. Coupled-chain systems also provide a useful description for many naturally occuring compounds, such as carbon nanotubes [90], low-dimensional organic conductors [91], spin ladders [92, 272–274], quasi-1D superconductors (such as $K_2Cr_3As_3$ [94]), as well as artificially manufactured structures (such as self-assembled transition metal nanowires [95]). Many of these studies involve two-leg ladder systems [275–282].

In the literature, systems of two coupled CuO chains have been used extensively for gaining insight into the physics of copper oxide materials [280]. In particular, the importance of an explicit treatment of the oxygen atoms, for a better understanding of these materials, has been discussed, and ladder models have been studied for including the effect of oxygen atoms in such systems [283, 284]. The question of whether orbital currents could exist in

cuprate materials has also received much attention. Various intriguing phases of strongly correlated systems have been considered due to their possible relevance for understanding the pseudogap region in the phase diagram of the cuprates. One such possibility is the "orbital antiferromagnet," the "staggered flux" phase, or the "d-density wave" [285–288]. It is characterized by circulating currents which produce local magnetic moments aligned in an antiferromagnetic (staggered) way. The "circulating current" phase [20, 289], like the "staggered flux" phase, breaks time reversal symmetry and is characterized by circulating currents which produce local orbital magnetic moments, with the difference that it preserves translational symmetry while the "staggered flux" phase breaks it. There are also experimental examples of fermionic ladder materials, such as the "telephone number" compound $Sr_{14-x}Ca_xCu_{24}O_{41}$ [290], which display similarities and differences with the uniform cuprates. Besides, the question of whether the transverse correlations between two chains of interacting fermions are sustained by single-particle hopping or by pair hopping processes has interesting implications for high-temperature superconductivity [276, 291, 281].The instability of superconductivity for systems where a chemical potential difference is introduced between the legs of a two-leg ladder has been analyzed [292]. The effect of disorder for one-dimensional systems in the presence of interactions has also been explored [278].

The number of comparable studies on systems of three coupled Luttinger liquids have been limited, and here, spinful systems have been studied more extensively. These have proven useful for comparing the magnetic properties of systems composed of an even and an odd number of spin chains [92, 293, 93, 294], understanding the nature of instabilities in a three-band system using a Luttinger liquid framework with perturbations induced by residual interactions between the low-energy fermions (applicable in the case of cylindrical single-walled carbon nanotubes in the (5,0) configuration [90]) and in a one-dimensional three-orbital Hubbard model with generic repulsive electronic interactions (applicable for the quasi-1D superconductor $K_2Cr_3As_3$ [94]).

The common prescription for studying all these systems involves setting up scaling equations for the stiffness matrix $\widehat{K}$ in the quadratic part of the bosonized Hamiltonian (a sine-Gordon model), and the coupling constants in the sine-Gordon terms. One peculiarity of coupled Luttinger liquid systems that distinguishes them from single-phase Luttinger liquids is the fact that the renormalization process, even if performed to one-loop order, introduces corrections to all the matrix elements of $\widehat{K}$ in general, which must be taken into account in any renormalization group analysis. Unlike the diagonal corrections to the $\widehat{K}-$matrix, the off-diagonal corrections result in an interplay of the different interaction channels, even when the scaling of the coupling constants is considered only up to the leading tree-level order. Instead of solving the scaling equations for all the independent elements of $\widehat{K}-$matrix, a considerably

simpler strategy is to separate the effects of these corrections into two groups: large rotations of the $\widehat{K}-$matrix and small renormalizations of the eigenvalues of $\widehat{K}$. Of these two, only the latter affects the scaling dimensions of the interactions. In contrast, for the case of *two* identical spinless coupled Luttinger liquids, the problem decouples into two disconnected problems, respectively involving symmetric and antisymmetric combinations of the valley fields. Generically, in the absence of interaction between these channels, the renormalization procedure does not generate off-diagonal corrections to the stiffness matrix in this case. On the other hand, in the case of two spinful Luttinger liquids, generic interactions lead to appearance of off-diagonal corrections to $\widehat{K}$ during the scaling procedure, a point which was first noted in Ref. [283]. However, the simplest situation where such nontrivial rotations arise is the case of *three* spinless Luttinger liquids. In the literature, there have been studies of three coupled spinful Luttinger liquid systems, which suffer from the shortcoming that the aforementioned rotations are not accounted for. Motivated thus, in this part of the thesis, we perform a one-loop RG analysis for three coupled spinless Luttinger liquid systems by taking into account both the rotations of the $\widehat{K}-$matrices and the rescaling of their eigenvalues [295]. From the solutions of the scaling equations, we identify the most singular susceptibilities, corresponding to different order parameters, which in turn determines the phase diagram. Also, from a numerical study of the RG equations, we obtain the critical behavior near the phase transition points.

Our main findings are as follows. We find that the fixed point behavior is dependent both on the relative initial values of the coupling constants and the Luttinger liquid parameter, which is a qualitatively different situation from, say, the single-phase and two-phase sine-Gordon models, where the fixed-point behavior is completely independent of the initial conditions on the interactions. This is a direct consequence of the rotations of the stiffness matrices introduced in our approach. Depending upon the relative initial values of the couplings and the Luttinger parameters, we identify the different instabilities in the particle-particle and particle-hole channels and the nature of their transitions across phase boundaries. Further, we obtain the conditions under which valley symmetry breaking and intervalley orders may appear in both these channels. The possibility of chiral orders is also discussed in this context.

Our calculations may prove useful for understanding phase transitions and critical phenomena in the context of systems with multiple small Fermi pockets (like graphite intercalates [296, 297] and bismuth [45, 44, 298, 43, 299, 42, 300, 301, 41, 40, 39, 38, 302]) subject to quantizing magnetic fields, and cylindrical nanotubes at high fields. Our analysis is applicable for the study of competing phases in three coupled 1D systems where the instability occurs at energy scales much smaller than the chemical potential. However, in situations

where the instabilities appear at higher energy scales, other approaches such as the parquet renormalization group approach [57, 303, 58], discussed in Chapter-3, will be relevant.

7.2 Interacting model and bosonization

We consider generic density-density type of interactions, and expand the three spinless fermionic fields in the vicinity of the two Fermi points. We are interested in situations that physically correspond to partially filled bands, so that Umklapp scattering between the two Fermi points for a given band is not relevant. However, since we would like our model to be relevant for systems with multiple nested Fermi pockets with a nesting vector half a reciprocal lattice vector (such as in the case of bismuth), we do allow the possibility of two-particle Umklapp scattering between pockets, such that the total momentum transferred corresponds to a reciprocal lattice vector. With these assumptions, the interaction part of the Hamiltonian has the following form,

$$\begin{aligned}
H_{int} = \sum_{p,m} (& g_1^{(1)} \psi^\dagger_{pm} \psi^\dagger_{\overline{pm}} \psi_{pm} \psi_{\overline{pm}} + g_1^{(2)} \psi^\dagger_{pm} \psi^\dagger_{\overline{pm}} \psi_{\bar{p}m} \psi_{p\overline{m}} \\
& + g_1^{(3)} \psi^\dagger_{pm} \psi^\dagger_{p\overline{m}} \psi_{\bar{p}m} \psi_{\overline{pm}} + g_1^{(4)} \psi^\dagger_{pm} \psi^\dagger_{p\overline{m}} \psi_{pm} \psi_{p\overline{m}} \\
& + g_2^{(1)} \psi^\dagger_{pm} \psi^\dagger_{\overline{pm}} \psi_{p\overline{m}} \psi_{\bar{p}m} + g_2^{(2)} \psi^\dagger_{pm} \psi^\dagger_{\overline{pm}} \psi_{\overline{pm}} \psi_{pm} \\
& + g_2^{(3)} \psi^\dagger_{pm} \psi^\dagger_{p\overline{m}} \psi_{\overline{pm}} \psi_{\bar{p}m} + g_2^{(4)} \psi^\dagger_{pm} \psi^\dagger_{p\overline{m}} \psi_{p\overline{m}} \psi_{pm} \\
& + g_3^{(1)} \psi^\dagger_{pm} \psi^\dagger_{\bar{p}m} \psi_{p\overline{m}} \psi_{\overline{pm}} + g_3^{(2)} \psi^\dagger_{pm} \psi^\dagger_{\bar{p}m} \psi_{\overline{pm}} \psi_{p\overline{m}} \\
& + g_3^{(3)} \psi^\dagger_{pm} \psi^\dagger_{pm} \psi_{\overline{pm}} \psi_{\overline{pm}} + g_3^{(4)} \psi^\dagger_{pm} \psi^\dagger_{pm} \psi_{p\overline{m}} \psi_{p\overline{m}} \\
& + g_4^{(1)} \psi^\dagger_{pm} \psi^\dagger_{\bar{p}m} \psi_{pm} \psi_{\bar{p}m} + g_4^{(2)} \psi^\dagger_{pm} \psi^\dagger_{\bar{p}m} \psi_{\bar{p}m} \psi_{pm} \\
& + g_4^{(4)} \psi^\dagger_{pm} \psi^\dagger_{pm} \psi_{pm} \psi_{pm}),
\end{aligned} \tag{7.1}$$

where $p = 1(-1)$ refers to right (left) moving fermions, and $m = 0, 1, -1$ denotes the bands and $\overline{m} \neq m$. The three bands are regarded as identical, for simplicity. The above model is C_3 symmetric under permutation of bands. To study the low-energy behavior, we shall utilize the standard bosonization technique to analyze the continuum fermion model. We now bosonize the fermionic model using the abelian bosonization prescription-

$$\psi_{pm} = \frac{\eta_{pm}}{\sqrt{2\pi a}} \exp[ipk_{Fm}x] \exp[-ip\varphi_{pm}], \tag{7.2}$$

where k_{Fm} is the Fermi momentum for band m, a is a cutoff of the order of the lattice constant, and $p = 1(-1)$ stands for the $R(L)$ branch. We assume the Fermi momenta k_{Fm} for the three

bands to be identical. The Majorana Klein factors $\eta_{R/Lm}$ satisfy

$$\{\eta_{Rm}, \eta_{Rm'}\} = 2\delta_{mm'}$$

$$\{\eta_{Lm}, \eta_{Lm'}\} = 2\delta_{mm'}$$

$$\{\eta_{Rm}, \eta_{Lm'}\} = 0.$$

We adopt the following convention for the Klein factors, following Ref. [94],

$$\eta_{mp}\eta_{\overline{m}p} = \eta_{0p}\eta_{mp} = imp,$$

$$\eta_{mp}\eta_{m\overline{p}} = \eta_{0p}\eta_{0\overline{p}} = ip,$$

$$\eta_{mp}\eta_{\overline{mp}} = \eta_{0p}\eta_{m\overline{p}} = im,$$

where $p, m = \pm 1$. The chiral fields φ_{pm} can be written in terms of nonchiral fields ϕ_m and θ_m as $\varphi_{pm} = \phi_m - p\theta_m$, and their gradients are proportional to the fermionic density and current operators, respectively, i.e.

$$\begin{aligned} \nabla\phi_m &\propto \psi^\dagger_{Rm}\psi_{Rm} + \psi^\dagger_{Lm}\psi_{Lm} \\ \nabla\theta_m &\propto \psi^\dagger_{Rm}\psi_{Rm} - \psi^\dagger_{Lm}\psi_{Lm} \end{aligned} \tag{7.3}$$

We collect all quadratic terms together, which we henceforth call the "noninteracting" part. The rest consist of sine-Gordon terms (see below) that we denote as interactions.

We diagonalize the quadratic part of the Hamiltonian by transforming to new bosonic fields $\widetilde{\phi}$ given by

$$\begin{pmatrix} \phi_1 \\ \phi_{-1} \\ \phi_0 \end{pmatrix} = \begin{pmatrix} \frac{1}{\sqrt{2}} & \frac{1}{\sqrt{6}} & \frac{1}{\sqrt{3}} \\ -\frac{1}{\sqrt{2}} & \frac{1}{\sqrt{6}} & \frac{1}{\sqrt{3}} \\ 0 & -\frac{2}{\sqrt{6}} & \frac{1}{\sqrt{3}} \end{pmatrix} \begin{pmatrix} \widetilde{\phi}_1 \\ \widetilde{\phi}_{-1} \\ \widetilde{\phi}_0 \end{pmatrix}$$

and likewise for the fields θ_i. The "noninteracting" part of the Hamiltonian can be written as

$$H_0^B = \frac{1}{2\pi}\int dx \sum_\mu v_\mu (K_\mu (\nabla\widetilde{\phi_\mu})^2 + \frac{1}{K_\mu}(\nabla\widetilde{\theta_\mu})^2), \tag{7.4}$$

where $\mu = 0, 1, -1$. Note our convention for K_μ differs from the one commonly used in the literature, where K_μ^{-1} takes the place of K_μ. We have, for the bare couplings,

$$
\begin{aligned}
v_{\pm 1} K_{\pm 1} &= v_F - \frac{1}{2\pi}(G_2 - G_1) \equiv v_\perp K_\perp \\
v_0 K_0 &= v_F - \frac{1}{2\pi}(G_2^0 - G_1^0) \\
v_\perp &= \sqrt{(v_F - \frac{1}{2\pi}(G_2 - G_1))(v_F + \frac{1}{2\pi}(G_1 + G_2))} \\
K_\perp &= \sqrt{\frac{1 - \frac{1}{2\pi v_F}(G_2 - G_1)}{1 + \frac{1}{2\pi v_F}(G_1 + G_2)}} \\
v_0 &= \sqrt{(v_F - \frac{1}{2\pi}(G_2^0 - G_1^0))(v_F + \frac{1}{2\pi}(G_1^0 + G_2^0))} \\
K_0 &= \sqrt{\frac{1 - \frac{1}{2\pi v_F}(G_2^0 - G_1^0)}{1 + \frac{1}{2\pi v_F}(G_1^0 + G_2^0)}}
\end{aligned}
$$

where $G_1 = g_1^{(4)} - g_2^{(4)} - 2g_4^{(4)}$, $G_2 = -g_1^{(1)} + g_2^{(2)} + 2g_4^{(1)} - 2g_4^{(2)}$, $G_1^0 = -2g_1^{(4)} + 2g_2^{(4)} - 2g_4^{(4)}$ and $G_2^0 = 2g_1^{(1)} - 2g_2^{(2)} + 2g_4^{(1)} - 2g_4^{(2)}$. Note that the twofold degeneracy of the eigenvalues of the stiffness matrix $\widehat{K}$ is a consequence of the C_3 rotational symmetry of the quadratic part of the Hamiltonian. Following the strategy of Ref. [89], we study the scaling of the quantities $K_{0,\perp}^\phi = \frac{v_{0,\perp} K_{0,\perp}}{\pi}$ and $K_{0,\perp}^\theta = \frac{v_{0,\perp}}{\pi K_{0,\perp}}$, assuming an initial condition $v_{0,\pm 1} = \pi$. We now define new rescaled fields $\widetilde{\psi}_{0,\pm 1} = \sqrt{K_{0,\perp}^\phi}\widetilde{\phi}_{0,\pm 1}$ and $\widetilde{\varphi}_{0,\pm 1} = \sqrt{K_{0,\perp}^\theta}\widetilde{\theta}_{0,\pm 1}$. Such a rescaling makes the stiffness matrix proportional to the identity matrix. During the RG process, small diagonal and off-diagonal corrections are introduced to the stiffness matrix, and it has a real symmetric form that we denote by $Z_{\mu\nu}$. After bosonization, the interacting part of the Hamiltonian has the form of coupled sine-Gordon terms

$$
H_{int}^B = \sum_\alpha g_\alpha \cos(a_i^{(\alpha)} \widetilde{\psi}_i) + \sum_\beta g_\beta \cos(A_i^{(\beta)} \widetilde{\varphi}_i) \tag{7.5}
$$

where $\alpha = 1-3, 7-9$ and $\beta = 4-6$, and the coefficients,

$$
\begin{aligned}
a^{(1)} &= \left(\frac{2\sqrt{2}}{\sqrt{K_\perp^\phi}}, \;\; 0, \;\; 0 \right), \\
a^{(2)} &= \left(\frac{\sqrt{2}}{\sqrt{K_\perp^\phi}}, \;\; \frac{\sqrt{6}}{\sqrt{K_\perp^\phi}}, \;\; 0 \right), \\
a^{(3)} &= \left(\frac{\sqrt{2}}{\sqrt{K_\perp^\phi}}, \;\; -\frac{\sqrt{6}}{\sqrt{K_\perp^\phi}}, \;\; 0 \right), \\
a^{(7)} &= \left(0, \;\; \frac{4}{\sqrt{6}\sqrt{K_\perp^\phi}} \;\; \frac{4}{\sqrt{3}\sqrt{K_0^\phi}} \right), \\
a^{(8)} &= \left(\frac{\sqrt{2}}{\sqrt{K_\perp^\phi}}, \;\; \frac{2}{\sqrt{6}\sqrt{K_\perp^\phi}}, \;\; -\frac{4}{\sqrt{3}\sqrt{K_0^\phi}} \right), \\
a^{(9)} &= \left(\frac{\sqrt{2}}{\sqrt{K_\perp^\phi}}, \;\; -\frac{2}{\sqrt{6}\sqrt{K_\perp^\phi}}, \;\; \frac{4}{\sqrt{3}\sqrt{K_0^\phi}} \right), \\
A^{(4)} &= \left(\frac{2\sqrt{2}}{\sqrt{K_\perp^\theta}}, \;\; 0, \;\; 0 \right), \\
A^{(5)} &= \left(\frac{\sqrt{2}}{\sqrt{K_\perp^\theta}}, \;\; \frac{\sqrt{6}}{\sqrt{K_\perp^\theta}}, \;\; 0 \right), \\
A^{(6)} &= \left(\frac{\sqrt{2}}{\sqrt{K_\perp^\theta}}, \;\; -\frac{\sqrt{6}}{\sqrt{K_\perp^\theta}}, \;\; 0 \right),
\end{aligned}
$$

where the effective couplings $g_\alpha (\alpha = 1-8)$ are linear combinations of the couplings $g_i^{(j)}$. Note that we allow the possibility of the coupling constants in the sine-Gordon model to break the C_3 permutation symmetry in the following analysis. The same can also be done in the quadratic part. However, introducing C_3 symmetry breaking in any of these sine-Gordon channels ultimately results in lifting of C_3 symmetry in the quadratic part, as we shall see, and so there is no loss of generality. During the RG procedure, the vectors $\widehat{a}$ and $\widehat{A}$, in general, rotate and stretch. We find that the scaling dimensions for the interaction terms in Eq. 7.5 depend on the values of the Luttinger parameters $K_0^{\phi,\theta}$ and $K_\perp^{\phi,\theta}$, and in our analysis, we only retain the most relevant interaction terms (smallest scaling dimensions). This further reduces the number of parameters we need to consider in our model.

7.3 Renormalization group analysis

The renormalization group follows the standard Wilsonian procedure of elimination of fast degrees of freedom, restoration of the cutoff, rescaling of the couplings and the renormalization of the fields. This makes the stiffness matrices differ from unity due to off-diagonal corrections, i.e. they take the form $Z_{\mu\nu}$. To keep the Gaussian fixed point unchanged, we

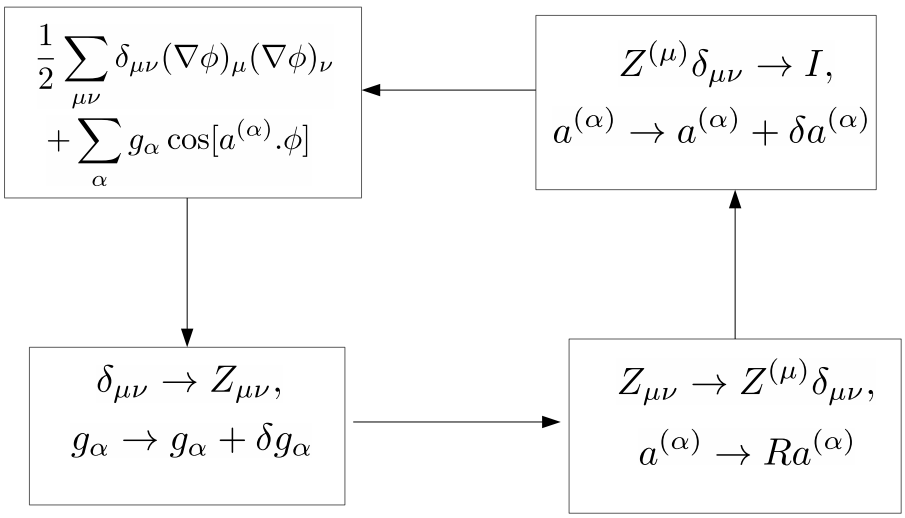

Fig. 7.1 The figure shows a schematic illustration of our renormalization group procedure. The stiffness matrix, which is initially diagonal, develops off-diagonal corrections in the course of the RG flow and takes the general form $Z_{\mu\nu}$. This matrix is diagonalized, which leads to a rotation R of the coefficients $a^{(\alpha)}$ of the sine-Gordon interaction terms. The diagonal elements are then absorbed in the respective sine-Gordon fields, which brings the stiffness matrix back to unity, and leads to a rescaling of the rotated coefficients $a^{(\alpha)}$.

need to rotate the $Z^{\theta,\phi}_{\mu\nu}$ matrices to diagonalize them and then rescale the fields such that they become proportional to identity matrices. Note that the above rotation does not change the scaling dimensions of the interaction terms. Now, in the new basis obtained after rotation and rescaling of the fields, we can once again compute the one-loop corrections and the resulting changes in the diagonal and off-diagonal elements, and repeat the aforementioned steps throughout the RG process. A completely equivalent procedure has been followed in Ref. [89], where, instead of keeping the Gaussian fixed point unchanged, the fields are kept unchanged and the renormalization process leads to rotations and stretching of eigenvalues of the $Z^{\theta,\phi}_{\mu\nu}$ matrices. At this point, the number of parameters in the model is still large, and we simplify our analysis by considering the anisotropic limits $K^{\phi}_{\perp} \gg K^{\phi}_{0}$ or $K^{\phi}_{0} \gg K^{\phi}_{\perp}$, which allows us to drop certain terms in the interacting Hamiltonian in Eq. 7.5 with higher scaling dimensions. However, we emphasize that the formulation may be readily extended to the general case. Below we discuss the results obtained by incorporating one-loop corrections to the matrices $Z^{\phi}_{\mu\nu}$ and $Z^{\theta}_{\mu\nu}$ in the two aforementioned parameter regimes. The details of the calculations are discussed in Appendix-D. At any given stage of the RG, the matrix $Z^{\phi}_{\mu\nu}$, with the one-loop corrections incorporated, is given by

$$Z^{\phi} = \begin{pmatrix} \frac{1}{2} + \sum_{\alpha} \frac{g_{\alpha}^2 dy}{16\pi}((a_1^{(\alpha)})^2 + (a_{-1}^{(\alpha)})^2)(a_1^{(\alpha)})^2 & \sum_{\alpha} \frac{g_{\alpha}^2 dy}{16\pi}((a_1^{(\alpha)})^2 + (a_{-1}^{(\alpha)})^2)(a_1^{(\alpha)})(a_{-1}^{(\alpha)}) & 0 \\ \sum_{\alpha} \frac{g_{\alpha}^2 dy}{16\pi}((a_1^{(\alpha)})^2 + (a_{-1}^{(\alpha)})^2)(a_1^{(\alpha)})(a_{-1}^{(\alpha)}) & \frac{1}{2} + \sum_{\alpha} \frac{g_{\alpha}^2 dy}{16\pi}((a_1^{(\alpha)})^2 + (a_{-1}^{(\alpha)})^2)(a_{-1}^{(\alpha)})^2 & 0 \\ 0 & 0 & \frac{1}{2} \end{pmatrix}. \tag{7.6}$$

Note that the above matrix is block-diagonal - a consequence of the nature of the interaction terms and/or approximations employed in the parameter regimes considered in our analysis. While the corrections accumulated are infinitesimal, the rotations involved in restoring the matrices with off-diagonal contributions are finite rotations which cannot be accounted for in the RG flow equations. In our approach, we are always in the rotating frame, where these large rotations are absent, and only small incremental changes to the components along the field directions need to be tracked. These amount to slow changes in the orientation and length, in the rotating frame, upon scaling. In the limit where $K^{\phi}_{0} \ll K^{\phi}_{\perp}$, we find that we only need to retain the couplings $g_{\alpha}(\alpha = 1-3)$, based on their lower scaling dimensions. In this case, we calculate one-loop corrections to the Z^{ϕ} matrices due to the terms g_1, g_2 and g_3 in the interaction Hamiltonian, and likewise, to the Z^{θ} matrices due to the terms g_4,g_5 and g_6. The corresponding matrix turns out to be block-diagonal due to the symmetry of the interaction terms in this regime. On the other hand, in the limit where $K^{\phi}_{\perp} \ll K^{\phi}_{0}$, only the couplings $g_{\alpha}(\alpha = 7-9)$ need to be retained for our analysis. Here we

obtain one-loop corrections to the Z^{ϕ} matrices arising from the couplings g_7, g_8 and g_9, and, once again, to the Z^{θ} matrices due to the terms g_4,g_5 and g_6. In this case, the matrix Z^{ϕ} is generally a dense matrix which comprises nonzero corrections to every matrix element. However, implementing the limit $K_{\perp}^{\phi} \ll K_0^{\phi}$, we can drop certain terms and it reduces to a block-diagonal form similar to Eq. 7.6 above with $\alpha = 7-9$.

We denote the eigenvalues of the matrices in the Eq. 7.6 above by z_1, z_{-1} and z_0. We diagonalize the stiffness matrix and rescale the fields using these eigenvalues. At any given stage of the RG flow, the coefficients of the cosine terms in the interaction Hamiltonian evolve in the manner $a_i^{(\alpha)} \to \frac{(Ra^{(\alpha)})_i}{\sqrt{z_i}}$, where R is the rotation which diagonalizes the matrix $Z_{\mu\nu}$. We continue to denote the interaction terms as $g_\alpha \cos[\widehat{a}_i^{(\alpha)} \widetilde{\psi}_i]$ or $g_\alpha \cos[\widehat{A}_i^{(\alpha)} \widetilde{\varphi}_i]$. Proceeding in incremental steps, the RG equations for $a_1^{(1)}$ and $a_{-1}^{(1)}$, due to the rescaling process, are given by

$$\begin{aligned} \frac{da_1^{(1)}}{dy} &= -a_1^{(1)} \alpha_1 \\ \frac{da_{-1}^{(1)}}{dy} &= -a_{-1}^{(1)} \alpha_{-1} \end{aligned} \tag{7.7}$$

where $z_1 = 1/2 + \alpha_1 dy$ and $z_{-1} = 1/2 + \alpha_{-1} dy$, and α_1 and α_{-1} depend upon all the couplings as well as the coefficients of all the fields in the sine-Gordon terms. The RG flow equations for the rest of the components $a_i^{(\alpha)}$ are similarly obtained. The tree-level contributions to the RG flows for the couplings g_α may be obtained in terms of their respective scaling dimensions. In our analysis, we do not calculate the one-loop corrections to the renormalization of the coupling constants g_α, as they are a higher-order contribution in the small coupling constants. As an illustrative example, the RG equations for the couplings $g_\alpha, \alpha = 1-3$ are given by

$$\begin{aligned} \frac{dg_1}{dy} &= \left(2 - \frac{1}{4\pi}((a_1^{(1)})^2 + (a_{-1}^{(1)})^2)\right) g_1 \\ \frac{dg_2}{dy} &= \left(2 - \frac{1}{4\pi}((a_1^{(2)})^2 + (a_{-1}^{(2)})^2)\right) g_2 \\ \frac{dg_3}{dy} &= \left(2 - \frac{1}{4\pi}((a_1^{(3)})^2 + (a_{-1}^{(3)})^2)\right) g_3 \end{aligned} \tag{7.8}$$

Similar arguments are used to determine the RG equations for the rest of the couplings $g_\alpha (\alpha = 4-9)$. We solve these coupled differential equations numerically and obtain the fixed-point values for the couplings g_α and the coefficients $a_i^{(\alpha)}$. We consider weak repulsive interactions in every channel, and study the nature of the RG flows as a function of the

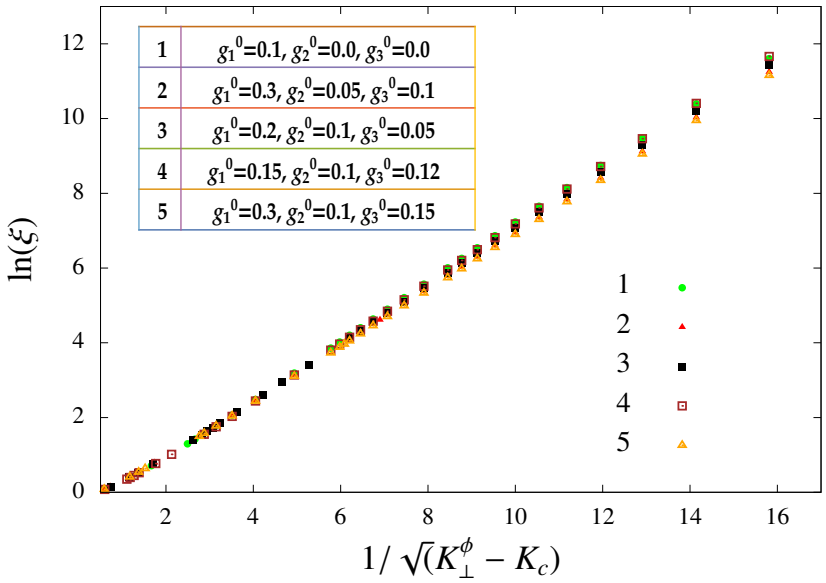

Fig. 7.2 The figure shows a scaling collapse plot of the RG flow parameter $y \sim \ln[\xi]$ (where ξ is the correlation length) as a function of $\frac{1}{\sqrt{K_\perp^\phi - K_c}}$. K_c denotes the critical value of the Luttinger liquid parameter $K_\perp^\phi$, where the system undergoes a phase transition. The plot shows results for five different sets of initial conditions on the interactions, with one or more of the couplings g_α taking non-zero values initially, and indicates that the phase transitions occuring in this system are continuous in nature and belong to the BKT universality class.

initial conditions on the interactions and the value of the Luttinger liquid parameter $K_\perp^{\phi,\theta}$. In general, we find that the couplings g_α either diverge or flow to zero in the course of the RG flow. From Eq. 7.7 above, it is clear that the coefficients $a_1^{(\alpha)}$ and $a_{-1}^{(\alpha)}$ obey different RG equations , and show qualitatively different behavior as a function of the RG flow parameter. While the coefficient $a_1^{(\alpha)}$ always decreases in the course of the RG procedure, $a_{-1}^{(\alpha)}$ may increase or decrease, depending upon the initial conditions considered for the interactions. In other words, the coefficients of the different fields rescale differently in the course of the RG flow, following the rotation of the stiffness matrix.

7.4 Order parameters and phase diagram

The order parameters considered in our analysis are fermionic bilinear operators characterized by chirality and band indices. There are two classes of order parameters in our system. These are defined in the particle-hole channels where we follow the convention used by Ref. [94],

$$\mathrm{Re}[O_{ph}^i] = \sum_{mm'} \lambda_{mm'}^i \psi_{Rm}^\dagger \psi_{Lm'} + \mathrm{h.c} \tag{7.9}$$

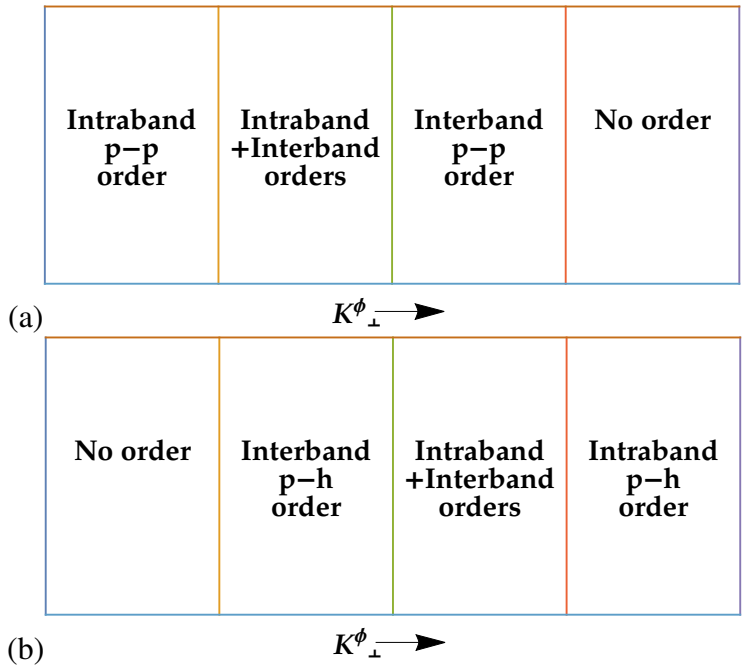

Fig. 7.3 The figure shows the phase diagram of a system of three coupled spinless Luttinger liquids, for the parameter regimes (a) $K^{\phi}_{\perp} \gg K^{\phi}_{0}$ and $K^{\phi}_{0} \ll 1$, where only particle-particle (p-p) orders are considered due to the smaller scaling dimensions for the corresponding terms, and (b) $K^{\phi}_{0} \gg K^{\phi}_{\perp}$ and $K^{\phi}_{0} \gg 1$, where only particle-hole (p-h) orders are considered in our analysis. In both cases, we can tune $K^{\phi}_{\perp}$ and for values of $K^{\phi}_{\perp} \sim 1$, various interband and intraband orders compete with one another, with the winner being determined by the initial conditions on the interactions.

where $\lambda^i (i = 1...8)$ correspond to the Gell-Mann matrices (see Appendix-D for details), λ^0 denotes the 3x3 unit matrix, ψ_{pm} ($\psi^\dagger_{pm}$) is the electron annihilation (creation) operator with chirality p and band m, and in the particle-particle channels,

$$\mathrm{Re}[O^i_{pp}] = \sum_{mm'} \lambda^i_{mm'} \psi^\dagger_{Rm} \psi^\dagger_{Lm'} + \mathrm{h.c} \tag{7.10}$$

where, in both the Eqs. 7.9 and 7.10, no spin indices are considered due to the spinless nature of the fermions. Note that we consider ordered states arising from scattering or pairing in opposite chiralities in this analysis, and we have checked that equal-chirality interband pairing terms show a qualitatively similar behavior. The order parameters in Eqs. 7.9 and 7.10 above are now expressed in terms of the bosonic fields. A total of sixteen order parameters are obtained in the particle-hole and particle-particle channels for the spinless case (see Appendix-D). The dominant order parameters are determined by introducing small order parameter fluctuations and considering how it evolves under RG. The corresponding RG equations are listed in Appendix-D. At the tree level, the dominant order parameters are those that have the smallest scaling dimensions. In order to determine the winning order parameters, we consider the behavior of the couplings g_α and the corresponding rotation parameters $a_i^{(\alpha)}$ near the critical point for a given set of initial conditions and find that both quantities play a crucial role in deciding the nature of the dominant electronic orders. In some cases, we find that none of the order parameters we studied grows under RG, implying the absence of any long-range order despite the presence of interactions.

We have two broad classes based on the relative sizes of K_0^ϕ and $K_\perp^\phi$ and within each of these two classes, we further have two situations corresponding to $K_0^\phi \gg 1$ or $K_0^\phi \ll 1$. The case of $K_0^\phi \sim 1$ has not been considered in this work and will be taken up later. In the regime where $K_0^\phi \gg K_\perp^\phi$ and $K_0^\phi \ll 1$, the dominant instabilities are found in the intraband particle-particle channel. Similarly, in the regime where $K_\perp^\phi \gg K_0^\phi$ and $K_0^\phi \gg 1$, the dominant instabilities are found in the intraband particle-hole channel. We now consider the remaining two cases, which allow us to tune $K_\perp^\phi$ over a large range, and involve both intraband and interband orders.

We find that for $K_0^\phi \gg K_\perp^\phi$ and $K_0^\phi \gg 1$, the particle-hole orders are more relevant due to smaller scaling dimensions of the corresponding terms, whereas for $K_\perp^\phi \gg K_0^\phi$ and $K_0^\phi \ll 1$, the particle-particle orders are found to be more relevant. Using a numerical scaling analysis, we have studied the nature of the phase transitions in this system, and find that the phase diagram is affected primarily by two factors: the magnitude of the Luttinger liquid parameter $K_\perp^\phi$ and the set of initial conditions considered for the interactions g_α. The scaling of the correlation length ξ at the critical point is determined by identifying the characteristic scale

y where the couplings $g_\alpha(y)$ cross a designated value $\gtrsim 1$. We obtain continuous transitions as a function of $K_\perp^\phi$, which belong to the Berezinskii-Kosterlitz-Thouless (BKT) universality class. To confirm this, we have demonstrated universal BKT scaling collapse for the behavior of the correlation length close to the critical point (see Fig. 7.2). Note that the critical value K_c of the Luttinger parameter $K_\perp^\phi$ is different for different initial conditions on the couplings g_α but give rise to the same critical behavior.

Below we discuss the salient features of the phase diagram, considering various parameter regimes for $K_\perp^\phi$, each of which correspond to two further regimes, $K_0^\phi \gg K_\perp^\phi$ and $K_0^\phi \gg 1$ or $K_0^\phi \ll K_\perp^\phi$and $K_0^\phi \ll 1$. Since $K_\perp^\theta$ is inversely related to $K_\perp^\phi$ in our model, it does not constitute an independent parameter in the phase diagram.

$K_\perp^\phi \ll 1$: In this regime, for $K_0^\phi \ll K_\perp^\phi$ and $K_0^\phi \ll 1$, the intraband particle-particle orders are found to be dominant, whereas if $K_0^\phi \gg K_\perp^\phi$ and $K_0^\phi \gg 1$, initially no electronic orders are present for extremely small values of $K_\perp^\phi$, and for larger values of $K_\perp^\phi$, a particular pair of interband particle-hole orders dominates, depending upon the initial conditions being considered for the interactions.

$K_\perp^\phi \sim 1$: In the regime $K_\perp^\phi \sim 1$, in both the regimes $K_0^\phi \ll K_\perp^\phi$ and $K_0^\phi \ll 1$, and $K_0^\phi \gg K_\perp^\phi$ and $K_0^\phi \gg 1$, various intraband and interband particle-particle and particle-hole orders compete with each other, and the winners are dependent most sensitively on the initial conditions chosen for the interactions in this part of the phase diagram.

$K_\perp^\phi \gg 1$: In this regime, for $K_0^\phi \ll K_\perp^\phi$ and $K_0^\phi \ll 1$, a particular pair of interband particle-particle orders is found to be dominant, depending upon the initial conditions chosen for the interactions, and no order is present at extremely large values of $K_\perp^\phi$, whereas if $K_0^\phi \gg K_\perp^\phi$ and $K_0^\phi \gg 1$, then the intraband particle-hole orders are found to dominate.

The various electronic orders found to occur in the different parameter regimes considered by us are schematically shown in Fig. 7.3.

7.5 Summary

In summary, we have studied competing electronic phases and phase transitions in a system of three coupled spinless Luttinger liquids using a renormalization group analysis of the bosonized model, that takes into account one-loop corrections to the stiffness matrix, generating off-diagonal contributions. In order to restore these matrices to a form that is proportional to an identity matrix, we introduce a series of rotations and then rescale the fields at each

step of the RG flow. These rotations and rescalings are found to couple different interaction channels even at the tree-level order. The coefficients of different fields in a given interaction term rescale differently. The results of the RG flows are found to be sensitive to the relative initial values of the interaction couplings g_α, a feature absent in single-phase and two-phase sine-Gordon models. We have also studied competing orders in the particle-particle and particle-hole channels using the renormalization group, which are sixteen in number for the spinless case. In the regimes considered, we find that for extreme values of the Luttinger liquid parameter $K_\perp^\phi$, interband and intraband orders which involve one of the three bands, or a particular pair of bands, are found to dominate, depending upon the initial conditions for the couplings, which leads to valley symmetry breaking, and the intraband orders realized are chiral. In the regime where $K_\perp^\phi \sim 1$, the dominant orders are found to be strongly sensitive to the initial values of the interaction couplings. For simplicity, we have considered the regimes of $K_0^\phi \gg 1$ or $K_0^\phi \ll 1$, and the case of $K_0^\phi \sim 1$ has not been considered here. In the latter regime, the particle-particle and particle-hole channels compete with each other and the results are likely to be sensitive to the initial conditions considered. This will be taken up in a future work. We determine the nature of the phase transitions as a function of the Luttinger parameter $K_\perp^\phi$ as well as the initial conditions on the interactions g_α using a numerical scaling analysis, and obtain continuous transitions belonging to the BKT universality class. We expect our analysis to be applicable to systems with three Fermi pockets, such as bismuth and graphite intercalation compounds, in the presence of a large magnetic field, where each of the electron pockets effectively behaves like a one-dimensional system.

Chapter 8

Summary

In summary, we have explored strongly spin-orbit coupled systems in the regimes of both weak and strong electronic correlations, and find that a variety of interesting phases can be realized either by tuning the electron correlations or an external parameter such as an applied magnetic field. In the case of the topological crystalline insulator $Pb_{1-x}Sn_xTe$ as well as multipocket systems at high fields, such as the one discussed in the last part of the thesis, weak electron correlations are shown to result in electronic states that break valley degeneracy, including chiral orders. In the spin-orbit assisted Mott insulator Na_2IrO_3, we found that a magnetic field may be used to tune the system from a magnetically ordered ground state to a quantum spin liquid state with short-range spin correlations. Below, I summarize the main findings of the three research projects that have been discussed in this thesis.

8.1 Electronic instabilities on a topological crystalline insulator surface

In the first part of the thesis, we have studied electronic phase competition on the (001) surface of the topological crystalline insulator $Pb_{1-x}Sn_xTe$ using a parquet renormalization group analysis, which takes into account competing instabilities in the particle-particle and particle-hole channels. We found that over a wide range of parameter space of the repulsive interactions considered, the dominant electronic order in this system is chiral $p-$wave superconductivity. Here, the chiral nature of the superconducting order arises from the Berry phases associated with the surface states, and is topologically protected against weak disorder, unlike in the case of Sr_2RuO_4. We further studied the effect of an external magnetization on the chiral $p-$wave superconductivity and found that the electronic order on the surface is

protected by multiorbital effects in this system, i.e. for a finite value of Hund's splitting, there is a critical value of the external magnetization beyond which the chiral $p-$wave order is no longer stable. On the experimental front, recent point-contact spectroscopy measurements have confirmed the existence of superconductivity on the (001) surface of this material, but the nature of the superconducting order remains to be ascertained. While scanning tunneling measurements provide a possible avenue for detecting unconventional superconductivity, zero-bias peaks in STM measurements may not necessarily indicate the presence of Majorana zero modes. In this connection, in the third part of the project, we have proposed a simple approach, using impurity-induced Shiba-like subgap states, for unambiguously identifying the nature of the superconducting order. We have shown that if chiral $p-$wave superconductivity is indeed present, then subgap bound states in only certain parameter regimes of doping depend crucially upon it. We have obtained exact analytical expressions for the bound state spectra and wavefunctions, as a function of the parameters of the system, and identified the properties of such states that can be associated with the nature of the superconducting order. From an experimental point of view, $Pb_{1-x}Sn_xTe$ provides a natural setting for realizing such a state, owing to the presence of low-lying Van Hove singularities and effectively spinless surface bands. If realized, this would be a rare example of a system with intrinsic chiral $p-$wave superconductivity, in contrast to the proximity-induced superconducting order in topological insulator heterostructures.

8.2 High-field torque response of the alkali Iridate Na_2IrO_3: Evidence for strong ferromagnetic Kitaev correlations and possibility of a field-induced spin liquid

In the second part of the thesis, we have combined high-field torque magnetometry measurements (up to 60 T) for the alkali iridate Na_2IrO_3, a popular Kitaev material, with large-scale exact diagonalization simulations, to probe the underlying interactions in this material. We calculated the magnetoresponse for effective spin models with a dominant Kitaev term, along with subdominant isotropic and anisotropic off-diagonal exchange interactions, and found that a robust characteristic peak-dip feature in the experimental torque response, observed in the field range of 20-40 T, can only be reproduced for models with a large ferromagnetic Kitaev interaction, and not for their antiferromagnetic Kitaev counterparts. We further calculated spin-spin correlations as a function of distance on the hexagonal cluster for various values of the applied field, and found that beyond the position of the peak-dip feature, the spin correlations become increasingly short-ranged for larger field values. Furthermore, structure

factor calculations do not show a crossover from an antiferromagnetic zigzag order to any of the commonly encountered magnetically ordered states at the position of the peak dip in the transverse magnetization. Indications therefore are that the high magnetic-field regime beyond the peak-dip feature manifests spin-liquid physics in Na_2IrO_3. Our work sheds light on the universality of magnetic-field-induced quantum spin liquid physics in Kitaev systems, which we find to be signaled by the peak dip structure in the anisotropic magnetization at the zigzag ordering scale, also recently reported in $\alpha-RuCl_3$, another Kitaev material that has attracted a lot of attention. Such a feature thus serves as an independent experimental handle that can provide valuable information about the nature of the magnetic interactions as well as, possibly, signal the onset of a field-induced spin liquid phase. The microscopic models that we use for our calculations are indicated to be relevant to a broad class of spin-orbit coupled honeycomb Kitaev materials including $\alpha-RuCl_3$. Our results are consistent with recent thermal Hall conductivity and inelastic neutron scattering experiments in $\alpha-RuCl_3$, which point towards the possibility of accessing Kitaev physics at high fields beyond the zigzag ordering scale of these materials. The short-range correlated phase at high fields obtained for models which reproduce the qualitative features of the experimental torque response strongly emphasize the importance of this regime for realizing a spin-liquid phase.

8.3 Competing phases and critical phenomena in a system of three coupled spinless Luttinger liquids

In the third part of the thesis, we have studied competing electronic phases and phase transitions in a system of three coupled spinless Luttinger liquids using a renormalization group (RG) analysis of the bosonized interactions. Our RG procedure takes into account one-loop corrections to the stiffness matrices, generating off-diagonal contributions. In order to keep the Gaussian fixed point invariant, we introduce a series of rotations and then rescale the fields at each step of the RG flow, or equivalently, the coefficients of different fields in the sine-Gordon interaction terms. These rotations and rescalings are found to be dependent on all the couplings as well as coefficients of all the fields, and couple different interaction channels even at the tree-level order. Moreover, we find that the coefficients of different fields in a given interaction term rescale differently. The RG flows are found to be sensitive to the initial values of the interaction couplings g_α, a feature absent in single-phase and two-phase sine-Gordon models. We also study the response to fluctuations to the order parameters in the particle-particle and particle-hole channels using the renormalization group, to determine the most dominant electronic orders. We find that the overall nature of the winning orders in

different parameter regimes is governed by the RG flow equations for the couplings as well as the coefficients of the fields in the sine-Gordon terms. In particular, for extreme values of the Luttinger liquid parameter $K_\perp^\phi$, interband and intraband orders which involve one of the three bands, or a particular pair of bands, are found to dominate, depending upon the initial conditions for the couplings, which is a manifestation of valley symmetry breaking. The intraband orders realized are generically chiral. In the regime where $K_\perp^\phi \sim 1$, the dominant orders are found to be strongly sensitive to the initial values of the interaction couplings. For simplicity in the analysis of the dominant electronic orders, we have considered the regimes of $K_0^\phi \gg 1$ or $K_0^\phi \ll 1$ in our analysis, and the case of $K_0^\phi \sim 1$ has not been considered in this work. In such a regime, the particle-particle and particle-hole channels will compete with each other and the results are likely to be sensitive to the initial conditions considered. This will be taken up in a future work. We determine the nature of the phase transitions as a function of the Luttinger parameter $K_\perp^\phi$ as well as the initial conditions on the interactions g_α using a numerical scaling analysis, and obtain continuous transitions belonging to the BKT universality class. While the critical value of $K_\perp^\phi$ is different for different initial values of the couplings, the nature of the phase transitions is found to be independent of this. Our analysis is expected to be applicable for strongly spin-orbit coupled systems with three Fermi pockets, such as bismuth, at high magnetic fields. We have not studied the case where $K_0^\phi \sim K_\perp^\phi$, with the rotations being in general O(3) matrices. The rotation matrices in that case are non-abelian and it would interesting to see if this gives qualitatively new insights into the problem. A similar analysis should also be performed for the case of three spinful coupled Luttinger liquids (which are useful for describing quasi-one dimensional systems such as $K_2Cr_3As_3$), taking into account special fillings where intraband Umklapp scattering terms are possible.

References

[1] A. S. Edelstein, J. Magn. Magn. Mater. **256**, 430 (2003).

[2] F. Ronning and C. Batista, J. Phys. Condens. Matter **23**, 090201 (2011).

[3] T. Moriya, "Local magnetic moments," in *Spin Fluctuations in Itinerant Electron Magnetism* (Springer Berlin Heidelberg, Berlin, Heidelberg, 1985) pp. 109–128.

[4] T. Moriya, Phys. Rev. **120**, 91 (1960).

[5] L. Savary and L. Balents, Rep. Prog. Phys. **80**, 016502 (2016).

[6] J. Knolle and R. Moessner, Annu. Rev. Condens. Matter Phys. **10**, 451 (2019).

[7] A. G. Green, G. Conduit, and F. Krüger, Annu. Rev. Condens. Matter Phys. **9**, 59 (2018).

[8] K. Miyake and Y. Kuramoto, Physica B: Condensed Matter **171**, 20 (1991).

[9] S. Sachdev, Science **288**, 475 (2000).

[10] P. Coleman, Nature **433**, 226 (2005).

[11] M. R. Norman, Science **332**, 196 (2011).

[12] M. Sigrist and K. Ueda, Rev. Mod. Phys. **63**, 239 (1991).

[13] P. F. Chester, Rep. Prog. Phys. **30**, 561 (1967).

[14] Z. J. J. Stekly, J. Appl. Phys. **42**, 65 (1971).

[15] G. Brassard, I. Chuang, S. Lloyd, and C. Monroe, Proceedings of the National Academy of Sciences **95**, 11032 (1998).

[16] S. D. Sarma, M. Freedman, and C. Nayak, Npj Quantum Information **1**, 15001 (2015).

[17] A. Steane, Rep. Prog. Phys. **61**, 117 (1998).

[18] G. Jackeli and G. Khaliullin, Phys. Rev. Lett. **102**, 017205 (2009).

[19] E.-G. Moon, C. Xu, Y. B. Kim, and L. Balents, Phys. Rev. Lett. **111**, 206401 (2013).

[20] S. Schmitt, N. Grewe, and T. Jabben, Phys. Rev. B **85** (2011).

[21] J. G. Rau, E. K.-H. Lee, and H.-Y. Kee, Annu. Rev. Condens. Matter Phys. **7**, 195 (2016).

[22] W. Witczak-Krempa, G. Chen, Y. B. Kim, and L. Balents, Annual Review of Condensed Matter Physics **5**, 57 (2014).

[23] N. F. Mott, Rev. Mod. Phys. **40**, 677 (1968).

[24] C. L. Kane and E. J. Mele, Phys. Rev. Lett. **95**, 146802 (2005).

[25] C. Kane and J. Moore, Physics World **24**, 32 (2011).

[26] J. E. Moore, Nature **464**, 194 (2010).

[27] O. Vafek and A. Vishwanath, Annu. Rev. Condens. Matter Phys. **5**, 83 (2014).

[28] N. P. Armitage, E. J. Mele, and A. Vishwanath, Rev. Mod. Phys. **90**, 015001 (2018).

[29] Y. L. Chen, J. G. Analytis, J.-H. Chu, Z. K. Liu, S.-K. Mo, X. L. Qi, H. J. Zhang, D. H. Lu, X. Dai, Z. Fang, S. C. Zhang, I. R. Fisher, Z. Hussain, and Z.-X. Shen, Science **325**, 178 (2009).

[30] D. Hsieh, Y. Xia, L. Wray, D. Qian, A. Pal, J. H. Dil, J. Osterwalder, F. Meier, G. Bihlmayer, C. L. Kane, Y. S. Hor, R. J. Cava, and M. Hasan, Science **323**, 919 (2009).

[31] T. Hanaguri, K. Igarashi, M. Kawamura, H. Takagi, and T. Sasagawa, Phys. Rev. B **82**, 081305 (2010).

[32] D. Hsieh, Y. Xia, D. Qian, L. Wray, F. Meier, J. H. Dil, J. Osterwalder, L. Patthey, A. V. Fedorov, H. Lin, A. Bansil, D. Grauer, Y. S. Hor, R. J. Cava, and M. Z. Hasan, Phys. Rev. Lett. **103**, 146401 (2009).

[33] M. R. Norman and C. Pépin, Rep. Prog. Phys. **66**, 1547 (2003).

[34] M. B. Salamon and M. Jaime, Rev. Mod. Phys. **73**, 583 (2001).

[35] A. Pergament, G. Stefanovich, N. Kuldin, and A. Velichko, ISRN Condensed Matter Physics **2013** (2013).

[36] G. Cao and L. De-Long, *Frontiers of 4d- and 5d-Transition Metal Oxides* (WORLD SCIENTIFIC, 2013).

[37] S. Rao and D. Sen, arXiv:cond-mat/0005492 (2000).

[38] K. Behnia, L. Balicas, and Y. Kopelevich, Science **317**, 1729 (2007).

[39] B. Fauque, B. Vignolle, C. Proust, J.-P. Issi, and K. Behnia, New J. Phys. **11**, 113012 (2009).

[40] R. Küchler, L. Steinke, R. Daou, M. Brando, K. Behnia, and F. Steglich, Nat. Mater. **13**, 461 (2014).

[41] L. Li, J. G. Checkelsky, Y. S. Hor, C. Uher, A. F. Hebard, R. J. Cava, and N. P. Ong, Science **321**, 547 (2008).

[42] B. Fauque, H. Yang, I. Sheikin, L. Balicas, J.-P. Issi, and K. Behnia, Phys. Rev. B **79**, 245124 (2009).

[43] Z. Zhu, B. Fauque, Y. Fuseya, and K. Behnia, Phys. Rev. B **84**, 115137 (2011).

[44] H. Yang, B. Fauqué, L. Malone, A. B. Antunes, Z. Zhu, C. Uher, and K. Behnia, Nat. Commun. **1**, 47 (2010).

[45] Z. Zhu, B. Fauque, L. Malone, A. B. Antunes, Y. Fuseya, and K. Behnia, Proceedings of the National Academy of Sciences **109**, 14813 (2012).

[46] S. Trebst, arXiv:1701.07056 (2017).

[47] L. Fu, Phys. Rev. Lett. **106**, 106802 (2011).

[48] T. H. Hsieh, H. Lin, J. Liu, W. Duan, A. Bansil, and L. Fu, Nat. Commun. **3**, 982 (2012).

[49] Y. Tanaka, Z. Ren, T. Sato, K. Nakayama, S. Souma, T. Takahashi, K. Segawa, and Y. Ando, Nat. Phys. **8**, 800 (2012).

[50] S.-Y. Xu, C. Liu, N. Alidoust, M. Neupane, D. Qian, I. Belopolski, J. Denlinger, Y. Wang, H. Lin, L. Wray, G. Landolt, B. Slomski, J. Dil, A. Marcinkova, E. Morosan, Q. Gibson, R. Sankar, F. Chou, R. Cava, A. Bansil, and M. Hasan, Nat. Commun. **3**, 1192 (2012).

[51] P. Dziawa, B. Kowalski, K. Dybko, R. Buczko, A. Szczerbakow, M. Szot, E. Łusakowska, T. Balasubramanian, B. M. Wojek, M. Berntsen, *et al.*, Nat. Mater. **11**, 1023 (2012).

[52] J. Liu, W. Duan, and L. Fu, Phys. Rev. B **88**, 241303 (2013).

[53] H. Yao and F. Yang, Phys. Rev. B **92**, 035132 (2015).

[54] I. Dzyaloshinskii, JETP Lett. **46** (1987).

[55] I. Dzyaloshinskii, J. Phys. I **6**, 119 (1996).

[56] D. Xiao, M.-C. Chang, and Q. Niu, Rev. Mod. Phys. **82**, 1959 (2010).

[57] N. Furukawa, T. Rice, and M. Salmhofer, Phys. Rev. Lett. **81**, 3195 (1998).

[58] R. Nandkishore, L. Levitov, and A. Chubukov, Nat. Phys. **8**, 158 (2012).

[59] C. Kallin, Rep. Prog. Phys. **75**, 042501 (2012).

[60] C. Kallin and J. Berlinsky, Rep. Prog. Phys. **79**, 054502 (2016).

[61] B. W. Heinrich, J. I. Pascual, and K. J. Franke, Progress in Surface Science **93**, 1 (2018).

[62] A. I. Rusinov, J. Exp. Theor. Phys. **29**, 1101 (1969).

[63] C. Beenakker, Annu. Rev. Condens. Matter Phys. **4**, 113 (2013).

[64] J. Alicea, Rep. Prog. Phys. **75**, 076501 (2012).

[65] M. Lannoo, Physica Scripta **T45**, 135 (1992).

[66] S. T. Pantelides, "Theory of impurity states in semiconductors," in *Festkorperprobleme 15: Plenary Lectures of the Divisions "Semiconductor Physics", "Low Temperature Physics", "Metal Physics" of the German Physical Society Münster, March 17–21, 1975*, edited by H. J. Queisser (Springer Berlin Heidelberg, Berlin, Heidelberg, 1975) pp. 149–181.

[67] J. Chaloupka, G. Jackeli, and G. Khaliullin, Phys. Rev. Lett. **110**, 097204 (2013).

[68] S. H. Chun, J.-W. Kim, J. Kim, H. Zheng, C. C. Stoumpos, C. Malliakas, J. Mitchell, K. Mehlawat, Y. Singh, Y. Choi, *et al.*, Nat. Phys. **11**, 462 (2015).

[69] R. Comin, G. Levy, B. Ludbrook, Z.-H. Zhu, C. Veenstra, J. Rosen, Y. Singh, P. Gegenwart, D. Stricker, J. N. Hancock, *et al.*, Phys. Rev. Lett. **109**, 266406 (2012).

[70] V. M. Katukuri, S. Nishimoto, V. Yushankhai, A. Stoyanova, H. Kandpal, S. Choi, R. Coldea, I. Rousochatzakis, L. Hozoi, and J. van den Brink, New J. Phys. **16**, 013056 (2014).

[71] X. Liu, T. Berlijn, W.-G. Yin, W. Ku, A. Tsvelik, Y.-J. Kim, H. Gretarsson, Y. Singh, P. Gegenwart, and J. Hill, Phys. Rev. B **83**, 220403 (2011).

[72] A. Banerjee, C. A. Bridges, J.-Q. Yan, A. A. Aczel, L. Li, M. B. Stone, G. E. Granroth, M. D. Lumsden, Y. Yiu, J. Knolle, S. Bhattacharjee, D. L. Kovrizhin, R. Moessner, D. A. Tennant, D. G. Mandrus, and S. E. Nagler, Nature Materials **15**, 733–740 (2016).

[73] S.-H. Baek, S.-H. Do, K.-Y. Choi, Y. S. Kwon, A. U. B. Wolter, S. Nishimoto, J. van den Brink, and B. Büchner, Phys. Rev. Lett. **119**, 037201 (2017).

[74] Z. Wang, S. Reschke, D. Hüvonen, S.-H. Do, K.-Y. Choi, M. Gensch, U. Nagel, T. Rõ om, and A. Loidl, Phys. Rev. Lett. **119**, 227202 (2017).

[75] S. M. Winter, K. Riedl, D. Kaib, R. Coldea, and R. Valentí, Phys. Rev. Lett. **120**, 077203 (2018).

[76] R. Yadav, N. A. Bogdanov, V. M. Katukuri, S. Nishimoto, J. van den Brink, and L. Hozoi, Sci. Rep. **6** (2016).

[77] A. Kitaev, Annals of Physics **321**, 2 (2006).

[78] J. G. Rau, E. K.-H. Lee, and H.-Y. Kee, Phys. Rev. Lett. **112**, 077204 (2014).

[79] J. G. Rau and H.-Y. Kee, arXiv:1408.4811 (2014).

[80] L. Janssen, E. C. Andrade, and M. Vojta, Phys. Rev. B **96**, 064430 (2017).

[81] K. Foyevtsova, H. O. Jeschke, I. I. Mazin, D. I. Khomskii, and R. Valentí, Phys. Rev. B **88**, 035107 (2013).

[82] Y. Sizyuk, C. Price, P. Wölfle, and N. B. Perkins, Phys. Rev. B **90**, 155126 (2014).

[83] J. Chaloupka and G. Khaliullin, Phys. Rev. B **94**, 064435 (2016).

[84] Y. Yamaji, Y. Nomura, M. Kurita, R. Arita, and M. Imada, Phys. Rev. Lett. **113**, 107201 (2014).

[85] K. Hu, F. Wang, and J. Feng, Phys. Rev. Lett. **115**, 167204 (2015).

[86] S. K. Choi, R. Coldea, A. N. Kolmogorov, T. Lancaster, I. I. Mazin, S. J. Blundell, P. G. Radaelli, Y. Singh, P. Gegenwart, K. R. Choi, S.-W. Cheong, P. J. Baker, C. Stock, and J. Taylor, Phys. Rev. Lett. **108**, 127204 (2012).

[87] Y. Singh, S. Manni, J. Reuther, T. Berlijn, R. Thomale, W. Ku, S. Trebst, and P. Gegenwart, Phys. Rev. Lett. **108**, 127203 (2012).

[88] I. A. Leahy, C. A. Pocs, P. E. Siegfried, D. Graf, S.-H. Do, K.-Y. Choi, B. Normand, and M. Lee, Phys. Rev. Lett. **118**, 187203 (2017).

[89] P. Chudzinski, M. Gabay, and T. Giamarchi, Phys. Rev. B **78**, 075124 (2008).

[90] D. Carpentier and E. Orignac, Phys. Rev. B **74**, 085409 (2006).

[91] Y. Suzumura and M. Tsuchiizu, J. Phys. Chem. Solids **62**, 93 (2001).

[92] E. Arrigoni, Phys. Lett. A **215**, 91 (1996).

[93] T. Kimura, K. Kuroki, and H. Aoki, Phys. Rev. B **54**, R9608 (1996).

[94] J.-J. Miao, F.-C. Zhang, and Y. Zhou, Phys. Rev. B **94**, 205129 (2016).

[95] J.-i. Okamoto and A. J. Millis, Phys. Rev. B **85**, 115406 (2012).

[96] V. Berezinskii, JETP **32**, 493 (1971).

[97] X.-G. Wen, Rev. Mod. Phys. **89**, 041004 (2017).

[98] J. Wang and S.-C. Zhang, Nat. Mater. **16**, 1062 (2017).

[99] A. Mesaros and Y. Ran, Phys. Rev. B **87**, 155115 (2013).

[100] C.-Y. Huang, X. Chen, and F. Pollmann, Phys. Rev. B **90**, 045142 (2014).

[101] T. Senthil, Annu. Rev. Condens. Matter Phys. **6**, 299 (2015).

[102] X.-G. Wen, Phys. Rev. B **85**, 085103 (2012).

[103] X. Chen, Z.-C. Gu, Z.-X. Liu, and X.-G. Wen, Phys. Rev. B **87**, 155114 (2013).

[104] M. Cheng, Z.-C. Gu, S. Jiang, and Y. Qi, Phys. Rev. B **96**, 115107 (2017).

[105] X.-L. Qi and S.-C. Zhang, Rev. Mod. Phys. **83**, 1057 (2011).

[106] M. Z. Hasan and C. L. Kane, Rev. Mod. Phys. **82**, 3045 (2010).

[107] Y. Ando and L. Fu, Annu. Rev. Condens. Matter Phys. **6**, 361 (2015).

[108] K. von Klitzing, Rev. Mod. Phys. **58**, 519 (1986).

[109] K. von Klitzing, Annu. Rev. Condens. Matter Phys. **8**, 13 (2017).

[110] D. J. Thouless, M. Kohmoto, M. P. Nightingale, and M. den Nijs, Phys. Rev. Lett. **49**, 405 (1982).

[111] B. A. Bernevig, T. L. Hughes, and S.-C. Zhang, Science **314**, 1757 (2006).

[112] X. Dai, T. L. Hughes, X.-L. Qi, Z. Fang, and S.-C. Zhang, Phys. Rev. B **77**, 125319 (2008).

[113] L. Fu, C. L. Kane, and E. J. Mele, Phys. Rev. Lett. **98**, 106803 (2007).

[114] J. C. Y. Teo, L. Fu, and C. L. Kane, Phys. Rev. B **78**, 045426 (2008).

[115] A. A. Taskin and Y. Ando, Phys. Rev. B **80**, 085303 (2009).

[116] H.-J. Zhang, C.-X. Liu, X.-L. Qi, X.-Y. Deng, X. Dai, S.-C. Zhang, and Z. Fang, Phys. Rev. B **80**, 085307 (2009).

[117] X.-G. Zhu, M. Stensgaard, L. Barreto, W. S. e Silva, S. Ulstrup, M. Michiardi, M. Bianchi, M. Dendzik, and P. Hofmann, New J. Phys. **15**, 103011 (2013).

[118] Z. Alpichshev, J. G. Analytis, J.-H. Chu, I. R. Fisher, and A. Kapitulnik, Phys. Rev. B **84**, 041104 (2011).

[119] P. Cheng, C. Song, T. Zhang, Y. Zhang, Y. Wang, J.-F. Jia, J. Wang, Y. Wang, B.-F. Zhu, X. Chen, X. Ma, K. He, L. Wang, X. Dai, Z. Fang, X. Xie, X.-L. Qi, C.-X. Liu, S.-C. Zhang, and Q.-K. Xue, Phys. Rev. Lett. **105**, 076801 (2010).

[120] L. Fu and E. Berg, Phys. Rev. Lett. **105**, 097001 (2010).

[121] H. Zhang, C.-X. Liu, X.-L. Qi, X. Dai, Z. Fang, and S.-C. Zhang, Nat. Phys. **5**, 438 (2009).

[122] C. Brüne, C. X. Liu, E. G. Novik, E. M. Hankiewicz, H. Buhmann, Y. L. Chen, X. L. Qi, Z. X. Shen, S. C. Zhang, and L. W. Molenkamp, Phys. Rev. Lett. **106**, 126803 (2011).

[123] A. Nishide, A. A. Taskin, Y. Takeichi, T. Okuda, A. Kakizaki, T. Hirahara, K. Nakatsuji, F. Komori, Y. Ando, and I. Matsuda, Phys. Rev. B **81**, 041309 (2010).

[124] J. Wang, Q. Zhou, B. Lian, and S.-C. Zhang, Phys. Rev. B **92**, 064520 (2015).

[125] K. Zhao, Y.-F. Lv, S.-H. Ji, X. Ma, X. Chen, and Q.-K. Xue, J. Phys. Condens. Matter **26**, 394003 (2014).

[126] W. A. Benalcazar, B. A. Bernevig, and T. L. Hughes, Science **357**, 61 (2017).

[127] F. Schindler, A. M. Cook, M. G. Vergniory, Z. Wang, S. S. P. Parkin, B. A. Bernevig, and T. Neupert, Science Advances **4** (2018).

[128] J. Langbehn, Y. Peng, L. Trifunovic, F. von Oppen, and P. W. Brouwer, Phys. Rev. Lett. **119**, 246401 (2017).

[129] F. Lu, B. Shi, and Y.-M. Lu, New J. Phys. **19**, 073002 (2017).

[130] H. Kim, K. Shiozaki, and S. Murakami, arXiv:1811.05153 (2018).

[131] S. Liu, A. Vishwanath, and E. Khalaf, arXiv:1809.01636 (2018).

[132] E. Khalaf, Phys. Rev. B **97**, 205136 (2018).

[133] G. van Miert and C. Ortix, Phys. Rev. B **98**, 081110 (2018).

[134] X. Zhou, C.-H. Hsu, T.-R. Chang, H.-J. Tien, Q. Ma, P. Jarillo-Herrero, N. Gedik, A. Bansil, V. M. Pereira, S.-Y. Xu, H. Lin, and L. Fu, Phys. Rev. B **98**, 241104 (2018).

[135] C.-H. Hsu, X. Zhou, Q. Ma, N. Gedik, A. Bansil, V. M. Pereira, H. Lin, L. Fu, S.-Y. Xu, and T.-R. Chang, 2D Materials **6**, 031004 (2019).

[136] T. Zhang, C. Yue, T. Zhang, S. Nie, Z. Wang, C. Fang, H. Weng, and Z. Fang, arXiv:1905.07253 (2019).

[137] S. K. Das, B. Yan, J. van den Brink, and I. C. Fulga, Phys. Rev. B **99**, 165418 (2019).

[138] Y. Tanaka, T. Shoman, K. Nakayama, S. Souma, T. Sato, T. Takahashi, M. Novak, K. Segawa, and Y. Ando, Phys. Rev. B **88**, 235126 (2013).

[139] C. S. Lent, M. A. Bowen, J. D. Dow, R. S. Allgaier, O. F. Sankey, and E. S. Ho, Superlattices and Microstructures **2**, 491 (1986).

[140] R. Tsu, W. E. Howard, and L. Esaki, Phys. Rev. **172**, 779 (1968).

[141] Y. W. Tung and M. L. Cohen, Phys. Rev. **180**, 823 (1969).

[142] H. T. Savage, B. Houston, and J. R. Burke, Phys. Rev. B **6**, 2292 (1972).

[143] L. M. Rogers, Journal of Physics D: Applied Physics **1**, 845 (1968).

[144] J. O. Dimmock, I. Melngailis, and A. J. Strauss, Phys. Rev. Lett. **16**, 1193 (1966).

[145] M. Sato and Y. Ando, Rep. Prog. Phys. **80**, 076501 (2017).

[146] M. Sato, Phys. Rev. B **81**, 220504 (2010).

[147] Z. Wu, Z. Yan, and W. Huang, Phys. Rev. B **99**, 020508 (2019).

[148] L. Fu and C. L. Kane, Phys. Rev. Lett. **100**, 096407 (2008).

[149] J. Alicea, Phys. Rev. B **81**, 125318 (2010).

[150] R. M. Lutchyn, J. D. Sau, and S. Das Sarma, Phys. Rev. Lett. **105**, 077001 (2010).

[151] T. D. Stanescu, R. M. Lutchyn, and S. Das Sarma, Phys. Rev. B **84**, 144522 (2011).

[152] R. M. Lutchyn, T. D. Stanescu, and S. Das Sarma, Phys. Rev. Lett. **106**, 127001 (2011).

[153] T. D. Stanescu and S. Tewari, J. Phys. Condens. Matter **25**, 233201 (2013).

[154] Q. L. He, L. Pan, A. L. Stern, E. C. Burks, X. Che, G. Yin, J. Wang, B. Lian, Q. Zhou, E. S. Choi, K. Murata, X. Kou, Z. Chen, T. Nie, Q. Shao, Y. Fan, S.-C. Zhang, K. Liu, J. Xia, and K. L. Wang, Science **357**, 294 (2017).

[155] R. M. Lutchyn, E. P. A. M. Bakkers, L. P. Kouwenhoven, P. Krogstrup, C. M. Marcus, and Y. Oreg, Nat. Rev. Mater. **3**, 52 (2018).

[156] J. D. Sau, R. M. Lutchyn, S. Tewari, and S. Das Sarma, Phys. Rev. Lett. **104**, 040502 (2010).

[157] C. Kallin and J. Berlinsky, Rep. Prog. Phys. **79**, 054502 (2016).

[158] Y. Maeno, S. Kittaka, T. Nomura, S. Yonezawa, and K. Ishida, J. Phys. Soc. Jpn. **81**, 011009 (2012).

[159] W.-S. Wang, C.-C. Zhang, F.-C. Zhang, and Q.-H. Wang, Phys. Rev. Lett. **122**, 027002 (2019).

[160] H. Wang, J. Luo, W. Lou, J. E. Ortmann, Z. Q. Mao, Y. Liu, and J. Wei, New J. Phys. **19**, 053001 (2017).

[161] W. Huang and H. Yao, Phys. Rev. Lett. **121**, 157002 (2018).

[162] S. Kittaka, S. Nakamura, T. Sakakibara, N. Kikugawa, T. Terashima, S. Uji, D. A. Sokolov, A. P. Mackenzie, K. Irie, Y. Tsutsumi, K. Suzuki, and K. Machida, J. Phys. Soc. Jpn. **87**, 093703 (2018).

[163] W. Huang, Y. Zhou, and H. Yao, arXiv:1901.07041 (2019).

[164] M. Saghir, J. A. T. Barker, G. Balakrishnan, A. D. Hillier, and M. R. Lees, Phys. Rev. B **90**, 064508 (2014).

[165] T. Sato, Y. Tanaka, K. Nakayama, S. Souma, T. Takahashi, S. Sasaki, Z. Ren, A. A. Taskin, K. Segawa, and Y. Ando, Phys. Rev. Lett. **110**, 206804 (2013).

[166] J. A. Krieger, A. Kanigel, A. Ribak, E. Pomjakushina, K. B. Chashka, K. Conder, E. Morenzoni, T. Prokscha, A. Suter, and Z. Salman, in *Proceedings of the 14th International Conference on Muon Spin Rotation, Relaxation and Resonance (μSR2017).*

[167] N. Levy, T. Zhang, J. Ha, F. Sharifi, A. A. Talin, Y. Kuk, and J. A. Stroscio, Phys. Rev. Lett. **110**, 117001 (2013).

[168] R. Tao, Y.-J. Yan, X. Liu, Z.-W. Wang, Y. Ando, Q.-H. Wang, T. Zhang, and D.-L. Feng, Phys. Rev. X **8**, 041024 (2018).

[169] P. Neha, P. Biswas, T. Das, and S. Patnaik, arXiv:1804.08998 (2018).

[170] M. P. Smylie, K. Willa, H. Claus, A. Snezhko, I. Martin, W.-K. Kwok, Y. Qiu, Y. S. Hor, E. Bokari, P. Niraula, A. Kayani, V. Mishra, and U. Welp, Phys. Rev. B **96**, 115145 (2017).

[171] A. Sirohi, S. Das, P. Neha, K. S. Jat, S. Patnaik, and G. Sheet, Phys. Rev. B **98**, 094523 (2018).

[172] S. Yonezawa, Condensed Matter **4** (2018).

[173] J. Shen, W.-Y. He, N. F. Q. Yuan, Z. Huang, C.-w. Cho, S. H. Lee, Y. S. Hor, K. T. Law, and R. Lortz, npj Quantum Materials **2**, 59 (2017).

[174] A. P. Mackenzie, R. K. W. Haselwimmer, A. W. Tyler, G. G. Lonzarich, Y. Mori, S. Nishizaki, and Y. Maeno, Phys. Rev. Lett. **80**, 161 (1998).

[175] S. Kundu and V. Tripathi, Phys. Rev. B **96**, 205111 (2017).

[176] M. Leijnse and K. Flensberg, Semiconductor Science and Technology **27**, 124003 (2012).

[177] A. Kitaev, Ann. Phys. **303**, 2 (2003).

[178] C. Nayak, S. H. Simon, A. Stern, M. Freedman, and S. Das Sarma, Rev. Mod. Phys. **80**, 1083 (2008).

[179] M. Wimmer, A. R. Akhmerov, M. V. Medvedyeva, J. Tworzydlo, and C. W. J. Beenakker, Phys. Rev. Lett. **105**, 046803 (2010).

[180] Y. E. Kraus, A. Auerbach, H. A. Fertig, and S. H. Simon, Phys. Rev. Lett. **101**, 267002 (2008).

[181] P. G. Björnsson, Y. Maeno, M. E. Huber, and K. A. Moler, Phys. Rev. B **72**, 012504 (2005).

[182] J. Jang, D. G. Ferguson, V. Vakaryuk, R. Budakian, S. B. Chung, P. M. Goldbart, and Y. Maeno, Science **331**, 186 (2011).

[183] G. M. Luke, Y. Fudamoto, K. M. Kojima, M. I. Larkin, J. Merrin, B. Nachumi, Y. J. Uemura, Y. Maeno, Z. Q. Mao, Y. Mori, H. Nakamura, and M. Sigrist, Nature **394**, 558 (1998).

[184] J. R. Kirtley, C. Kallin, C. W. Hicks, E.-A. Kim, Y. Liu, K. A. Moler, Y. Maeno, and K. D. Nelson, Phys. Rev. B **76**, 014526 (2007).

[185] M. Matsumoto and M. Sigrist, J. Phys. Soc. Jpn. **68**, 994 (1999).

[186] K. Ishida, H. Mukuda, Y. Kitaoka, K. Asayama, Z. Q. Mao, Y. Mori, and Y. Maeno, Nature **396**, 658 (1998).

[187] K. D. Nelson, Z. Q. Mao, Y. Maeno, and Y. Liu, Science **306**, 1151 (2004).

[188] S. Das, L. Aggarwal, S. Roychowdhury, M. Aslam, S. Gayen, K. Biswas, and G. Sheet, Appl. Phys. Lett. **109**, 132601 (2016).

[189] G. Mazur, K. Dybko, A. Szczerbakow, M. Zgirski, E. Lusakowska, S. Kret, J. Korczak, T. Story, M. Sawicki, and T. Dietl, arXiv:1709.04000 (2017).

[190] C.-X. Liu, J. D. Sau, T. D. Stanescu, and S. Das Sarma, Phys. Rev. B **96**, 075161 (2017).

[191] C.-X. Liu, J. D. Sau, and S. Das Sarma, Phys. Rev. B **97**, 214502 (2018).

[192] Z.-T. Zhang, J. Phys. Condens. Matter **30**, 145402 (2018).

[193] Y.-H. Lai, J. D. Sau, and S. Das Sarma, arXiv:1901.02655 (2019).

[194] K. Yavilberg, E. Ginossar, and E. Grosfeld, arXiv:1902.07229 (2019).

[195] Y.-C. Yam, S. Fang, P. Chen, Y. He, A. Soumyanarayanan, M. Hamidian, D. Gardner, Y. Lee, M. Franz, B. I. Halperian, E. Kaxiras, and J. E. Hoffman, arXiv:1810.13390 (2018).

[196] P. Sessi, D. Di Sante, A. Szczerbakow, F. Glott, S. Wilfert, H. Schmidt, T. Bathon, P. Dziawa, M. Greiter, T. Neupert, G. Sangiovanni, T. Story, R. Thomale, and M. Bode, Science **354**, 1269 (2016).

[197] H. Pan, W. S. Cole, J. D. Sau, and S. Das Sarma, arXiv:1906.08193 (2019).

[198] L. Tsui, Z.-X. Li, Y.-T. Huang, S. G. Louie, and D.-H. Lee, arXiv:1805.12150 (2018).

[199] B. D. Woods, J. Chen, S. M. Frolov, and T. D. Stanescu, arXiv:1902.02772 (2019).

[200] J. Chen, B. Woods, P. Yu, M. Hocevar, D. Car, S. Plissard, E. Bakkers, T. Stanescu, and S. Frolov, arXiv:1902.02773 (2019).

[201] Y. Kim, J. Zhang, E. Rossi, and R. M. Lutchyn, Phys. Rev. Lett. **114**, 236804 (2015).

[202] A. V. Balatsky, I. Vekhter, and J.-X. Zhu, Rev. Mod. Phys. **78**, 373 (2006).

[203] F. Wang, Q. Liu, T. Ma, and X. Jiang, J. Phys. Condens. Matter **24**, 455701 (2012).

[204] H. Shiba, Prog. Theor. Phys. **40**, 435 (1968).

[205] J. D. Sau and E. Demler, Phys. Rev. B **88**, 205402 (2013).

[206] S. Haas and K. Maki, Phys. Rev. Lett. **85**, 2172 (2000).

[207] V. Kaladzhyan, C. Bena, and P. Simon, J. Phys. Condens. Matter **28**, 485701 (2016).

[208] K. Maki and S. Haas, Phys. Rev. B **62**, R11969 (2000).

[209] Q.-H. Wang and Z. D. Wang, Phys. Rev. B **69**, 092502 (2004).

[210] S. Maiti and A. V. Chubukov, AIP Conference Proceedings **1550**, 3 (2013).

[211] M. Dayan, Journal of Physics F: Metal Physics **11**, L227 (1981).

[212] S. Kundu and V. Tripathi, Eur. Phys. J. B **91**, 198 (2018).

[213] A. Chubukov, Physica C: Superconductivity **469**, 640 (2009), superconductivity in Iron-Pnictides.

[214] S. Nadj-Perge, I. K. Drozdov, J. Li, H. Chen, S. Jeon, J. Seo, A. H. MacDonald, B. A. Bernevig, and A. Yazdani, Science **346**, 602 (2014).

[215] D. Wang, L. Kong, P. Fan, H. Chen, S. Zhu, W. Liu, L. Cao, Y. Sun, S. Du, J. Schneeloch, R. Zhong, G. Gu, L. Fu, H. Ding, and H.-J. Gao, Science **362**, 333 (2018).

[216] D. Iaia, C.-Y. Wang, Y. Maximenko, D. Walkup, R. Sankar, F. Chou, Y.-M. Lu, and V. Madhavan, Phys. Rev. B **99**, 155116 (2019).

[217] S. Kundu and V. Tripathi, Phys. Rev. B **99**, 205105 (2019).

[218] I. S. Gradshteyn and I. M. Ryzhik, *Table of integrals, series, and products*, seventh ed. (Elsevier/Academic Press, Amsterdam, 2007).

[219] I. Eremin, D. Manske, S. Ovchinnikov, and J. Annett, Annalen der Physik **13**, 149 (2004).

[220] L. Balents, Nature **6**, 376 (2010).

[221] Y. Iqbal, F. Becca, S. Sorella, and D. Poilblanc, Phys. Rev. B **87**, 060405 (2013).

[222] Y. Iqbal, W.-J. Hu, R. Thomale, D. Poilblanc, and F. Becca, Phys. Rev. B **93**, 144411 (2016).

[223] R. B. Laughlin and Z. Zou, Phys. Rev. B **41**, 664 (1990).

[224] W.-J. Hu, S.-S. Gong, W. Zhu, and D. N. Sheng, Phys. Rev. B **92**, 140403 (2015).

[225] H.-C. Jiang, H. Yao, and L. Balents, Phys. Rev. B **86**, 024424 (2012).

[226] T. V. Ramakrishnan, H. R. Krishnamurthy, S. R. Hassan, and G. V. Pai, Phys. Rev. Lett. **92**, 157203 (2004).

[227] B. J. Kim, H. Jin, S. J. Moon, J.-Y. Kim, B.-G. Park, C. S. Leem, J. Yu, T. W. Noh, C. Kim, S.-J. Oh, J.-H. Park, V. Durairaj, G. Cao, and E. Rotenberg, Phys. Rev. Lett. **101**, 076402 (2008).

[228] J. Chaloupka, G. Jackeli, and G. Khaliullin, Phys. Rev. Lett. **105**, 027204 (2010).

[229] S. D. Das, S. Kundu, Z. Zhu, E. Mun, R. D. McDonald, G. Li, L. Balicas, A. McCollam, G. Cao, J. G. Rau, H.-Y. Kee, V. Tripathi, and S. E. Sebastian, Phys. Rev. B **99**, 081101 (2019).

[230] Y. Kasahara, K. Sugii, T. Ohnishi, M. Shimozawa, M. Yamashita, N. Kurita, H. Tanaka, J. Nasu, Y. Motome, T. Shibauchi, and Y. Matsuda, Phys. Rev. Lett. **120**, 217205 (2018).

[231] Y. Kasahara, T. Ohnishi, Y. Mizukami, O. Tanaka, S. Ma, K. Sugii, N. Kurita, H. Tanaka, J. Nasu, Y. Motome, T. Shibauchi, and Y. Matsuda, Nature **559**, 227 (2018).

[232] K. Kugel and D. I. Khomskii, JETP Lett. - JETP LETT-ENGL TR **15**, 446 (1972).

[233] Z. Nussinov and J. van den Brink, Rev. Mod. Phys. **87**, 1 (2015).

[234] I. Dzyaloshinsky, J. Phys. Chem. Solids **4**, 241 (1958).

[235] I. Kimchi and Y.-Z. You, Phys. Rev. B **84**, 180407 (2011).

[236] Y. Singh and P. Gegenwart, Phys. Rev. B **82**, 064412 (2010).

[237] C. H. Sohn, H.-S. Kim, T. F. Qi, D. W. Jeong, H. J. Park, H. K. Yoo, H. H. Kim, J.-Y. Kim, T. D. Kang, D.-Y. Cho, G. Cao, J. Yu, S. J. Moon, and T. W. Noh, Phys. Rev. B **88**, 085125 (2013).

[238] H. Gretarsson, J. P. Clancy, X. Liu, J. P. Hill, E. Bozin, Y. Singh, S. Manni, P. Gegenwart, J. Kim, A. H. Said, D. Casa, T. Gog, M. H. Upton, H.-S. Kim, J. Yu, V. M. Katukuri, L. Hozoi, J. van den Brink, and Y.-J. Kim, Phys. Rev. Lett. **110**, 076402 (2013).

[239] H. Gretarsson, J. P. Clancy, Y. Singh, P. Gegenwart, J. P. Hill, J. Kim, M. H. Upton, A. H. Said, D. Casa, T. Gog, and Y.-J. Kim, Phys. Rev. B **87**, 220407 (2013).

[240] X. Yao, Physics Letters A **379**, 1480 (2015).

[241] T. Biesner, S. Biswas, W. Li, Y. Saito, A. Pustogow, M. Altmeyer, A. U. B. Wolter, B. Büchner, M. Roslova, T. Doert, S. M. Winter, R. Valentí, and M. Dressel, Phys. Rev. B **97**, 220401 (2018).

[242] A. Banerjee, P. Lampen-Kelley, J. Knolle, C. Balz, A. A. Aczel, B. Winn, Y. Liu, D. Pajerowski, J. Yan, C. A. Bridges, A. T. Savici, B. C. Chakoumakos, M. D. Lumsden, D. A. Tennant, R. Moessner, D. G. Mandrus, and S. E. Nagler, npj Quantum Materials **3**, 2397 (2018).

[243] A. U. B. Wolter, L. T. Corredor, L. Janssen, K. Nenkov, S. Schönecker, S.-H. Do, K.-Y. Choi, R. Albrecht, J. Hunger, T. Doert, M. Vojta, and B. Büchner, Phys. Rev. B **96**, 041405 (2017).

[244] L. Y. Shi, Y. Q. Liu, T. Lin, M. Y. Zhang, S. J. Zhang, L. Wang, Y. G. Shi, T. Dong, and N. L. Wang, Phys. Rev. B **98**, 094414 (2018).

[245] K. W. Plumb, J. P. Clancy, L. J. Sandilands, V. V. Shankar, Y. F. Hu, K. S. Burch, H.-Y. Kee, and Y.-J. Kim, Phys. Rev. B **90**, 041112 (2014).

[246] A. Banerjee, J. Yan, J. Knolle, C. A. Bridges, M. B. Stone, M. D. Lumsden, D. G. Mandrus, D. A. Tennant, R. Moessner, and S. E. Nagler, Science **356**, 1055 (2017).

[247] L. J. Sandilands, Y. Tian, K. W. Plumb, Y.-J. Kim, and K. S. Burch, Phys. Rev. Lett. **114**, 147201 (2015).

[248] J. Nasu, J. Knolle, D. Kovrizhin, Y. Motome, and R. Moessner, Nat. Phys. **12**, 912 (2016).

[249] C. Balz, P. Lampen-Kelly, A. Banerjee, J. Yan, Z. Lu, X. Hu, S. M. Yadav, Y. Takano, Y. Liu, D. A. Tennant, M. D. Lumsden, D. Mandrus, and S. E. Nagler, arXiv:1903.00056 (2019).

[250] Y. Wang, G. B. Osterhoudt, Y. Tian, P. Lampen-Kelly, A. Banerjee, T. Goldstein, J. Yan, J. Knolle, H. Ji, R. J. Cava, J. Nasu, Y. Motome, S. E. Nagler, D. Mandrus, and K. S. Burch, arXiv:1809.07782 (2018).

[251] J. Zheng, K. Ran, T. Li, J. Wang, P. Wang, B. Liu, Z.-X. Liu, B. Normand, J. Wen, and W. Yu, Phys. Rev. Lett. **119**, 227208 (2017).

[252] A. N. Ponomaryov, E. Schulze, J. Wosnitza, P. Lampen-Kelley, A. Banerjee, J.-Q. Yan, C. A. Bridges, D. G. Mandrus, S. E. Nagler, A. K. Kolezhuk, and S. A. Zvyagin, Phys. Rev. B **96**, 241107 (2017).

[253] Y. J. Yu, Y. Xu, K. J. Ran, J. M. Ni, Y. Y. Huang, J. H. Wang, J. S. Wen, and S. Y. Li, Phys. Rev. Lett. **120**, 067202 (2018).

[254] R. Hentrich, A. U. B. Wolter, X. Zotos, W. Brenig, D. Nowak, A. Isaeva, T. Doert, A. Banerjee, P. Lampen-Kelley, D. G. Mandrus, S. E. Nagler, J. Sears, Y.-J. Kim, B. Büchner, and C. Hess, Phys. Rev. Lett. **120**, 117204 (2018).

[255] S. Reschke, V. Tsurkan, S.-H. Do, K.-Y. Choi, P. Lunkenheimer, Z. Wang, and A. Loidl, arXiv:1902.10453 (2019).

[256] L. Wu, A. Little, E. E. Aldape, D. Rees, E. Thewalt, P. Lampen-Kelley, A. Banerjee, C. A. Bridges, J.-Q. Yan, D. Boone, S. Patankar, D. Goldhaber-Gordon, D. Mandrus, S. E. Nagler, E. Altman, and J. Orenstein, Phys. Rev. B **98**, 094425 (2018).

[257] D. Takikawa and S. Fujimoto, Phys. Rev. B **99**, 224409 (2019).

[258] J. Cookmeyer and J. E. Moore, Phys. Rev. B **98**, 060412 (2018).

[259] G. Y. Hao, C. Hickey, T. Xiang, S. Trebst, and G. Chen, arXiv:1905.11321 (2019).

[260] K. A. Modic, B. J. Ramshaw, J. B. Betts, N. P. Breznay, J. G. Analytis, R. D. McDonald, and A. Shekhter, Nat. Commun. **8**, 180 (2017).

[261] A. Ruiz, A. Frano, N. P. Breznay, I. Kimchi, T. Helm, I. Oswald, J. Y. Chan, R. J. Birgeneau, Z. Islam, and J. G. Analytis, Nat. Commun. **8**, 961 (2017).

[262] S. Das, *Anisotropic studies on pnictide superconductors and frustrated quantum magnets* (2014).

[263] A. Revelli, M. Moretti Sala, G. Monaco, C. Hickey, P. Becker, F. Freund, A. Jesche, P. Gegenwart, T. Eschmann, F. Buessen, S. Trebst, P. van Loosdrecht, J. van den Brink, and M. Gruninger, arXiv:1905.13590 (2019).

[264] E. R. Gagliano, E. Dagotto, A. Moreo, and F. C. Alcaraz, Phys. Rev. B **34**, 1677 (1986).

[265] F. Trousselet, G. Khaliullin, and P. Horsch, Phys. Rev. B **84**, 054409 (2011).

[266] K. Le Hur, A. Soret, and F. Yang, Phys. Rev. B **96**, 205109 (2017).

[267] R. V. Mishmash, M. S. Block, R. K. Kaul, D. N. Sheng, O. I. Motrunich, and M. P. A. Fisher, Phys. Rev. B **84**, 245127 (2011).

[268] D. Podolsky, E. Altman, T. Rostunov, and E. Demler, Phys. Rev. B **70**, 224503 (2004).

[269] D. Podolsky, E. Altman, T. Rostunov, and E. Demler, Phys. Rev. Lett. **93**, 246402 (2004).

[270] U. Schollwöck, Rev. Mod. Phys. **77**, 259 (2005).

[271] U. Schollwöck, Ann. Phys. **326**, 96 (2011).

[272] D. G. Shelton, A. A. Nersesyan, and A. M. Tsvelik, Phys. Rev. B **53**, 8521 (1996).

[273] M. Sato, Phys. Rev. B **76**, 054427 (2007).

[274] W. Vincent Liu and E. Fradkin, Phys. Rev. Lett. **86**, 1865 (2001).

[275] L. Balents and M. P. A. Fisher, Phys. Rev. B **53**, 12133 (1996).

[276] M. Fabrizio, Phys. Rev. B **48**, 15838 (1993).

[277] H. J. Schulz, Phys. Rev. B **53**, R2959 (1996).

[278] E. Orignac and T. Giamarchi, Phys. Rev. B **56**, 7167 (1997).

[279] K. L. Hur, Phys. Rev. B **63**, 165110 (2001).

[280] C. Wu, W. Vincent Liu, and E. Fradkin, Phys. Rev. B **68**, 115104 (2003).

[281] M. Tsuchiizu, P. Donohue, Y. Suzumura, and T. Giamarchi, Eur. Phys. J. B - Condensed Matter and Complex Systems **19**, 185 (2001).

[282] S. T. Carr, B. N. Narozhny, and A. A. Nersesyan, Phys. Rev. B **73**, 195114 (2006).

[283] P. Chudzinski, M. Gabay, and T. Giamarchi, Phys. Rev. B **76**, 161101 (2007).

[284] S. Nishimoto, E. Jeckelmann, and D. J. Scalapino, Phys. Rev. B **66**, 245109 (2002).

[285] J. Fjaerestad, J. Marston, and U. Schollwöck, Ann. Phys. **321**, 894 (2006).

[286] J. O. Fjaerestad and J. B. Marston, Phys. Rev. B **65**, 125106 (2002).

[287] B. Srinivasan and M.-B. Lepetit, Phys. Rev. B **66**, 024421 (2002).

[288] M. Tsuchiizu and A. Furusaki, Phys. Rev. B **66**, 245106 (2002).

[289] S. Nishimoto, E. Jeckelmann, and D. Scalapino, Physica C: Superconductivity **470** (2010).

[290] D. Controzzi and A. M. Tsvelik, Phys. Rev. B **72**, 035110 (2005).

[291] N. J. Robinson, F. H. L. Essler, E. Jeckelmann, and A. M. Tsvelik, Phys. Rev. B **85**, 195103 (2012).

[292] S. Wessel, M. Indergand, A. Lauchli, U. Ledermann, and M. Sigrist, Phys. Rev. B **67**, 184517 (2003).

[293] E. Arrigoni, Physica Status Solidi (B) **195**, 425 (1996).

[294] T. Kimura, K. Kuroki, and H. Aoki, J. Phys. Soc. Jpn. **67**, 1377 (1998).

[295] S. Kundu and V. Tripathi, arXiv:1906.11053 (2019).

[296] M. Dresselhaus and G. Dresselhaus, Advances in Physics **30**, 139 (1981).

[297] F. L. Vogel, "Intercalation compounds of graphite," in *Molecular Metals*, edited by W. E. Hatfield (Springer US, Boston, MA, 1979) pp. 261–279.

[298] B. Seradjeh, J. Wu, and P. Phillips, Phys. Rev. Lett. **103**, 136803 (2009).

[299] M. Matsuo, A. Endo, N. Hatano, H. Nakamura, R. Shirasaki, and K. Sugihara, Phys. Rev. B **80**, 075313 (2009).

[300] J. Alicea and L. Balents, Phys. Rev. B **79**, 241101 (2009).

[301] Y. V. Sharlai and G. P. Mikitik, Phys. Rev. B **79**, 081102 (2009).

[302] S. Koley, M. S. Laad, and A. Taraphder, Sci. Rep. **7**, 10993 (2017).

[303] C. Honerkamp, M. Salmhofer, N. Furukawa, and T. M. Rice, Phys. Rev. B **63**, 035109 (2001).

Appendix A

Parquet RG equations in the presence of an external magnetization

Here we present the RG equations in the presence of an external magnetization M, which is taken into account by introducing additional form factors $v_\uparrow(M)$ and $v_\downarrow(M)$ in the RG equations. Corresponding to every scattering channel h_r, we then have four components $h_r^{\uparrow\uparrow}$, $h_r^{\downarrow\downarrow}$, $h_r^{\uparrow\downarrow}$ and $h_r^{\downarrow\uparrow}$, alternately denoted by h_r^0, h_r^2, h_r^1 and h_r^3 respectively. This gives us a set of 16 coupling constants. The final set of RG equations are given by

$$
\begin{aligned}
\frac{dh_1^{\sigma\sigma}}{dy} &= \frac{2}{\sqrt{1+y}}((h_3^{\sigma\sigma})^2 v_\sigma^2 \\
&\quad - (h_1^{\sigma\sigma})^2 v_\sigma^2 - (h_3^{\sigma\overline{\sigma}})(h_3^{\overline{\sigma}\sigma}) v_{\overline{\sigma}}^2 \\
&\quad - (h_1^{\sigma\overline{\sigma}})(h_1^{\overline{\sigma}\sigma}) v_{\overline{\sigma}}^2 + 2(h_1^{\sigma\sigma})(h_2^{\sigma\sigma}) v_\sigma^2) \\
\frac{dh_1^{\overline{\sigma}\overline{\sigma}}}{dy} &= \frac{2}{\sqrt{1+y}}((h_3^{\overline{\sigma}\overline{\sigma}})^2 v_{\overline{\sigma}}^2 \\
&\quad - (h_1^{\overline{\sigma}\overline{\sigma}})^2 v_{\overline{\sigma}}^2 - (h_3^{\overline{\sigma}\sigma})(h_3^{\sigma\overline{\sigma}}) v_\sigma^2 \\
&\quad - (h_1^{\overline{\sigma}\sigma})(h_1^{\sigma\overline{\sigma}}) v_\sigma^2 + 2(h_1^{\overline{\sigma}\overline{\sigma}})(h_2^{\overline{\sigma}\overline{\sigma}}) v_{\overline{\sigma}}^2) \\
\frac{dh_1^{\sigma\overline{\sigma}}}{dy} &= \frac{2h_1^{\sigma\overline{\sigma}}}{\sqrt{1+y}}(-(h_1^{\overline{\sigma}\overline{\sigma}}) v_{\overline{\sigma}}^2 - (h_1^{\sigma\sigma}) v_\sigma^2 \\
&\quad + (h_2^{\sigma\sigma}) v_\sigma^2 + (h_2^{\overline{\sigma}\overline{\sigma}}) v_{\overline{\sigma}}^2) \\
\frac{dh_1^{\overline{\sigma}\sigma}}{dy} &= \frac{2h_1^{\overline{\sigma}\sigma}}{\sqrt{1+y}}(-(h_1^{\overline{\sigma}\overline{\sigma}}) v_{\overline{\sigma}}^2 - (h_1^{\sigma\sigma}) v_\sigma^2 \\
&\quad + (h_2^{\sigma\sigma}) v_\sigma^2 + (h_2^{\overline{\sigma}\overline{\sigma}}) v_{\overline{\sigma}}^2) \\
\frac{dh_2^{\sigma\sigma}}{dy} &= \frac{2}{\sqrt{1+y}}((h_2^{\sigma\sigma})^2 + (h_3^{\sigma\sigma})^2) v_\sigma^2 \\
\frac{dh_2^{\overline{\sigma}\overline{\sigma}}}{dy} &= \frac{2}{\sqrt{1+y}}((h_2^{\overline{\sigma}\overline{\sigma}})^2 + (h_3^{\overline{\sigma}\overline{\sigma}})^2) v_{\overline{\sigma}}^2 \\
\frac{dh_2^{\sigma\overline{\sigma}}}{dy} &= \frac{2}{\sqrt{1+y}}((h_2^{\sigma\overline{\sigma}})^2 + (h_3^{\sigma\overline{\sigma}})^2) v_\sigma v_{\overline{\sigma}} \\
\frac{dh_2^{\overline{\sigma}\sigma}}{dy} &= \frac{2}{\sqrt{1+y}}((h_2^{\overline{\sigma}\sigma})^2 + (h_3^{\overline{\sigma}\sigma})^2) v_\sigma v_{\overline{\sigma}} \\
\frac{dh_3^{\sigma\sigma}}{dy} &= -4h_3^{\sigma\sigma} h_4^{\sigma\sigma} v_\sigma^2 + \frac{2}{\sqrt{1+y}}(4h_2^{\sigma\sigma} h_3^{\sigma\sigma} v_\sigma^2
\end{aligned}
$$

$$
\begin{aligned}
&\quad - h_1^{\overline{\sigma}\sigma} h_3^{\sigma\overline{\sigma}} v_{\overline{\sigma}}^2 - h_1^{\sigma\overline{\sigma}} h_3^{\overline{\sigma}\sigma} v_{\overline{\sigma}}^2) \\
\frac{dh_3^{\overline{\sigma}\overline{\sigma}}}{dy} &= -4h_3^{\overline{\sigma}\overline{\sigma}} h_4^{\overline{\sigma}\overline{\sigma}} v_{\overline{\sigma}}^2 + \frac{2}{\sqrt{1+y}}(4h_2^{\overline{\sigma}\overline{\sigma}} h_3^{\overline{\sigma}\overline{\sigma}} v_{\overline{\sigma}}^2 \\
&\quad - h_1^{\overline{\sigma}\sigma} h_3^{\sigma\overline{\sigma}} v_{\sigma}^2 - h_1^{\sigma\overline{\sigma}} h_3^{\overline{\sigma}\sigma} v_{\sigma}^2) \\
\frac{dh_3^{\sigma\overline{\sigma}}}{dy} &= -4h_3^{\sigma\overline{\sigma}} h_4^{\sigma\overline{\sigma}} v_{\sigma} v_{\overline{\sigma}} \\
&\quad + \frac{2}{\sqrt{1+y}}(2h_2^{\sigma\overline{\sigma}} h_3^{\sigma\overline{\sigma}} v_{\sigma} v_{\overline{\sigma}} + \\
&\quad h_3^{\sigma\overline{\sigma}}(h_2^{\sigma\sigma} v_{\sigma}^2 + h_2^{\overline{\sigma}\overline{\sigma}} v_{\overline{\sigma}}^2 - h_1^{\sigma\sigma} v_{\sigma}^2 - h_1^{\overline{\sigma}\overline{\sigma}} v_{\overline{\sigma}}^2)) \\
\frac{dh_3^{\overline{\sigma}\sigma}}{dy} &= -4h_3^{\overline{\sigma}\sigma} h_4^{\overline{\sigma}\sigma} v_{\sigma} v_{\overline{\sigma}} \\
&\quad + \frac{2}{\sqrt{1+y}}(2h_2^{\overline{\sigma}\sigma} h_3^{\overline{\sigma}\sigma} v_{\sigma} v_{\overline{\sigma}} + \\
&\quad h_3^{\overline{\sigma}\sigma}(h_2^{\sigma\sigma} v_{\sigma}^2 + h_2^{\overline{\sigma}\overline{\sigma}} v_{\overline{\sigma}}^2 - h_1^{\sigma\sigma} v_{\sigma}^2 - h_1^{\overline{\sigma}\overline{\sigma}} v_{\overline{\sigma}}^2)) \\
\frac{dh_4^{\sigma\sigma}}{dy} &= -2((h_3^{\sigma\sigma})^2 + (h_4^{\sigma\sigma})^2) v_{\sigma}^2 \\
\frac{dh_4^{\overline{\sigma}\overline{\sigma}}}{dy} &= -2((h_3^{\overline{\sigma}\overline{\sigma}})^2 + (h_4^{\overline{\sigma}\overline{\sigma}})^2) v_{\overline{\sigma}}^2 \\
\frac{dh_4^{\sigma\overline{\sigma}}}{dy} &= -2((h_3^{\sigma\overline{\sigma}})^2 + (h_4^{\sigma\overline{\sigma}})^2) v_{\sigma} v_{\overline{\sigma}} \\
\frac{dh_4^{\overline{\sigma}\sigma}}{dy} &= -2((h_3^{\overline{\sigma}\sigma})^2 + (h_4^{\overline{\sigma}\sigma})^2) v_{\sigma} v_{\overline{\sigma}},
\end{aligned}
$$

Fixed-point behavior of the couplings

The different couplings $h_r^{\ell}(y)$ have an asymptotic form $\frac{g_r^{\ell}}{y_c - y}$ near the critical point y_c of the RG flow. In order to determine the behavior of the fixed point values g_r^{ℓ} for the different couplings as a function of $d_1(y_c)$, we substitute this asymptotic form into the RG equations to obtain the polynomial equations, as follows-

$$
\begin{aligned}
g_1^0 &= 2d_1(y_c)(-(g_1^0)^2-(g_3^1)^2-(g_1^1)^2+2g_1^0g_2^0+(g_3^0)^2),\\
g_1^1 &= 2d_1(y_c)(-2g_1^0g_1^1+2g_1^1g_2^0),\\
g_2^0 &= 2d_1(y_c)((g_2^0)^2+(g_3^0)^2),\\
g_2^1 &= 2d_1(y_c)((g_2^1)^2+(g_3^1)^2),\\
g_3^0 &= -4g_4^0g_3^0+2d_1(y_c)(4g_2^0g_3^0-2g_1^1g_3^1),\\
g_3^1 &= -4g_4^1g_3^1+2d_1(y_c)(2g_2^1g_3^1-2g_1^0g_3^1+2g_2^0g_3^1),\\
g_4^0 &= -2(g_4^0)^2-2(g_3^0)^2,\\
g_4^1 &= -2(g_4^1)^2-2(g_3^1)^2. \qquad (1)
\end{aligned}
$$

These coupled equations are then solved with appropriate initial conditions, to determine g_r^ℓ ($\ell = 0, 1$) as a function of $d_1(y_c)$, which is the ratio of the particle-hole and particle-particle susceptibilities at the fixed point y_c. The behaviour of g_r^ℓ as a function of $d_1(y_c)$ when the degeneracy between the couplings in the $\ell = 0$ and $\ell = 1$ channels is lifted (such that $g_r^0 > g_r^1$ for all r) is shown in Fig. 2.

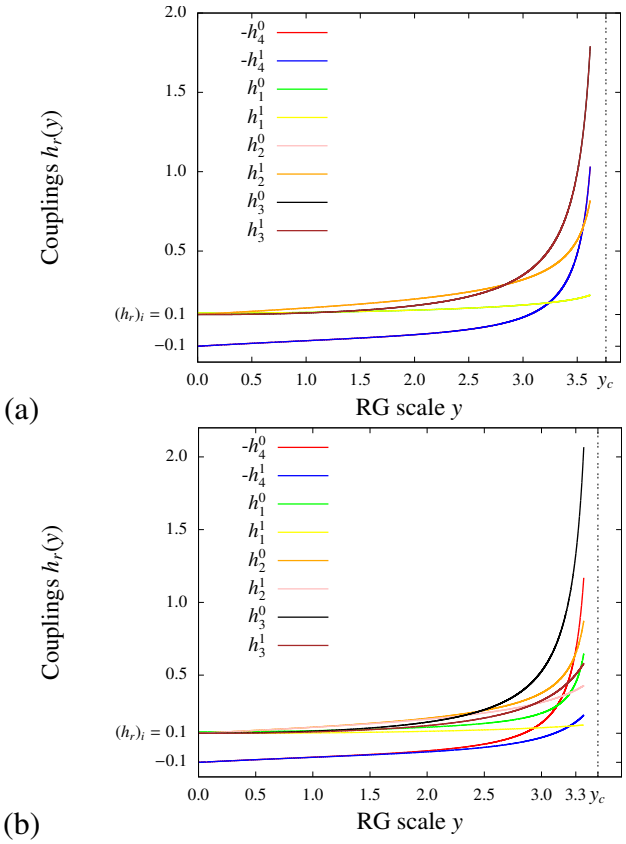

Fig. 1 (a) Flow of the couplings with the RG scale y, with an initial splitting in the different scattering channels r. Here we have chosen the initial value of h_1 to be greater than all the other h_r by 10%, i.e. $\frac{|h_1^\ell - h_r^\ell|}{|h_r^\ell|} = 0.1$ $(r \neq 1)$ for $\ell = 0, 1$, where $(h_r^\ell)_{initial} = 0.1$ for $r \neq 1$. The resulting order of the couplings at the fixed-point y_c is identical to the case where all the couplings are chosen to be degenerate initially, and $h_3^{0,1}$ and $(-h_4^{0,1})$ are the dominant couplings. This illustrates that our RG flows are insensitive to the initial order of the couplings in different scattering channels $r = 1 - 4$, as long as $h_r^0 = h_r^1$ for all r. Here, the critical point $y_c \approx 3.8$. (b) Flow of the couplings with the RG scale y, with $h_1^0 > h_1^1$ by 10% initially, i.e. $\frac{|h_1^0 - h_1^1|}{|h_1^1|} = 0.1$, where $(h_r^0)_{initial} = 0.1$ for $r \neq 1$ and $(h_r^1)_{initial} = 0.1$ for all r. This changes the order of the couplings at the fixed point drastically, and now h_3^0 and $(-h_4^0)$ dominate near the fixed point of the RG flow.

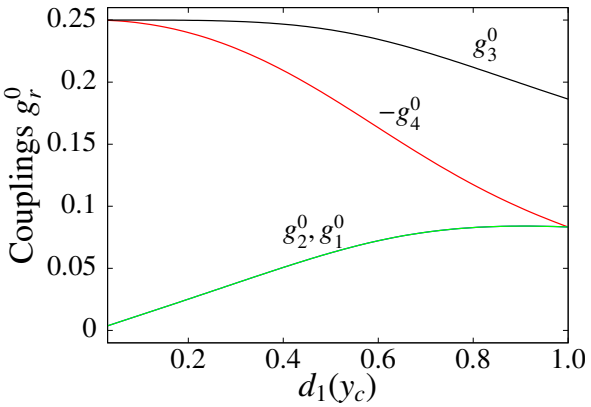

Fig. 2 The fixed point values for g_r^0 as a function of $d_1(y_c)$ for the case where the $\ell = 0$ components of all the couplings dominate initially. Note that the fixed point values g_2^0 and g_1^0 turn out to be identical.

Appendix B

Ladder RG equations in the absence of Hund's splitting

In the absence of Hund's splitting, i.e. when the various components of interactions h_i in the different scattering channels $i = 1-4$ are taken to be identical initially, p-wave superconductivity cannot be stabilized at energies corresponding to the fixed point of the parquet RG. However, when the Fermi energy E_F associated with the system exceeds the energy ω_c corresponding to the critical point y_c, the RG flow must be terminated at E_F, and any possible instabilities will then depend on the order of the different couplings at the Fermi energy. These are determined using a ladder RG approach.

Two kinds of vertices continue to flow logarithmically at energies below the Fermi energy E_F: vertices with zero total momentum, and with total momentum exactly equal to the nesting vector Q in two dimensions. The vertices with zero total momentum are the h_3 and h_4 terms in our RG analysis and the vertices with total momentum Q are the h_1, h_2 and h_3 terms. The values of h_i at E_F act as the bare couplings for the theory at $\omega < E_F$. There are two kinds of h_3 vertices with a momentum transfer Q, h_{3a} and h_{3b} and we denote the h_3 vertex with zero total momentum as h_{3c}. We shall refer to the vertices with zero total momentum as $h_i(0)$ and the vertices with total momentum Q as $h_i(Q)$. The ladder RG equations are obtained by considering those diagrams which still yield a logarithmic divergence.

The ladder RG equations for our system, where now $y \equiv \ln[\frac{E_F}{\omega}]$, are given as follows-

$$\begin{aligned}\frac{dh_1^{\sigma\sigma}(Q)}{dy} &= 2((2h_{3a}^{\sigma\sigma}(Q)h_{3b}^{\sigma\sigma}(Q) - (h_{3a}^{\sigma\sigma}(Q))^2)v_\sigma^2 \\ &\quad - (h_1^{\sigma\sigma}(Q))^2 v_\sigma^2 - (h_{3a}^{\sigma\overline{\sigma}}(Q))(h_{3a}^{\overline{\sigma}\sigma}(Q))v_{\overline{\sigma}}^2 - \\ &\quad (h_1^{\sigma\overline{\sigma}}(Q))(h_1^{\overline{\sigma}\sigma}(Q))v_{\overline{\sigma}}^2 + 2(h_1^{\sigma\sigma}(Q))(h_2^{\sigma\sigma}(Q))v_\sigma^2)\end{aligned}$$

$$\begin{aligned}\frac{dh_1^{\overline{\sigma}\overline{\sigma}}(Q)}{dy} &= 2((2(h_{3a}^{\overline{\sigma}\overline{\sigma}}(Q))(h_{3b}^{\overline{\sigma}\overline{\sigma}}(Q)) - (h_{3a}^{\overline{\sigma}\overline{\sigma}}(Q))^2)v_{\overline{\sigma}}^2 \\ &\quad - (h_1^{\overline{\sigma}\overline{\sigma}}(Q))^2 v_{\overline{\sigma}}^2 - (h_{3a}^{\overline{\sigma}\sigma}(Q))(h_{3a}^{\sigma\overline{\sigma}}(Q))v_\sigma^2 - \\ &\quad (h_1^{\overline{\sigma}\sigma}(Q))(h_1^{\sigma\overline{\sigma}}(Q))v_\sigma^2 + 2(h_1^{\overline{\sigma}\overline{\sigma}}(Q))(h_2^{\overline{\sigma}\overline{\sigma}}(Q))v_{\overline{\sigma}}^2)\end{aligned}$$

$$\frac{dh_1^{\sigma\overline{\sigma}}(Q)}{dy} = 2(h_{3a}^{\sigma\overline{\sigma}}(Q)(h_{3b}^{\overline{\sigma}\overline{\sigma}}(Q) - h_{3a}^{\overline{\sigma}\overline{\sigma}}(Q))v_{\overline{\sigma}}^2 + h_{3a}^{\sigma\overline{\sigma}}(Q)(h_{3b}^{\sigma\sigma}(Q) - h_{3a}^{\sigma\sigma}(Q))v_{\sigma}^2 + h_1^{\sigma\overline{\sigma}}(Q)(-(h_1^{\overline{\sigma}\overline{\sigma}}(Q))v_{\overline{\sigma}}^2 - (h_1^{\sigma\sigma}(Q))v_{\sigma}^2 + (h_2^{\sigma\sigma}(Q))v_{\sigma}^2 + (h_2^{\overline{\sigma}\overline{\sigma}}(Q))v_{\overline{\sigma}}^2)$$

-

$$\frac{dh_1^{\overline{\sigma}\sigma}(Q)}{dy} = 2(h_{3a}^{\overline{\sigma}\sigma}(Q)(h_{3b}^{\overline{\sigma}\overline{\sigma}}(Q) - h_{3a}^{\overline{\sigma}\overline{\sigma}}(Q))v_{\overline{\sigma}}^2 + h_{3a}^{\overline{\sigma}\sigma}(Q)(h_{3b}^{\sigma\sigma}(Q) - h_{3a}^{\sigma\sigma}(Q))v_{\sigma}^2 + h_1^{\overline{\sigma}\sigma}(Q)(-(h_1^{\overline{\sigma}\overline{\sigma}}(Q))v_{\overline{\sigma}}^2 - (h_1^{\sigma\sigma}(Q))v_{\sigma}^2 + (h_2^{\sigma\sigma}(Q))v_{\sigma}^2 + (h_2^{\overline{\sigma}\overline{\sigma}}(Q))v_{\overline{\sigma}}^2)$$

$$\frac{dh_2^{\sigma\sigma}(Q)}{dy} = 2((h_2^{\sigma\sigma}(Q))^2 + (h_{3b}^{\sigma\sigma}(Q))^2)v_{\sigma}^2$$
$$\frac{dh_2^{\overline{\sigma}\overline{\sigma}}(Q)}{dy} = 2((h_2^{\overline{\sigma}\overline{\sigma}}(Q))^2 + (h_{3b}^{\overline{\sigma}\overline{\sigma}}(Q))^2)v_{\overline{\sigma}}^2$$

$$\frac{dh_2^{\sigma\overline{\sigma}}(Q)}{dy} = 2((h_2^{\sigma\overline{\sigma}}(Q))^2 + (h_{3b}^{\sigma\overline{\sigma}}(Q))^2)v_{\sigma}v_{\overline{\sigma}}$$
$$\frac{dh_2^{\overline{\sigma}\sigma}(Q)}{dy} = 2((h_2^{\overline{\sigma}\sigma}(Q))^2 + (h_{3b}^{\overline{\sigma}\sigma}(Q))^2)v_{\sigma}v_{\overline{\sigma}}$$

$$\frac{dh_{3a}^{\sigma\sigma}(Q)}{dy} = 2(2h_1^{\sigma\sigma}(Q)(h_{3b}^{\sigma\sigma}(Q) - h_{3a}^{\sigma\sigma}(Q))v_{\sigma}^2 + 2h_2^{\sigma\sigma}(Q)h_{3a}^{\sigma\sigma}(Q)v_{\sigma}^2 - h_1^{\overline{\sigma}\sigma}(Q)h_{3a}^{\sigma\overline{\sigma}}(Q)v_{\overline{\sigma}}^2 - h_1^{\sigma\overline{\sigma}}(Q)h_{3a}^{\overline{\sigma}\sigma}(Q)v_{\overline{\sigma}}^2)$$

$$\frac{dh_{3b}^{\sigma\sigma}(Q)}{dy} = 4h_2^{\sigma\sigma}(Q)h_{3b}^{\sigma\sigma}(Q)v_{\sigma}^2$$
$$\frac{dh_{3c}^{\sigma\sigma}(0)}{dy} = -4h_4^{\sigma\sigma}(0)h_{3c}^{\sigma\sigma}(0)v_{\sigma}^2$$

$$\frac{dh_{3a}^{\overline{\sigma}\sigma}(Q)}{dy} = 2(2h_1^{\overline{\sigma}\sigma}(Q)(h_{3b}^{\overline{\sigma}\sigma}(Q) - h_{3a}^{\overline{\sigma}\sigma}(Q))v_{\overline{\sigma}}^2 + 2h_2^{\overline{\sigma}\sigma}(Q)h_{3a}^{\overline{\sigma}\sigma}(Q)v_{\overline{\sigma}}^2 - h_1^{\overline{\sigma}\sigma}(Q)h_{3a}^{\sigma\overline{\sigma}}(Q)v_{\sigma}^2 - h_1^{\sigma\overline{\sigma}}(Q)h_{3a}^{\overline{\sigma}\sigma}(Q)v_{\sigma}^2)$$

$$\frac{dh_{3b}^{\overline{\sigma}\sigma}(Q)}{dy} = 4h_2^{\overline{\sigma}\sigma}(Q)h_{3b}^{\overline{\sigma}\sigma}(Q)v_{\overline{\sigma}}^2$$

$$\frac{dh_{3c}^{\overline{\sigma}\sigma}(0)}{dy} = -4h_4^{\overline{\sigma}\sigma}(0)h_{3c}^{\overline{\sigma}\sigma}(0)v_{\overline{\sigma}}^2$$

$$\frac{dh_{3a}^{\sigma\overline{\sigma}}(Q)}{dy} = 2(h_1^{\sigma\overline{\sigma}}(Q)(h_{3b}^{\sigma\sigma}(Q) - h_{3a}^{\sigma\sigma}(Q))v_{\sigma}^2 + h_1^{\sigma\overline{\sigma}}(Q)(h_{3b}^{\overline{\sigma}\sigma}(Q) - h_{3a}^{\overline{\sigma}\sigma}(Q))v_{\overline{\sigma}}^2 + h_{3a}^{\sigma\overline{\sigma}}(Q)(h_2^{\sigma\sigma}(Q)v_{\sigma}^2 + h_2^{\overline{\sigma}\sigma}(Q)v_{\overline{\sigma}}^2 - h_1^{\sigma\sigma}(Q)v_{\sigma}^2 - h_1^{\overline{\sigma}\sigma}(Q)v_{\overline{\sigma}}^2))$$

$$\frac{dh_{3b}^{\sigma\overline{\sigma}}(Q)}{dy} = 4h_2^{\sigma\overline{\sigma}}(Q)h_{3b}^{\sigma\overline{\sigma}}(Q)v_{\sigma}v_{\overline{\sigma}}$$

$$\frac{dh_{3c}^{\sigma\overline{\sigma}}(0)}{dy} = -4h_4^{\sigma\overline{\sigma}}(0)h_{3c}^{\sigma\overline{\sigma}}(0)v_{\sigma}v_{\overline{\sigma}}$$

$$\frac{dh_{3a}^{\overline{\sigma}\sigma}(Q)}{dy} = 2(h_1^{\overline{\sigma}\sigma}(Q)(h_{3b}^{\sigma\sigma}(Q) - h_{3a}^{\sigma\sigma}(Q))v_{\sigma}^2 + h_1^{\overline{\sigma}\sigma}(Q)(h_{3b}^{\overline{\sigma}\sigma}(Q) - h_{3a}^{\overline{\sigma}\sigma}(Q))v_{\overline{\sigma}}^2 + h_{3a}^{\overline{\sigma}\sigma}(Q)(h_2^{\sigma\sigma}(Q)v_{\sigma}^2 + h_2^{\overline{\sigma}\sigma}(Q)v_{\overline{\sigma}}^2 - h_1^{\sigma\sigma}(Q)v_{\sigma}^2 - h_1^{\overline{\sigma}\sigma}(Q)v_{\overline{\sigma}}^2))$$

$$\frac{dh_{3b}^{\overline{\sigma}\sigma}(Q)}{dy} = 4h_2^{\overline{\sigma}\sigma}(Q)h_{3b}^{\overline{\sigma}\sigma}(Q)v_{\sigma}v_{\overline{\sigma}}$$

$$\frac{dh_{3c}^{\overline{\sigma}\sigma}(0)}{dy} = -4h_4^{\overline{\sigma}\sigma}(0)h_{3c}^{\overline{\sigma}\sigma}(0)v_{\sigma}v_{\overline{\sigma}}$$

$$\frac{dh_4^{\sigma\sigma}(0)}{dy} = -2((h_{3c}^{\sigma\sigma}(0))^2 + (h_4^{\sigma\sigma}(0))^2)v_\sigma^2$$
$$\frac{dh_4^{\overline{\sigma}\overline{\sigma}}(0)}{dy} = -2((h_{3c}^{\overline{\sigma}\overline{\sigma}}(0))^2 + (h_4^{\overline{\sigma}\overline{\sigma}}(0))^2)v_{\overline{\sigma}}^2$$

$$\frac{dh_4^{\sigma\overline{\sigma}}(0)}{dy} = -2((h_{3c}^{\sigma\overline{\sigma}}(0))^2 + (h_4^{\sigma\overline{\sigma}}(0))^2)v_\sigma v_{\overline{\sigma}}$$
$$\frac{dh_4^{\overline{\sigma}\sigma}(0)}{dy} = -2((h_{3c}^{\overline{\sigma}\sigma}(0))^2 + (h_4^{\overline{\sigma}\sigma}(0))^2)v_\sigma v_{\overline{\sigma}}$$

From the above equations, we find

$$\frac{d(h_{3c}^{\sigma\overline{\sigma}}(0) - h_4^{\sigma\overline{\sigma}}(0))}{dy} = 2(h_{3c}^{\sigma\overline{\sigma}}(0) - h_4^{\sigma\overline{\sigma}}(0))^2 v_\sigma v_{\overline{\sigma}}$$

for the superconducting vertex. These equations can be solved to give

$$h_3^{\sigma\overline{\sigma}}(0) - h_4^{\sigma\overline{\sigma}}(0) = \frac{(h_3^{\sigma\overline{\sigma}})_{E_F} - (h_4^{\sigma\overline{\sigma}})_{E_F}}{1 - 2v_\sigma v_{\overline{\sigma}}((h_3^{\sigma\overline{\sigma}})_{E_F} - (h_4^{\sigma\overline{\sigma}})_{E_F})\log[\frac{E_F}{\omega}]}$$

A similar situation arises for the SDW instability in this regime. The competition between these instabilities depends on the respective energies at which different combinations of couplings diverge, and thus, on their values at the Fermi energy E_F. The first instability occurs in the channel for which the coupling at $\omega \sim E_F$ is the largest.

To illustrate the nature of the most divergent couplings in the two limits, RG flows for $M < M_c$ and $M > M_c$ with a dimensionless initial repulsive interaction of 0.1 and a Hund's splitting of 5% ($\frac{|h_i^{\sigma\overline{\sigma}} - h_i^{\sigma\sigma}|}{|h_i^{\sigma\sigma}|} = 0.05$) introduced initially, where the critical value of the Zeeman splitting $M_c \approx 6.1$ meV, are shown in the Fig 3. The corresponding behavior of $h_i^{\sigma\sigma'}(y)(y_c - y)$ as a function of $(y_c - y)$, which illustrates the order of the fixed point values $g_i^{\sigma\sigma'}$ for the different couplings in the above-mentioned two cases, is shown in the Fig. 4.

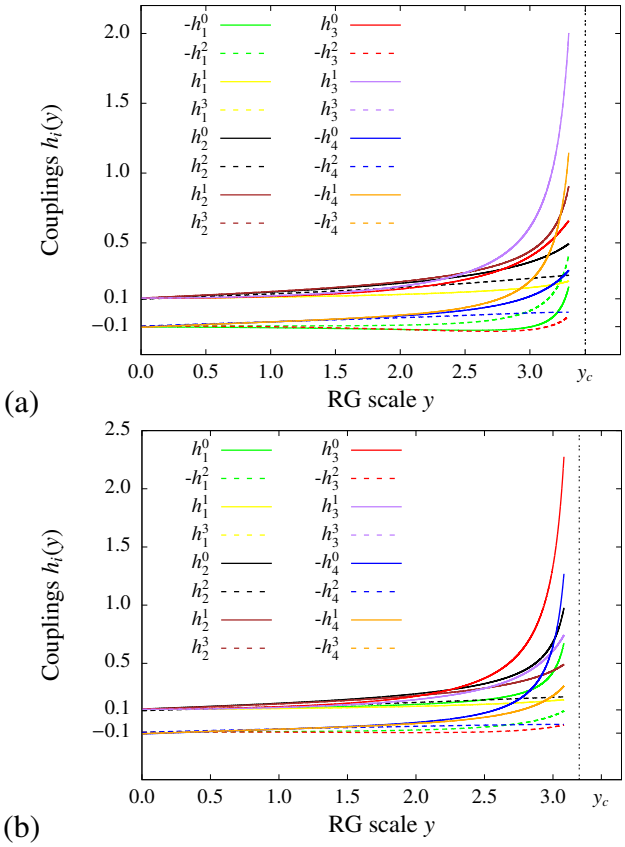

Fig. 3 The RG flows for (a) $M = 4$ meV and (b) $M = 7$ meV where the critical value of spin-splitting $M_c \approx 6.1$ meV. The fixed point value $y_c \approx 3.43$ for (a) and $y_c \approx 3.2$ for (b) above. Here, the initial values for each of the dimensionless couplings is taken to be 0.1, and a Hund's splitting of 5% ($\frac{|h_i^{\sigma\overline{\sigma}} - h_i^{\sigma\sigma}|}{|h_i^{\sigma\sigma}|} = 0.05$) is introduced initially such that $h_i^{\sigma\overline{\sigma}} > h_i^{\sigma\sigma}$ for $i = 1-4$ and $\sigma = \uparrow, \downarrow$. Clearly, the leading couplings near the instability threshold correspond to spin-antiparallel configurations for $M < M_c$, while the spin $\uparrow$ component of each of the couplings dominates for $M > M_c$. Here the couplings $h_i^{\uparrow\uparrow}$, $h_i^{\downarrow\downarrow}$, $h_i^{\uparrow\downarrow}$and $h_i^{\downarrow\uparrow}$ are denoted respectively by h_i^0, h_i^2, h_i^1 and h_i^3, for clarity. The factors of $v_\uparrow$ and $v_\downarrow$ have been absorbed into the couplings constants h_i^ℓ ($\ell = 0-3$) in the above plots, for simplicity in notation.

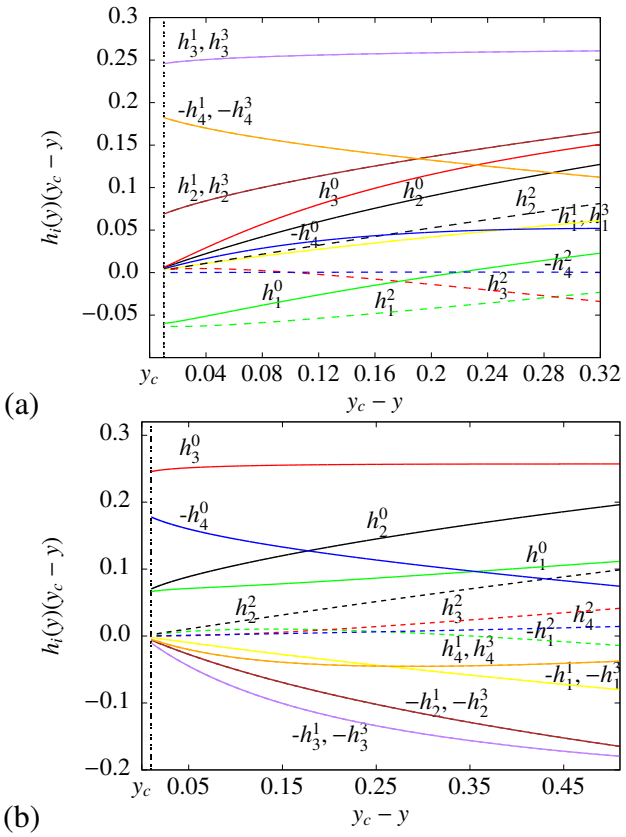

Fig. 4 The order of the fixed-point values for the different couplings h_i^ℓ ($\ell = 0-3$) at the critical point y_c for (a) $M = 4$ meV and (b) $M = 7$ meV, where the critical spin-splitting $M_c \approx 6.1$ meV. Here, the initial values for each of the dimensionless couplings is taken to be 0.1, and a Hund's splitting of 5% ($\frac{|h_i^{\sigma\overline{\sigma}} - h_i^{\sigma\sigma}|}{|h_i^{\sigma\sigma}|} = 0.05$) is introduced initially such that $h_i^{\sigma\overline{\sigma}} > h_i^{\sigma\sigma}$ for $i = 1-4$ and $\sigma = \uparrow, \downarrow$. The above plots show the evolution of $h_i^\ell(y)$ as a function of $(y_c - y)$ close to the fixed point y_c, where each coupling constant h_i^ℓ has an asymptodic form $\frac{g_i^\ell}{y_c - y}$, and the y-intercepts of curves shown give an estimate of the fixed-point values g_i^ℓ for the different couplings. This clearly indicates that the leading couplings for $M < M_c$ correspond to the odd angular momentum ($\ell = 1$ and $\ell = 3$) channels, for spin-antiparallel configurations, in the presence of a finite Hund's splitting, while for $M > M_c$ these correspond to the spin $\uparrow$ ($\ell = 0$) channel. As in Fig. 3, the factors of $v_\uparrow$ and $v_\downarrow$ corresponding to each coupling have been absorbed into h_i^ℓ ($\ell = 0-3$).

Appendix C

Derivation of the asymptotic form of the bound state wavefunctions for point defects

Here we derive the expressions for the asymptotic form of the bound state wavefunctions for a point defect in a chiral $p-$wave superconductor.

The expression for the bound state wavefunctions for point defects involves the following integrals

$$I_1(r) = -\frac{1}{(2\pi)^2}\int kdkd\phi \exp\{ikr\cos[\theta-\phi]\}\frac{(Ak^2+\mu')}{(Ak^2+\mu')^2+\Delta^2k^2}$$

and

$$I_2(r,\theta) = \frac{1}{(2\pi)^2}\int kdkd\phi \exp\{ikr\cos[\theta-\phi]\}\exp[i\phi]\frac{\Delta k}{(Ak^2+\mu')^2+\Delta^2k^2}$$

where $k=\sqrt{k_x^2+k_y^2}$, $\tan[\phi]=\frac{y}{x}$. Let us now consider the integral I_1. Using the result $\int d\phi \exp\{ikr\cos[\theta-\phi]\} = 2\pi J_0(kr)$, we have

$$I_1(r) = -\frac{1}{(2\pi)^2}\int kdk\frac{Ak^2+\mu'}{(Ak^2+\mu')^2+\Delta^2k^2}2\pi J_0(kr)$$

The above expression may be rewritten as

$$I_1 = -\frac{1}{2\pi}\int kdk\frac{\frac{1}{2}(Ak^2+\mu'+i\Delta k)+\frac{1}{2}(Ak^2+\mu'-i\Delta k)}{(Ak^2+\mu')^2+\Delta^2k^2}J_0(kr)$$

$$= -\frac{1}{4\pi}\int dkkJ_0(kr)\frac{1}{A}\left(\frac{1}{(k-k_1)(k-k_2)}+\frac{1}{(k-k_3)(k-k_4)}\right)$$

where $k_1 = i\sqrt{\frac{\mu'}{A}}\frac{\sqrt{\lambda+2}+\sqrt{\lambda}}{\sqrt{2}}$, $k_2 = i\sqrt{\frac{\mu'}{A}}\frac{\sqrt{\lambda}-\sqrt{\lambda+2}}{\sqrt{2}}$, $k_3 = i\sqrt{\frac{\mu'}{A}}\frac{\sqrt{\lambda+2}-\sqrt{\lambda}}{\sqrt{2}} = -k_2$, $k_4 = -i\sqrt{\frac{\mu'}{A}}\frac{\sqrt{\lambda+2}+\sqrt{\lambda}}{\sqrt{2}} = -k_1$. This can further be simplified as

$$-\frac{1}{4\pi}\int dkkJ_0(kr)\frac{1}{A(k_1-k_2)}\left(\frac{2k_1}{k^2-k_1^2}-\frac{2k_2}{k^2-k_2^2}\right)$$

Let us now rewrite $k_1 = i\alpha, k_2 = -i\beta$ where α and β are real, and $\alpha, \beta > 0$ ($\alpha = \sqrt{\frac{\mu'}{A}}\frac{\sqrt{\lambda+2}+\sqrt{\lambda}}{\sqrt{2}}$, $\beta = \sqrt{\frac{\mu'}{A}}\frac{\sqrt{\lambda+2}-\sqrt{\lambda}}{\sqrt{2}}$). The above equation can be rewritten as

$$-\frac{1}{4\pi}\int dk k J_0(kr)\frac{2}{A(\alpha+\beta)}\left(\frac{\alpha}{k^2+\alpha^2}+\frac{\beta}{k^2+\beta^2}\right)$$

To evaluate the above expression, we shall use the standard integral [218]

$$\int_0^\infty dk \frac{kJ_0(kr)}{k^2+\alpha^2} = K_0(\alpha r),$$

which is applicable in our case, since $r > 0$, α, β are real and $Re[\alpha]$,$Re[\beta] > 0$. The asymptotic form of the RHS is given by

$$K_0(\alpha r) \sim \left(\frac{\pi}{2\alpha r}\right)^{1/2}\exp[-\alpha r]\sum_{n=0}^{\infty}\frac{a_n(0)}{(\alpha r)^n}$$

where $a_n(\nu) = \frac{(4\nu^2-1^2)(4\nu^2-3^2)\ldots(4\nu^2-(2n+1)^2)}{(n+1)!}\left(\frac{1}{4\nu^2-1^2}+\frac{1}{4\nu^2-2^2}+\ldots\frac{1}{4\nu^2-(2n+1)^2}\right)$. Using these results, we find

$$I_1(r) = -\frac{1}{2\pi A(\alpha+\beta)}(\alpha K_0(\alpha r)+\beta K_0(\beta r))$$

which is an exponentially decaying function at large values of r.

Similarly, using the result $\int d\phi \exp\{ikr\cos[\theta-\phi]\}\exp[i\phi] = i2\pi J_1(kr)\exp[i\theta]$, we may simplify the expression for I_2 as

$$I_2(r,\theta) = \frac{\exp[i\theta]}{(2\pi)^2}\int kdk\frac{\Delta k}{(Ak^2+\mu')^2+\Delta^2k^2}i2\pi J_1(kr)$$

$$= \frac{\exp[i\theta]}{2\pi}\int dk k J_1(kr)\frac{1}{2}\left(\frac{1}{Ak^2+\mu'-i\Delta k}-\frac{1}{Ak^2+\mu'+i\Delta k}\right)$$

$$= \frac{\exp[i\theta]}{4\pi}\int dk k J_1(kr)\frac{1}{A(k_1-k_2)}\left(\frac{1}{k-k_1}-\frac{1}{k-k_2}+\frac{1}{k+k_1}-\frac{1}{k+k_2}\right)$$

$k_1 = i\sqrt{\frac{\mu'}{A}}\frac{\sqrt{\lambda+2}+\sqrt{\lambda}}{\sqrt{2}}$, $k_2 = i\sqrt{\frac{\mu'}{A}}\frac{\sqrt{\lambda}-\sqrt{\lambda+2}}{\sqrt{2}}$, $k_3 = i\sqrt{\frac{\mu'}{A}}\frac{\sqrt{\lambda+2}-\sqrt{\lambda}}{\sqrt{2}} = -k_2$, $k_4 = -i\sqrt{\frac{\mu'}{A}}\frac{\sqrt{\lambda+2}+\sqrt{\lambda}}{\sqrt{2}} = -k_1$. This can be rewritten as

$$\frac{\exp[i\theta]}{4\pi}\int dk k J_1(kr)\frac{1}{A(k_1-k_2)}\left(\frac{2k}{k^2-k_1^2}-\frac{2k}{k^2-k_2^2}\right)$$

Again, replacing k_1 by $i\alpha$ and k_2 by $-i\beta$, where α and β are real,and $\alpha,\beta > 0$ ($\alpha = \sqrt{\frac{\mu'}{A}}\frac{\sqrt{\lambda+2}+\sqrt{\lambda}}{\sqrt{2}}$, $\beta = \sqrt{\frac{\mu'}{A}}\frac{\sqrt{\lambda+2}-\sqrt{\lambda}}{\sqrt{2}}$), we find

$$I_2 = \frac{\exp[i\theta]}{4\pi}\int dk J_1(kr)\frac{2}{Ai(\alpha+\beta)}(\frac{k^2}{k^2+\alpha^2} - \frac{k^2}{k^2+\beta^2})$$

Let us rewrite the variable of integration as $kr \equiv x$. Then

$$I_2 = \frac{\exp[i\theta]}{2\pi Ai(\alpha+\beta)}\int \frac{dx}{r}J_1(x)(\frac{x^2}{x^2+\alpha^2r^2} - \frac{x^2}{x^2+\beta^2r^2}) \tag{2}$$

To evaluate the above Eq. 2, we shall use the standard integral [218]

$$\int_0^\infty dx \frac{xJ_0(ax)}{x^2+\alpha^2r^2} = K_0(a\alpha r),$$

where $r > 0$, α,β are real and $Re[\alpha], Re[\beta] > 0$. Here, we differentiate both sides with respect to a, and then take the limit $a \to 1$, we have

$$\int_0^\infty \frac{x^2J_1(x)}{x^2+\alpha^2r^2}dx = K_1(\alpha r) \tag{3}$$

Thus, using Eq. 3 in Eq. 2, we have

$$I_2 = \frac{\exp[i\theta]}{2\pi Ai(\alpha+\beta)r}(K_1(\alpha r) - K_1(\beta r))$$

The asymptotic form of the function on the RHS is given by

$$K_1(\alpha r) \sim (\frac{\pi}{2\alpha r})^{1/2}\exp[-\alpha r]\sum_{n=0}^{\infty}\frac{a_n(1)}{(\alpha r)^n}$$

where $a_n(\nu) = \frac{(4\nu^2-1^2)(4\nu^2-3^2)...(4\nu^2-(2n+1)^2)}{(n+1)!}(\frac{1}{4\nu^2-1^2} + \frac{1}{4\nu^2-2^2} + ...\frac{1}{4\nu^2-(2n+1)^2})$, which is exponentially decaying in nature.

Appendix D

Order parameters in terms of bosonic fields

In our analysis, the fermionic bilinears for the order parameters are expressed in terms of Gell-Mann matrices, which are a set of eight linearly independent 3×3 traceless Hermitian matrices. These are as follows-

$$\lambda^1 = \begin{pmatrix} 0 & 1 & 0 \\ 1 & 0 & 0 \\ 0 & 0 & 0 \end{pmatrix}, \lambda^2 = \begin{pmatrix} 0 & -i & 0 \\ i & 0 & 0 \\ 0 & 0 & 0 \end{pmatrix}$$

$$\lambda^3 == \begin{pmatrix} 1 & 0 & 0 \\ 0 & -1 & 0 \\ 0 & 0 & 0 \end{pmatrix}, \lambda^4 = \begin{pmatrix} 0 & 0 & 1 \\ 0 & 0 & 0 \\ 1 & 0 & 0 \end{pmatrix}$$

$$\lambda^5 = \begin{pmatrix} 0 & 0 & -i \\ 0 & 0 & 0 \\ i & 0 & 0 \end{pmatrix}, \lambda^6 = \begin{pmatrix} 0 & 0 & 0 \\ 0 & 0 & 1 \\ 0 & 1 & 0 \end{pmatrix}$$

$$\lambda^7 = \begin{pmatrix} 0 & 0 & 0 \\ 0 & 0 & -i \\ 0 & i & 0 \end{pmatrix}, \lambda^8 = \frac{1}{\sqrt{3}} \begin{pmatrix} 1 & 0 & 0 \\ 0 & 1 & 0 \\ 0 & 0 & -2 \end{pmatrix}$$

Below, we list the expressions for the sixteen order parameters in terms of the bosonic fields:

$$
\begin{aligned}
&Re[O_{ph}^{10}] \propto \sin[\sqrt{2}\widetilde{\theta}_1]\cos[\frac{2\widetilde{\phi}_{-1}}{\sqrt{6}}+\frac{2\widetilde{\phi}_0}{\sqrt{3}}-2k_Fx]\\
&Re[O_{ph}^{20}] \propto \cos[\sqrt{2}\widetilde{\theta}_1]\cos[\frac{2\widetilde{\phi}_{-1}}{\sqrt{6}}+\frac{2\widetilde{\phi}_0}{\sqrt{3}}-2k_Fx]\\
&Re[O_{ph}^{30}] \propto \sin[\sqrt{2}\widetilde{\phi}_1]\cos[\frac{2\widetilde{\phi}_{-1}}{\sqrt{6}}+\frac{2\widetilde{\phi}_0}{\sqrt{3}}-2k_Fx]\\
&Re[O_{ph}^{40}] \propto \sin[\frac{\widetilde{\theta}_1}{\sqrt{2}}+\frac{3\widetilde{\theta}_{-1}}{\sqrt{6}}]\cos[\frac{\widetilde{\phi}_1}{\sqrt{2}}-\frac{\widetilde{\phi}_{-1}}{\sqrt{6}}+\frac{2\widetilde{\phi}_0}{\sqrt{3}}-2k_Fx]\\
&Re[O_{ph}^{50}] \propto \cos[\frac{\widetilde{\theta}_1}{\sqrt{2}}+\frac{3\widetilde{\theta}_{-1}}{\sqrt{6}}]\cos[\frac{\widetilde{\phi}_1}{\sqrt{2}}-\frac{\widetilde{\phi}_{-1}}{\sqrt{6}}+\frac{2\widetilde{\phi}_0}{\sqrt{3}}-2k_Fx]\\
&Re[O_{ph}^{60}] \propto \sin[\frac{\widetilde{\theta}_1}{\sqrt{2}}-\frac{3\widetilde{\theta}_{-1}}{\sqrt{6}}]\cos[\frac{\widetilde{\phi}_1}{\sqrt{2}}+\frac{\widetilde{\phi}_{-1}}{\sqrt{6}}-\frac{2\widetilde{\phi}_0}{\sqrt{3}}+2k_Fx]\\
&Re[O_{ph}^{70}] \propto \cos[\frac{\widetilde{\theta}_1}{\sqrt{2}}-\frac{3\widetilde{\theta}_{-1}}{\sqrt{6}}]\cos[\frac{\widetilde{\phi}_1}{\sqrt{2}}+\frac{\widetilde{\phi}_{-1}}{\sqrt{6}}-\frac{2\widetilde{\phi}_0}{\sqrt{3}}+2k_Fx]\\
&Re[O_{ph}^{80}] \propto (\cos[\sqrt{2}\widetilde{\phi}_1]\sin[\frac{2\widetilde{\phi}_{-1}}{\sqrt{6}}+\frac{2\widetilde{\phi}_0}{\sqrt{3}}-2k_Fx]+\sin[\frac{4}{\sqrt{6}}\widetilde{\phi}_{-1}-\frac{2\widetilde{\phi}_0}{\sqrt{3}}-2k_Fx])\\
&Re[O_{pp}^{10}] \propto \sin[\sqrt{2}\widetilde{\phi}_1]\cos[\frac{2\widetilde{\theta}_{-1}}{\sqrt{6}}+\frac{2\widetilde{\theta}_0}{\sqrt{3}}]\\
&Re[O_{pp}^{20}] \propto \cos[\sqrt{2}\widetilde{\phi}_1]\cos[\frac{2\widetilde{\theta}_{-1}}{\sqrt{6}}+\frac{2\widetilde{\theta}_0}{\sqrt{3}}]\\
&Re[O_{pp}^{30}] \propto \sin[\sqrt{2}\widetilde{\theta}_1]\cos[\frac{2\widetilde{\theta}_{-1}}{\sqrt{6}}+\frac{2\widetilde{\theta}_0}{\sqrt{3}}]\\
&Re[O_{pp}^{40}] \propto \sin[\frac{\widetilde{\phi}_1}{\sqrt{2}}+\frac{3\widetilde{\phi}_{-1}}{\sqrt{6}}]\cos[\frac{\widetilde{\theta}_1}{\sqrt{2}}-\frac{\widetilde{\theta}_{-1}}{\sqrt{6}}+\frac{2\widetilde{\theta}_0}{\sqrt{3}}]\\
&Re[O_{pp}^{50}] \propto \cos[\frac{\widetilde{\phi}_1}{\sqrt{2}}+\frac{3\widetilde{\phi}_{-1}}{\sqrt{6}}]\cos[\frac{\widetilde{\theta}_1}{\sqrt{2}}-\frac{\widetilde{\theta}_{-1}}{\sqrt{6}}+\frac{2\widetilde{\theta}_0}{\sqrt{3}}]\\
&Re[O_{pp}^{60}] \propto \sin[\frac{\widetilde{\phi}_1}{\sqrt{2}}-\frac{3\widetilde{\phi}_{-1}}{\sqrt{6}}]\cos[\frac{\widetilde{\theta}_1}{\sqrt{2}}+\frac{\widetilde{\theta}_{-1}}{\sqrt{6}}-\frac{2\widetilde{\theta}_0}{\sqrt{3}}]\\
&Re[O_{pp}^{70}] \propto \cos[\frac{\widetilde{\phi}_1}{\sqrt{2}}-\frac{3\widetilde{\phi}_{-1}}{\sqrt{6}}]\cos[\frac{\widetilde{\theta}_1}{\sqrt{2}}+\frac{\widetilde{\theta}_{-1}}{\sqrt{6}}-\frac{2\widetilde{\theta}_0}{\sqrt{3}}]\\
&Re[O_{pp}^{80}] \propto (\cos[\sqrt{2}\widetilde{\theta}_1]\sin[\frac{2\widetilde{\theta}_{-1}}{\sqrt{6}}+\frac{2\widetilde{\theta}_0}{\sqrt{3}}]+\sin[\frac{4\widetilde{\theta}_{-1}}{\sqrt{6}}-\frac{2\widetilde{\theta}_0}{\sqrt{3}}])
\end{aligned}
\tag{4}
$$

The RG equations for the above order parameters are given as follows-

$$\frac{dO_{ph}^{10}}{dy} = (2 - \frac{1}{16\pi}((A_1^{(4)})^2 + (A_{-1}^{(4)})^2 + (a_1^{(7)})^2 + (a_{-1}^{(7)})^2))O_{ph}^{10}$$
$$\frac{dO_{ph}^{20}}{dy} = (2 - \frac{1}{16\pi}((A_1^{(4)})^2 + (A_{-1}^{(4)})^2 + (a_1^{(7)})^2 + (a_{-1}^{(7)})^2))O_{ph}^{20}$$
$$\frac{dO_{ph}^{40}}{dy} = (2 - \frac{1}{16\pi}((a_1^{(9)})^2 + (a_{-1}^{(9)})^2 + (A_1^{(5)})^2 + (A_{-1}^{(5)})^2)))O_{ph}^{40}$$
$$\frac{dO_{ph}^{50}}{dy} = (2 - \frac{1}{16\pi}((a_1^{(9)})^2 + (a_{-1}^{(9)})^2 + (A_1^{(5)})^2 + (A_{-1}^{(5)})^2))O_{ph}^{50}$$
$$\frac{dO_{ph}^{60}}{dy} = (2 - \frac{1}{16\pi}((a_1^{(8)})^2 + (a_{-1}^{(8)})^2 + (A_1^{(6)})^2 + (A_{-1}^{(6)})^2)))O_{ph}^{60}$$
$$\frac{dO_{ph}^{70}}{dy} = (2 - \frac{1}{16\pi}((a_1^{(8)})^2 + (a_{-1}^{(8)})^2 + (A_1^{(6)})^2 + (A_{-1}^{(6)})^2))O_{ph}^{70}$$
$$\frac{d\Delta_{ph}^{10}}{dy} = (2 - \frac{1}{4\pi}(a_1^2 + a_{-1}^2))\Delta_{ph}^{10}$$
$$\frac{d\Delta_{ph}^{20}}{dy} = (2 - \frac{1}{4\pi}(b_1^2 + b_{-1}^2))\Delta_{ph}^{20}$$
$$\frac{d\Delta_{ph}^{30}}{dy} = (2 - \frac{1}{4\pi}(c_1^2 + c_{-1}^2))\Delta_{ph}^{30}$$
$$\frac{dO_{pp}^{10}}{dy} = (2 - \frac{1}{16\pi}((a_1^{(1)})^2 + (a_{-1}^{(1)})^2 + (A_1^{(7)})^2 + (A_{-1}^{(7)})^2))O_{pp}^{10}$$
$$\frac{dO_{pp}^{20}}{dy} = (2 - \frac{1}{16\pi}((a_1^{(1)})^2 + (a_{-1}^{(1)})^2 + (A_1^{(7)})^2 + (A_{-1}^{(7)})^2))O_{pp}^{20}$$
$$\frac{dO_{pp}^{40}}{dy} = (2 - \frac{1}{16\pi}((a_1^{(2)})^2 + (a_{-1}^{(2)})^2 + (A_1^{(9)})^2 + (A_{-1}^{(9)})^2))O_{pp}^{40}$$
$$\frac{dO_{pp}^{50}}{dy} = (2 - \frac{1}{16\pi}((a_1^{(2)})^2 + (a_{-1}^{(2)})^2 + (A_1^{(9)})^2 + (A_{-1}^{(9)})^2))O_{pp}^{50}$$
$$\frac{dO_{pp}^{60}}{dy} = (2 - \frac{1}{16\pi}((a_1^{(3)})^2 + (a_{-1}^{(3)})^2 + (A_1^{(8)})^2 + (A_{-1}^{(8)})^2))O_{pp}^{60}$$
$$\frac{dO_{pp}^{70}}{dy} = (2 - \frac{1}{16\pi}((a_1^{(3)})^2 + (a_{-1}^{(3)})^2 + (A_1^{(8)})^2 + (A_{-1}^{(8)})^2))O_{pp}^{70}$$
$$\frac{d\Delta_{pp}^{10}}{dy} = (2 - \frac{1}{4\pi}(A_1^2 + A_{-1}^2))\Delta_{pp}^{10}$$
$$\frac{d\Delta_{pp}^{20}}{dy} = (2 - \frac{1}{4\pi}(B_1^2 + B_{-1}^2))\Delta_{pp}^{20}$$
$$\frac{d\Delta_{pp}^{30}}{dy} = (2 - \frac{1}{4\pi}(C_1^2 + C_{-1}^2))\Delta_{pp}^{30} \quad (5)$$

where $A_i^{(\alpha)}, \alpha = 7-9$ are defined analogously to $a_i^{(\alpha)}, \alpha = 7-9$. Note that we have studied the RG flow equations for each of the terms $\Delta^{i0}_{pp/ph}(i = 1-3)$, in the order parameters $O^{30}_{ph/pp}$ and $O^{80}_{ph/pp}$ defined in Eq.4 separately. The scaling dimensions of either of these sets of terms cannot be expressed in terms of those of the interaction couplings considered in our analysis.